

# SELF-CONSISTENT CORONAL HEATING AND SOLAR WIND ACCELERATION FROM ANISOTROPIC MAGNETOHYDRODYNAMIC TURBULENCE

STEVEN R. CRANMER, ADRIAAN A. VAN BALLEGOOIJEN, AND RICHARD J. EDGAR

Harvard-Smithsonian Center for Astrophysics, 60 Garden Street, Cambridge, MA 02138

Submitted 2006 December 15; accepted 2007 March 11

Draft version April 9, 2018

## ABSTRACT

We present a series of models for the plasma properties along open magnetic flux tubes rooted in solar coronal holes, streamers, and active regions. These models represent the first self-consistent solutions that combine: (1) chromospheric heating driven by an empirically guided acoustic wave spectrum, (2) coronal heating from Alfvén waves that have been partially reflected, then damped by anisotropic turbulent cascade, and (3) solar wind acceleration from gradients of gas pressure, acoustic wave pressure, and Alfvén wave pressure. The only input parameters are the photospheric lower boundary conditions for the waves and the radial dependence of the background magnetic field along the flux tube. We have not included multifluid or collisionless effects (e.g., preferential ion heating) which are not yet fully understood. For a single choice for the photospheric wave properties, our models produce a realistic range of slow and fast solar wind conditions by varying only the coronal magnetic field. Specifically, a two-dimensional model of coronal holes and streamers at solar minimum reproduces the latitudinal bifurcation of slow and fast streams seen by *Ulysses*. The radial gradient of the Alfvén speed affects where the waves are reflected and damped, and thus whether energy is deposited below or above the Parker critical point. As predicted by earlier studies, a larger coronal “expansion factor” gives rise to a slower and denser wind, higher temperature at the coronal base, less intense Alfvén waves at 1 AU, and correlative trends for commonly measured ratios of ion charge states and FIP-sensitive abundances that are in general agreement with observations. These models offer supporting evidence for the idea that coronal heating and solar wind acceleration (in open magnetic flux tubes) can occur as a result of wave dissipation and turbulent cascade.

*Subject headings:* MHD — solar wind — Sun: atmospheric motions — Sun: corona — turbulence — waves

## 1. INTRODUCTION

One of the most persistent problems in solar physics has been the unambiguous identification of the mechanisms that heat the Sun’s corona and accelerate the solar wind. Many processes have been proposed for converting some fraction of the mechanical energy in subphotospheric convective motions to heat, but it has proved very difficult to make distinguishing comparisons between the predictions of these competing ideas and specific observations. We are entering an era, though, where both the models and the measurements are improving to the point of soon being able to eliminate many of the candidate theories. For example, it seems increasingly clear that closed loops in the low corona are heated by small-scale, intermittent magnetic reconnection that is driven by the continual stressing of their magnetic footpoints (see recent reviews by Longcope 2004; Gudiksen 2005; Aschwanden 2006; Klimchuk 2006).

In this paper we model the coronal heating along open field lines that reach into interplanetary space. We construct a self-consistent model of the photosphere, chromosphere, corona, and solar wind that is driven mainly by magnetohydrodynamic (MHD) turbulence and is free of arbitrary “heating functions” that have been used in the past. This work continues earlier studies (Cranmer & van Ballegoijen 2005; Cranmer 2005a) which used prescribed empirical descriptions of the density and flow velocity along an open flux tube in order to compute the rates of turbulent heating and acceleration. The main goal of this paper is to provide a possible explanation for the origin and properties of fast and slow solar wind

streams. Another goal, though, is to illustrate how the particular description of MHD turbulence can be applied to more advanced modeling efforts—specifically those that attempt to reproduce the full three-dimensional and time-dependent nature of the corona and heliosphere (e.g., Riley et al. 2001; Roussev et al. 2003; Tóth et al. 2005; Usmanov & Goldstein 2006).

Coronal heating and solar wind acceleration have been known to be closely linked since the initial contributions of Parker (1958). However, nearly all subsequent theoretical attempts to model both processes together have made limiting assumptions about either the heating (i.e., ad hoc energy input rates) or the acceleration (i.e., a prescribed mass flux). It has been realized over the past few decades that it is key to resolve the full chromosphere-corona transition region in order to produce a model with an internally consistent radial dependence of pressure, density, and flow speed (see Hammer 1982; Hansteen & Leer 1995; Hansteen et al. 1997; Lie-Svendsen & Esser 2005). To our knowledge, the only solar wind models—other than the ones presented in this paper—that contain *both* a first-principles approach to coronal heating and a self-consistent chromosphere, transition region, and mass flux are those of Suzuki & Inutsuka (2005, 2006).<sup>1</sup>

The study of MHD turbulence as a potential source of heating for the solar wind goes back to Coleman (1968) and Jokipii & Davis (1969). Hollweg (1986) extended these ideas

<sup>1</sup> Other models can be included if some of the above conditions are relaxed. For example, Hu et al. (2000) and Li (2002, 2003) considered wave-driven coronal heating with a lower boundary within the transition region (i.e., temperatures ranging between  $6 \times 10^4$  and  $8 \times 10^5$  K). See § 2 below for a comparison of the underlying physical assumptions and numerical approaches.

down into the corona and laid the foundations for the cascade-driven heating rates used by Isenberg (1990), Li et al. (1999), Matthaeus et al. (1999), Dmitruk et al. (2001, 2002), and this paper. These ideas are highly complementary to theoretical models of wave dissipation via ion cyclotron resonance (e.g., Hollweg & Isenberg 2002; Cranmer 2000, 2001, 2002) that have been invoked to explain the observed preferential heating of heavy ions in the extended corona (Kohl et al. 1997, 1998, 2006). In the cascade paradigm, the energy in large-scale Alfvénic fluctuations must eventually be dissipated in small-scale (short wavelength or high frequency) collisionless kinetic modes. The results from this paper can thus be used as initial conditions for detailed models of the anisotropic turbulent cascade and minor ion heating.

The remainder of this paper is organized as follows. In § 2 we present an overview of the general principles involved in our modeling effort (i.e., why certain physical processes are included or excluded). § 3 gives the conservation equations that are solved and the adopted prescriptions for basic ingredients such as radiative heating/cooling and conduction. The detailed treatment of waves is described in the following three sections: acoustic waves and shock heating in § 4, Alfvén waves and turbulent cascade in § 5, and the ponderomotive wave pressure acceleration due to both types of fluctuations in § 6. The numerical methods used to solve the equations and the newly developed computer code, called ZEPHYR, are described in § 7. We then present a comprehensive set of solutions for the solar wind emerging from coronal holes, helmet streamers, and active regions (§ 8). A summary of the major results of this paper, together with a discussion of the implications for understanding the winds of other stars, is given in § 9.

## 2. MODEL PHILOSOPHY

We consider the *one-dimensional* variation of plasma parameters along a radially pointed magnetic flux tube rooted in the solar photosphere and open to interplanetary space. Some effects of the multi-dimensional magnetic field in the photosphere and chromosphere are included as explicit superradial expansion of the flux tube (see also Cranmer & van Ballegoijen 2005), but otherwise we ignore the effects of neighboring closed flux tubes. We assume that most of the plasma that eventually becomes the time-steady solar wind originates in small (100 km sized) intergranular flux concentrations that are concentrated most densely in the supergranular network.

The models we construct are *time-independent* solutions to the hydrodynamic conservation equations. This may be a restrictive simplification since all observed layers of the solar atmosphere are intrinsically dynamic over a wide range of time scales. It is evident, for example, that the transition region is “strongly nonuniform and magnetically structured” (Marsch et al. 2006) to the extent that one-dimensional layered models may miss some important physical effects at those heights. However, the corona above the transition region seems to exist in its hot ( $T \sim 10^6$  K) state all the time. Also, in situ measurements of the solar wind plasma often can be interpreted clearly as a superposition of a quasi-steady supersonic flow (which depends mainly on the coronal source region of the streams being measured or on stream-stream interactions) and a rapidly varying turbulent or wavelike component. We thus separate these two scales and model the fluctuations using energy conservation equations derived from linear wave theory.

It is especially beneficial to treat waves and turbulent motions statistically—rather than follow the oscillations explic-

itly in time—when the dynamically important ranges of wavelength and period span many orders of magnitude. Alfvén waves in the solar wind are measured to have periods from seconds to days (e.g., Goldstein et al. 1995; Tu & Marsch 1995) and there is evidence that the waves that dominate the dissipation in the collisionless extended corona have periods even below  $10^{-3}$  s (McKenzie et al. 1995; Cranmer et al. 1999). If this full range of scales had to be resolved in order to track the motions in a time-dependent numerical model, it would be extremely difficult to simulate the macroscopic plasma properties simultaneously from the photosphere to the heliosphere.

There are, however, some clear disadvantages in modeling fluctuations as statistical “wave energy fluxes” rather than as explicit variations. Any nonlinear processes, such as shock steepening, turbulent cascade, mode conversion, or ponderomotive forces, must be inserted beforehand as source or sink terms in the time-steady conservation equations. Time-dependent MHD models have the benefit of producing such effects naturally (e.g., Ofman & Davila 1998; Ofman 2005; Bogdan et al. 2002, 2003; Suzuki & Inutsuka 2005, 2006). However, by resolving only certain temporal and spatial scales, these models are limited in ways that a statistical treatment is not. For example, the relative importance of shock dissipation in the time-dependent models of Suzuki & Inutsuka (2005, 2006) may be an artifact of either the inability to resolve small enough scales (which could drive processes such as perpendicular cascade, Landau damping, and collisionless particle energization at shocks) or the waveguide-like trapping of fluctuations along the model flux tube. It is important to note, though, that neither extreme—i.e., neither coarse time-dependent simulations nor statistical (and more approximate) time-independent models—is ideal. There may be value in seeking some kind of hybrid methodology between these two approaches.<sup>2</sup>

As indicated above, the only source of heating for the chromosphere and corona that we consider is the dissipation of *waves and turbulent motions*. For open flux tubes, a substantial fraction of the energy appears to be deposited at large heights in the wind’s acceleration region—i.e., at spatial scales much larger than the sizes of low-lying closed loops in the quiet Sun and active regions. This demands the energy be propagated for some distance, presumably by waves or turbulent eddies, before it is dissipated. However, the general phenomenology of turbulence is probably not limited to the open-field regions. Concepts from turbulence theory have been applied to the full range of time scales for closed-field coronal energy input as well, from the most rapid (AC) wave-like oscillations to the slowest (DC) quasistatic stresses on magnetic footpoints (see van Ballegoijen 1986; Hendrix & van Hoven 1996; Milano et al. 1997; Gómez et al. 2000; Chae et al. 2002). Indeed, some recent simulations of intermittent turbulent heating in closed loops have been interpreted using similar cascade rate expressions as we use in this paper (Rappazzo et al. 2007).

The models presented below include the effects of both Alfvén waves and acoustic waves on the mean flow. We assume implicitly that all waves propagate parallel to the radially oriented flux tube, but this is not an essential feature. In the magnetically dominated corona (where  $\beta \ll 1$ ;  $\beta$  be-

<sup>2</sup> Recent advances in modeling MHD turbulence in coronal loops with a so-called “shell model” in wavenumber space may be pointing the way (e.g., Giuliani & Carbone 1998; Nigro et al. 2004).

ing the ratio of gas pressure to magnetic pressure) the modeled Alfvén waves can be considered essentially to be the sum of true Alfvénic wave power and fast-mode MHD wave power. The acoustic waves can be considered equivalent to slow-mode MHD waves. As a starting point, we neglect all nonlinear couplings between the Alfvén and acoustic wave modes. By ignoring the enhanced reflection and dissipation that may arise because of these couplings (e.g., Suzuki & Inutsuka 2005, 2006) we essentially *underestimate* the heat deposited in the extended corona and heliosphere. The fact that sufficient energy nonetheless exists to heat the corona and accelerate the wind (mainly from the Alfvén waves) appears to deemphasize the need for such mode couplings.

It should be noted that the attention given to modeling the steepening and shock dissipation of the acoustic waves (§ 4) does not seem to have much of a “payoff” in the resulting properties of the corona and solar wind. The fully ionized outer atmosphere is extremely insensitive to the magnitude (or sometimes even the presence) of acoustic wave power that comes up from below the photosphere (§ 8.2). Accordingly, many prior studies of the coupled chromosphere and corona used a much simpler prescription for maintaining the chromosphere. We believe it is important, though, to treat both the chromospheric and coronal heating at a comparable level of first-principles modeling. We also anticipate that the ZEPHYR code developed here will be applied to the simulations of winds of other late-type stars that may have acoustically heated coronae (e.g., Mullan & Cheng 1993; Schrijver 1995), and thus the acoustic waves should be treated as realistically as possible.

One final limitation of the models presented below is that the energy conservation is treated in a *one-fluid* manner. The protons, electrons, and heavy ions are modeled as having a common flow speed  $u$  and temperature  $T$ , with microscopic velocity distributions that are simple isotropic Maxwellians. This is an extreme simplification of reality, since it has been known since the 1960s that the in situ solar wind exhibits significant departures from a thermalized equilibrium (see reviews by Hundhausen 1972; Feldman & Marsch 1997). Many of these effects persist down into the extended corona as well (e.g., Kohl et al. 2006). Therefore, theoretical models have long included a range of attempts to deal with these features. Fluid-based models have been extended to solve separate conservation equations for each particle species, and they have been reconstructed in various ways based on different parameterizations for the anisotropic velocity distributions. Several purely kinetic models have also been attempted (see above-cited reviews, also Cranmer 2002; Hollweg & Isenberg 2002; Marsch 2005).

Despite the potentially clumsy “averaging” over real kinetic effects, we believe the one-fluid approach is the *most consistent with our present state of knowledge* about the primary source of energy deposition: MHD turbulent cascade. There are a number of competing ideas in the literature regarding how the cascade proceeds to its smallest kinetic scales and how either linear or nonlinear damping transfers wave energy to the particles (for a recent summary see § 5.2.4 of Kohl et al. 2006). We thus do not yet know, from first principles, how to partition the cascaded wave energy between particle species ( $T_e \neq T_p \neq T_{\text{ion}}$ ) and between various directions in microscopic velocity space ( $T_{\parallel} \neq T_{\perp}$ ). Performing such partitioning at the present time would essentially add new free parameters into the model. Our adopted rate of Alfvénic coronal heating (eq. [47]) thus deals only with the total energy flux that cas-

cades from large to small scales and not the specific means of dissipation once the energy reaches the small scales.

### 3. BASIC PHYSICS

The equations governing the expansion of a time-steady stellar wind are derivable by taking successive velocity moments of the Boltzmann equation, together with some assumption about the shape of the velocity distribution function in order to close the otherwise infinite chain of moment equations (see, e.g., Braginskii 1965; Collins 1989; Marsch 2005). In this section we describe the conservation equations used in the models (§ 3.1) and the adopted prescriptions for heat transport due to radiation (§ 3.2) and conduction (§ 3.3).

#### 3.1. Conservation Equations

We consider the flow of a pure hydrogen plasma along a radially oriented magnetic field. The goal is to solve for the time-steady radial dependence of the mass density  $\rho$ , the bulk flow speed  $u$ , and the Maxwellian temperature  $T$ . The distance along the magnetic flux tube is denoted either as  $r$ , measured from Sun-center, or  $z$ , measured from the lower boundary of the model in the solar atmosphere (essentially the photosphere). For completeness, the equations below contain the dependence on time  $t$ , though these terms are set to zero in the time-independent solutions that we describe below.

The equation of mass conservation is

$$\frac{\partial \rho}{\partial t} + \frac{1}{A} \frac{\partial}{\partial r} (\rho u A) = 0 \quad (1)$$

where  $A$  is the cross-sectional area of the one-dimensional flux tube along which the wind flows. Magnetic flux conservation demands that the product  $B_0 A$  is constant along the flux tube, where  $B_0$  is the field strength that we specify explicitly (see § 8). A time-steady one-dimensional flow thus constrains the product  $\rho u$  to be proportional to  $B_0$ .

The equation of momentum conservation is

$$\frac{\partial u}{\partial t} + u \frac{\partial u}{\partial r} + \frac{1}{\rho} \frac{\partial P}{\partial r} = -\frac{GM_*}{r^2} + D \quad (2)$$

where  $P$  is the gas pressure,  $G$  is the Newtonian gravitation constant, and  $M_*$  is the mass of the star. The mass of the plasma in the modeled stellar wind region is assumed to be negligible from a gravitational standpoint. Also,  $D$  is the bulk acceleration on the plasma due to *wave pressure*; i.e., the nondissipative net ponderomotive force due to the propagation of waves through an inhomogeneous medium (§ 6).

The equation of internal energy conservation is

$$\frac{\partial E}{\partial t} + u \frac{\partial E}{\partial r} + \left( \frac{E+P}{A} \right) \frac{\partial}{\partial r} (uA) = Q_{\text{rad}} + Q_{\text{cond}} + Q_A + Q_S \quad (3)$$

where  $E$  is the internal energy density and the terms on the right-hand side are volumetric heating/cooling rates due to radiation, conduction, Alfvén wave damping, and acoustic (sound) wave damping. The terms on the left-hand side that depend on  $u$  are responsible for enthalpy transport and adiabatic cooling in the accelerating wind. The coupling of the above equations requires additional constitutive relations to be specified:

$$P \equiv n_{\text{tot}} k_B T, \quad (4)$$

$$E \equiv \frac{P}{\gamma - 1} + n_p I_H, \quad (5)$$

$$n_{\text{tot}} \equiv n_H + n_e = (n_0 + n_p) + n_e, \quad (6)$$

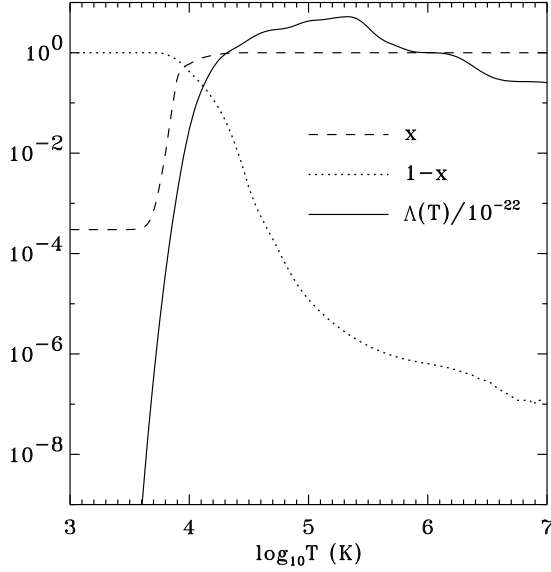


FIG. 1.— Temperature dependence of the hydrogen ionization state  $x$  (dashed line), the corresponding neutral hydrogen fraction  $1-x$  (dotted line), and the optically thin radiative loss function  $\Lambda(T)$  in units of  $10^{-22}$  erg  $\text{cm}^3$   $\text{s}^{-1}$  (solid line).

where  $k_B$  is Boltzmann's constant and a monatomic ratio of specific heats  $\gamma = 5/3$  is used. The total particle number density  $n_{\text{tot}}$  is given by the sum of the hydrogen number density  $n_H$  and the electron density  $n_e$ , and the number densities of neutral hydrogen and protons are denoted  $n_0$  and  $n_p$ , respectively. For the pure hydrogen plasma assumed in this paper,  $n_p = n_e$ . The mass density is given by  $\rho = m_H n_H + m_e n_e$ , although the second term is safely considered to be negligible.

Note that equation (5) becomes the ideal gas relation  $E = 3P/2 = \rho c_v T$  in the purely neutral limit, where  $c_v$  is the specific heat at constant volume. Ionization is taken into account by the internal energy's dependence on  $I_H$ , the ionization potential of hydrogen from the ground level (13.6 eV). We use the same convention in the definition of  $E$  as Ulmschneider & Muchmore (1986) and Mullan & Cheng (1993). An alternate definition of the internal energy is possible, though, which is essentially given by  $E - n_H I_H$ . This version reduces to the above ideal-gas relation in the limit of a fully ionized plasma (e.g., McClymont & Canfield 1983; Fontenla et al. 1990). Either definition is consistent with the combined equations of mass and energy conservation given above.

We adopted a relatively simple prescription to compute the ionization fraction  $x \equiv n_p/n_H$ . This quantity is parameterized as a tabulated function of  $T$  only, where we have used the ionization balance from a recent semi-empirical model of the solar photosphere, chromosphere, and transition region (E. Avrett 2005, private communication; see also Fontenla et al. 1993, 2002, 2006). The tabulated model we use is a modified version of the quiet-Sun model C from the above papers, and it is the same one used by Cranmer & van Ballegoijen (2005) to model the magnetic structure of the chromospheric network. For convenience we call this model FAL-C'.

Figure 1 shows the adopted ionization fraction  $x$ , as well as the corresponding neutral fraction  $1-x$  (in order to see small departures from total ionization at high temperatures) and the radiative cooling function that was derived in part from the FAL-C' model (see § 3.2). For temperatures below the minimum tabulated value of about 4500 K, we prevent  $x$  from decreasing below a minimum value of  $3 \times 10^{-4}$ , because pho-

toionization is expected to always keep some small fraction of metals ionized at and above the photosphere.

We tested the ZEPHYR code with a more self-consistent model of the hydrogen ionization balance. The results were extremely similar, though, to those using the tabulated fraction shown in Figure 1. This model consisted of a three-level hydrogen atom, where the  $n = 1$  and  $n = 2$  levels were assumed to remain in relative local thermodynamic equilibrium (LTE) and the full rate equation between  $n = 2$  and the continuum was solved iteratively with collisional and radiative terms from Hartmann & MacGregor (1980), Vriens & Smeets (1980), Ferland et al. (1992), and Ferguson & Ferland (1997). Because the tabulated version was much faster in terms of computation time, though, we decided to use it in the models shown below. It will be important to include this kind of self-consistent ionization balance when adapting this method to the winds of other stars (e.g., Natta et al. 1988).

### 3.2. Radiative Heating and Cooling

A complete treatment of the non-LTE transfer of energy between radiation and matter in a partially ionized plasma is beyond the scope of this paper. Detailed computational efforts to model chromospheric and coronal radiative transfer effects (e.g., Avrett & Loeser 1992; Carlsson & Stein 1997, 2002; Rammacher et al. 2005) are important for reproducing the spectrum or studying time-dependent or multidimensional dynamics, but for our purposes a simpler treatment is warranted. We use a similar general “bridging” approach as Mullan & Cheng (1993) to combine different limiting cases in the optically thick lower atmosphere and the optically thin upper atmosphere.

The adopted radiative heating/cooling rate is given by

$$Q_{\text{rad}} = e^{-\tau_R/\tau_0} Q_{\text{thin}} + (1 - e^{-\tau_R/\tau_0}) Q_{\text{thick}} \quad (7)$$

where  $\tau_R$  is the Rosseland mean optical depth and  $\tau_0 = 0.1$  is a constant that defines where the rate is dominated by the optically thick or thin limits (see also Ludwig et al. 1994). For a spherical stellar atmosphere, we use a definition for the Rosseland optical depth,

$$d\tau_R = -\kappa_R \rho \left( \frac{R_*}{r} \right)^2 dr, \quad (8)$$

that contains the geometrical correction factor suggested by Lucy (1971, 1976); it is unimportant in the case of the Sun—where  $r \approx R_*$  in regions where  $\tau_R \approx 1$ —but we include it for later use in the extended atmospheres of evolved stars. The Rosseland mean opacity  $\kappa_R$  (in  $\text{cm}^2 \text{g}^{-1}$ ) is interpolated as a function of temperature and pressure from the table of Kurucz (1992). For a given one-dimensional model, we integrate downward from the upper boundary far out in the supersonic wind (which has an assumed optical depth of zero) to compute  $\tau_R(r)$ .

In the optically thick photosphere and lower chromosphere we assume that the heating and cooling is dominated by continuum photons emitted and absorbed in LTE, with

$$Q_{\text{thick}} = 4\pi\rho \int \kappa_\nu (J_\nu - S_\nu) d\nu = 4\pi\rho\kappa_R (J - S) \quad (9)$$

(e.g., Mihalas 1978; Vögler et al. 2004). Above,  $S$  is the frequency-integrated source function, assumed here in LTE to equal the local integrated Planck function,  $S = B = \sigma_R T^4/\pi$ , with  $\sigma_R$  being the Stefan-Boltzmann constant. The frequency-integrated mean intensity  $J$  is given by the gray atmosphere

dependence on optical depth  $\tau_R$ ,

$$J(\tau_R) = \frac{3}{4\pi} \sigma_R T_{\text{eff}}^4 [\tau_R + 2q(\tau_R)W(r)] , \quad (10)$$

where  $T_{\text{eff}} = 5800$  K is the solar effective temperature and  $q(\tau)$  is the Hopf (1930, 1932) function, for which we use the following fit (accurate to better than 0.2%),

$$q(\tau) = 0.710 - \frac{0.133}{(1 + 0.15\tau^{0.73})^{17.4}} . \quad (11)$$

Also,  $W(r) = [1 - (1 - R_*^2/r^2)^{1/2}]/2$  is the spherical dilution factor suggested for use in this context by Chandrasekhar (1934) and Lucy (1971, 1976).  $Q_{\text{thick}}$  is positive—giving net heating—when  $T$  is less than the radiative equilibrium temperature ( $T_{\text{rad}}$ ) given by  $J = S$ , and it is negative—with net cooling—when  $T > T_{\text{rad}}$ .

In the optically thin upper chromosphere and corona, we use a modified temperature-dependent radiative cooling function that has been computed for photon losses due to a large collection of spectral lines and continuum processes,

$$Q_{\text{thin}} = -n_e n_H \Lambda(T) \left( 1 - \frac{T_{\text{rad}}^4}{T^4} \right) \quad (12)$$

(see also Cox & Tucker 1969; Anderson & Athay 1989b; Schmutzler & Tscharnuter 1993). The radiative loss function  $\Lambda(T)$  is shown in Figure 1, and it has been assembled from three sources. (1) For hydrogen and helium above  $10^4$  K, we used the output from the PANDORA radiative transfer code which produced the FAL-C' semi-empirical model discussed above. (2) For other elements above  $10^4$  K, we used a tabulated radiative loss function from version 4.2 of the CHIANTI atomic database (Young et al. 2003) using a traditional solar abundance mixture (Grevesse & Sauval 1998) and collisional ionization balance (Mazzotta et al. 1998). (3) For temperatures below  $10^4$  K, we used the fitting function for partially ionized hydrogen given by Scholz & Waters (1991). For these low temperatures we also added a constant lower-limit value of  $10^{-34}$  erg cm<sup>3</sup> s<sup>-1</sup> to  $\Lambda(T)$  to account for photoionized metals, molecules, and dust, which may be important contributors to radiative cooling at very low temperatures in late-type stellar atmospheres (e.g., Schirmacher et al. 2003).

In order to ensure that the optically thin parts of the atmosphere would smoothly approach radiative equilibrium (in the absence of nonradiative heating) in the same way as in the optically thick parts of the atmosphere, we multiplied the standard cooling function by the term in parentheses in equation (12). For temperatures above  $\sim 2T_{\text{rad}}$  this correction factor rapidly approaches unity.

Note from Figure 1 that there is no isolated “Lyman alpha peak” at temperatures of  $1\text{--}2 \times 10^4$  K. For solar atmosphere models, this peak seems to be a spurious feature that appears in optically thin radiative loss curves computed without a radiation field. The FAL-C' model used here contained a full non-LTE treatment of hydrogen as well as ambipolar diffusion that also provides additional smearing of discrete features related to the strong H I Ly $\alpha$  transition (see also Kuin & Poland 1991; Fontenla et al. 2002).

With regard to the extension to other stars, the computation of the radiative cooling rate is in a similar situation as the ionization fraction discussed in § 3.1. Our use of tabulated quantities from FAL-C' seems to be reasonable for modeling the solar atmosphere, but it will eventually need to be replaced with a more self-consistent procedure. Specifically, evolved

low-gravity stars with high mass loss rates are expected to have more optically thick chromospheres. Hartmann & MacGregor (1980), Canfield & Ricchiazzi (1980), and Mullan & Cheng (1993) computed approximate optically thick radiation losses by taking account of reduced escape probabilities in the damping wings of strong lines; it is possible that these methods can be extended in a robust way to future time-steady stellar wind models.

### 3.3. Heat Conduction

For the radially oriented flux tubes that we consider, the conductive energy exchange rate is dominated by the divergence of a parallel heat flux density, i.e.,

$$Q_{\text{cond}} = -\frac{1}{A} \frac{\partial}{\partial r} (q_{\parallel} A) . \quad (13)$$

Because the solar atmosphere undergoes a transition from being strongly collisionally coupled (at low heights and high densities) to being nearly collisionless (at large heights and low densities), it was realized long ago that the classical Spitzer-Härm (SH) prescription for thermal conductivity must break down somewhere in the corona and solar wind. We thus follow Wang (1993), and others, by using a semi-empirical bridging law between the SH heat flux  $q_{\text{SH}}$  and a completely collisionless “free-streaming” heat flux  $q_{\text{FS}}$ ,

$$q_{\parallel} = \frac{\nu_{\text{coll}} q_{\text{SH}} + \nu_{\text{exp}} q_{\text{FS}}}{\nu_{\text{coll}} + \nu_{\text{exp}}} \quad (14)$$

where  $\nu_{\text{exp}} = (u/\rho)|\partial\rho/\partial r|$  is the local wind expansion rate and  $\nu_{\text{coll}}$  is the electron-electron Coulomb collision frequency,

$$\nu_{\text{coll}} = \frac{\ln \Lambda_{ee}}{275 \text{ s}} \left( \frac{n_e}{10^6 \text{ cm}^{-3}} \right) \left( \frac{T}{10^6 \text{ K}} \right)^{-3/2} \quad (15)$$

(Braginskii 1965; Olsen & Leer 1996). The electron Coulomb logarithm is approximated by

$$\ln \Lambda_{ee} = 23.2 + \frac{3}{2} \ln \left( \frac{T}{10^6 \text{ K}} \right) - \frac{1}{2} \ln \left( \frac{n_e}{10^6 \text{ cm}^{-3}} \right) . \quad (16)$$

A more accurate version of equation (14) was derived by Cuperman & Dryer (1985). Under a number of simplifying approximations, though (such as nearly Maxwellian distributions), their expression reduces to something very close to the above bridging formula.

The radial distance where the heat flux undergoes the transition from collisional to collisionless can be estimated by locating the point at which  $\nu_{\text{exp}} = \nu_{\text{coll}}$ . For the models of low-density high-speed solar wind streams presented below, this occurs at about  $r \approx 10$  solar radii ( $R_{\odot}$ ); for the models of high-density low-speed solar wind, this occurs at  $r \approx 50\text{--}80 R_{\odot}$ .

In the collisionally dominated limit, we assume SH conduction,

$$q_{\text{SH}} = -\kappa \frac{\partial T}{\partial r} \quad (17)$$

where the thermal conductivity is assumed to be dominated by contributions from free electrons and neutral hydrogen,  $\kappa = F\kappa_e + \kappa_H$  (e.g., Nowak & Ulmschneider 1977; McClymont & Canfield 1983). The effects of protons and heavy ions are neglected because they tend to be overwhelmed by the electron conductivity in regions of appreciable ionization (see also Ulmschneider 1970; Hansteen & Leer 1995). The electron conductivity is given by

$$\kappa_e = (1.84 \times 10^{-5} \text{ erg cm}^{-1} \text{ s}^{-1} \text{ K}^{-7/2}) \frac{T^{5/2}}{\ln \Lambda_{ee}} \quad (18)$$

(Spitzer 1962; Braginskii 1965). Partial ionization effects (i.e.,  $F$  and  $\kappa_H$ ) are parameterized using the results of Shmel'eva & Syrovatskii (1973) and McClymont & Canfield (1983), with

$$F = \frac{1 + 4.49w + 3.37w^2 + 0.59w^3}{(1 + 3.86w + 0.94w^2)^2}, \quad (19)$$

where  $w$  is the ratio of the electron-electron collision time  $\tau_{ee}$  to the electron-neutral hydrogen time  $\tau_{e0}$ , and

$$w = \frac{\tau_{ee}}{\tau_{e0}} = \frac{n_0}{n_e \ln \Lambda_{ee}} \left( \frac{T}{52705 \text{ K}} \right)^2. \quad (20)$$

Similarly, the neutral hydrogen conductivity is given by

$$\kappa_H = \frac{29.6T}{1 + (n_p/n_0)(T/7.6 \times 10^5 \text{ K})^{-1/2}}. \quad (21)$$

The above partial ionization effects are generally unimportant in the solar atmosphere, but we include them for some attempt at completeness, and with anticipation that the cooler and more optically thick chromospheres of other stars may depend more sensitively on them.

In the collisionless limit we use the free-streaming heat flux derived for escaping electrons by Hollweg (1974, 1976), which was based on empirical constraints from Forslund (1970) and Perkins (1973) on the electron velocity distribution,

$$q_{FS} = \frac{3}{2} \alpha_c n_e u k_B T, \quad (22)$$

where  $\alpha_c$  is an order-unity correction factor that depends on how the wings of the electron velocity distribution depart from a Maxwellian shape. We take a constant value of  $\alpha_c = 4$  as has been often used in solar wind modeling (see, e.g., Leer et al. 1982; Scudder & Olbert 1983; Withbroe 1988; Canullo et al. 1996; Landi & Pantellini 2003). Tests using Hollweg's (1974) more detailed prescription for how  $\alpha_c$  should depend on the solar wind speed and electron temperature produced no more than a 10% change in  $T(r)$  from the  $\alpha_c = 4$  model (and no more than a 2% change in the mass loss rate or terminal wind speed). The simpler constant value was used in all subsequent ZEPHYR models.

Note that equations (14) and (22) are in some ways similar to the heat flux relations used by Smith & Auer (1980) and others for flare plasmas, where the classical heat flux is assumed to *saturate* at a value no larger than a threshold flux proportional to  $v_e^3$  (where  $v_e$  is the electron thermal speed). The free-streaming heat flux given above is dimensionally similar to the saturated heat flux, but the former is proportional to  $uv_e^2$  rather than  $v_e^3$ . These two limits are related, though, because saturation occurs when the electron-electron collisional mean free path becomes larger than the local temperature scale height. When heat can no longer be carried diffusively by classical conduction, it may be advected directly at some characteristic velocity  $v_c$ , and the heat flux then becomes proportional to  $v_c v_e^2$ . In the low-density supersonic solar wind, the characteristic speed for, e.g., the total enthalpy flux is  $v_c \approx u$ . To the extent that  $\alpha_c$  is an order-unity correction factor (that depends weakly on  $v_e$ ), this applies also to the heat flux carried in the non-Maxwellian tail of the electron distribution. For a high-density laboratory plasma, though, Mannheimer & Klein (1975) showed that  $v_c$  scales directly with  $v_e$  (see also Smith & Lilliequist 1979; Craig & Davys 1984).

#### 4. ACOUSTIC WAVES AND SHOCKS

We include the time-averaged effects of acoustic waves that propagate parallel to the magnetic field. The only source of these waves that we consider is the convective motion below the photosphere which channels compressive wave energy into the magnetic flux tubes. Deep in the atmosphere these fluctuations take the form of longitudinal, or sausage-mode tube waves (e.g., Spruit 1982; Roberts 2000), but because the individual flux tubes appear to merge together somewhere in the low chromosphere into a region filled with magnetic field (Cranmer & van Ballegoijen 2005) we treat these waves as standard acoustic oscillations and do not consider thin-tube dispersive effects. A separate source of compressive waves, which we do not model, may be the gradual parametric decay of nonlinear MHD waves in the outflowing stellar wind (see Sagdeev & Galeev 1969; Goldstein 1978; Jayanti & Hollweg 1993). It is usually assumed that these waves have very low frequencies and thus are likely to have small rates of damping and steepening, and thus a minimal impact on chromospheric or coronal heating.<sup>3</sup>

Below we describe how ZEPHYR models the propagation, steepening, and dissipation of individual monochromatic "packets" of acoustic wave energy (§ 4.1) and how the complete power spectrum is specified (§ 4.2).

##### 4.1. Monochromatic Wave Train Evolution

An arbitrarily steepened acoustic wave/shock train travels along the field with constant frequency  $\omega$  and a radially varying wavenumber  $k_{\parallel}$  determined by the dispersion relation  $\omega = (u + c_s)k_{\parallel}$ . The sound speed is given by  $c_s^2 = \gamma P / \rho$ . The energy density  $U_S$  of linear acoustic fluctuations obeys an equation of wave action conservation,

$$\frac{\partial}{\partial t} \left( \frac{U_S}{\omega'} \right) + \frac{1}{A} \frac{\partial}{\partial r} \left[ \frac{(u + c_s) A U_S}{\omega'} \right] = - \frac{Q_S}{\omega'} \quad (23)$$

(e.g., Jacques 1977; Koninx 1992). The Doppler shifted frequency in the frame of the accelerating wind is given by  $\omega' = \omega - uk_{\parallel}$  and the wave energy density is given by

$$U_S = \frac{1}{s} \rho v_{\parallel}^2 \quad (24)$$

where  $s$  is a dimensionless shape factor determined by the spatial profile of the waves (see below). For a small-amplitude sinusoid,  $s = 2$ , and for a fully steepened sawtooth or N-wave,  $s = 3$ . The parallel velocity variance, or squared wave amplitude, is specified as  $v_{\parallel}^2$ . Below we give the wave energy flux  $F_S$  as a lower boundary condition for the ZEPHYR code; this quantity is converted into wave energy density using

$$F_S = \left[ \frac{(\gamma + 3)u}{2} + c_s \right] U_S. \quad (25)$$

Note that in the limit of a static plane-parallel atmosphere ( $u = 0$  and  $A = \text{constant}$ ) equations (23)–(25) simplify into the standard flux conservation quantities implicit in wave-heated models of the solar atmosphere since the initial work of Schwarzschild (1948), Biermann (1948), and Osterbrock (1961).

<sup>3</sup> See, though, Suzuki & Inutsuka (2005) for an example of naturally produced compressive waves by similar nonlinear couplings. This kind of process could account for a substantial fraction of the low-frequency density fluctuations measured in interplanetary space by in situ spacecraft and radio scintillations.

The right-hand side of equation (23) couples the dissipation of acoustic wave energy to the  $Q_S$  heating term in equation (3). We include two sources of wave damping: heat conduction and entropy gain at shock discontinuities. For the present models we ignore radiation damping of the waves (which damps high frequencies at low heights, but does not technically provide heat to the plasma), viscosity, and ion-neutral friction. The acoustic heating rate is given by

$$Q_S = 2\gamma_{\text{cond}} U_S + \frac{\rho T \Delta S}{2\pi/\omega}, \quad (26)$$

where  $\gamma_{\text{cond}}$  is the linear damping rate due to heat conduction and  $\Delta S$  is the net entropy jump across a shock (which is nonzero only above the height where the wave train has steepened into shocks).

The damping rate due to heat conduction is given for adiabatic waves ( $\gamma = 5/3$ ) by

$$\gamma_{\text{cond}} = \frac{4\omega^2 \kappa}{15k_B c_s^2 n_H} \quad (27)$$

(e.g., Landau & Lifshitz 1959; Hung & Barnes 1973; Whang 1997). We use the same thermal conductivity  $\kappa$  as is used in the classical SH heat flux (eq. [17]). For simplicity, the electron and neutral hydrogen conductivities are assumed to dominate proton and heavy ion heat conduction as well as other classical transport processes. Note that  $\gamma_{\text{cond}}$  is the damping rate for the wave amplitude; the damping rate for wave energy is twice that value (see the factor of 2 in eq. [26]).

The major contribution to the acoustic heating rate comes from shock steepening and dissipation. The gain in internal energy across an ideal inviscid shock is given by

$$T \Delta S = c_v \left[ T_2 - T_1 \left( \rho_2 / \rho_1 \right)^{\gamma-1} \right] \quad (28)$$

where subscripts 1 and 2 denote quantities measured on the upstream (supersonic) and downstream (subsonic) sides of the shock (Landau & Lifshitz 1959). The above expression does not contain the internal energy component from  $P\Delta V$  work but only the energy that goes into dissipation. Equation (26) uses the approximation from so-called “weak-shock theory” that the volumetric heating rate is given by the internal energy dissipated at one shock divided by the mean time between shock passages in a periodic train. This assumption breaks down for very strong shocks in the chromosphere, which dissipate their energy in a relatively narrow zone behind the shock (e.g., Carlsson & Stein 1992, 1997), but the models presented below do not develop such strong shocks.

To evaluate equation (28) we used the classical Rankine-Hugoniot relations for a monatomic ( $\gamma = 5/3$ ) gas. These relations also are valid for a plasma with a constant ionization state across the shock, and Carlsson & Stein (2002) found that shock trains in the solar chromosphere often approach this nearly steady-state condition. The density and temperature jump relations can be written in terms of the upstream Mach number  $M_1$ ,

$$\frac{\rho_2}{\rho_1} = \frac{(\gamma+1)M_1^2}{(\gamma-1)M_1^2+2} \quad (29)$$

$$\frac{T_2}{T_1} = \frac{[2\gamma M_1^2 - (\gamma-1)][(\gamma-1)M_1^2 + 2]}{(\gamma+1)^2 M_1^2} \quad (30)$$

Note, though, that for shocks of arbitrary strength, equation (28) requires the absolute upstream and downstream temperatures  $T_1$  and  $T_2$  to be computed, not just their ratio. (In the

weak-shock limit,  $T_1 \approx T_2 \approx T$ , the latter being the “mean” model atmospheric temperature.) In many astrophysical models of shocks,  $T_1$  is often assumed to be the undisturbed equilibrium state and  $T_2$  is computed from equation (30). However, in time-dependent simulations of chromospheric shocks,  $T_1$  is often seen to fall *below* the time-averaged mean temperature  $T$  and often also below the radiative equilibrium value  $T_{\text{rad}} \approx 4500$  K. This is believed to arise from adiabatic expansion behind the shock.

To compute  $T_1$  and  $T_2$ , we first determine the upstream and downstream densities  $\rho_1$  and  $\rho_2$  relative to the known background model density  $\rho$ . With respect to the propagating shock train, the background density can be defined as that which occurs when the shock passes through zero velocity in the reference frame of the undisturbed atmosphere. For an ideal sawtooth-shaped N-wave, this occurs for a given height at a time halfway between shock passages. Using this definition, the analytic results of Bertschinger & Chevalier (1985) can be used to estimate the ratio of the minimum (preshock) density to the background value to be

$$\frac{\rho_1}{\rho} = \frac{1 + (\rho_2/\rho_1)}{2(\rho_2/\rho_1)} \quad (31)$$

which then allows both  $\rho_1$  and  $\rho_2$  to be computed. To convert densities into temperatures, some knowledge of the thermodynamic cycle of the shock must be incorporated. In other words, after the gas is heated and compressed, we need to know what “path” it takes as it cools and expands back to the preshock values, in order to be heated and compressed again as the next shock in the train goes by. Nearly all time-dependent models of periodic shocks in stellar atmospheres have found that shocks first undergo rapid radiative cooling at a roughly constant density, followed by nearly adiabatic expansion back to the preshock density and temperature (e.g., Weymann 1960; Osterbrock 1961; Ulmschneider et al. 1978; Bowen 1988). This second phase seems to dominate the time between shock passages—usually encompassing the halfway point used above as the definition for the undisturbed density—so we assume that the cooling from the mean temperature  $T$  to the preshock, or upstream temperature  $T_1$  is adiabatic, and

$$T_1/T = (\rho_1/\rho)^{\gamma-1}. \quad (32)$$

This, in combination with equations (29)–(31), completes the specification of  $T_1$  and  $T_2$  needed to compute  $T \Delta S$ .

In the limit of low-amplitude shocks (i.e.,  $M_1^2 \approx 1 + m$ , where  $m \ll 1$ ), equation (28) reduces to the standard weak-shock limit

$$T \Delta S \approx \frac{2\gamma(\gamma-1)}{3(\gamma+1)^2} c_v m^3 T \quad (33)$$

(e.g., Ulmschneider 1970; Stein & Schwartz 1972, 1973; Mihalas & Mihalas 1984). In the strong-shock limit ( $M_1 \gg 1$  and  $\rho_2/\rho_1 \rightarrow 4$ ), the ratio  $T_1/T$  approaches a constant value of  $(5/8)^{2/3} \approx 0.73$  and  $T_2$  grows without bound. The first term of equation (28) dominates the second and

$$T \Delta S \approx c_v T_2 \approx 0.228 c_v M_1^2 T. \quad (34)$$

The weak and strong limiting expressions are valid to within about 25% of the exact result for  $M_1 < 1.2$  and  $M_1 > 4.6$ , respectively. Because the peak Mach numbers of the shock trains in the ZEPHYR models shown below are typically outside these ranges (i.e.,  $M_1 \approx 2$ ) we use the full procedure described by equations (28)–(32), which is valid for shocks of arbitrary strength.

In order to incorporate the shock dissipation into the acoustic wave transport equation, the wave amplitude  $v_{\parallel}$  must be converted, where appropriate, into the Mach number  $M_1$ . We must take account of how the initially sinusoidal wave profile steepens into a sawtooth shock train. Often shock heating is applied only above an estimated shock formation height. However, there exists a finite range of heights between the first formation of the shock (i.e., where the acoustic wave train first “breaks”) and the height where the shock train has evolved into a complete sawtooth shape. Between these heights the velocity amplitude of the shock may only be a fraction of the crest-to-trough velocity amplitude of the wave.

To solve for the wave evolution and dissipation in this region, we have computed numerical profiles of both the shape factor  $s$  and a steepening efficiency factor  $\varepsilon$ . These quantities are computed as a function of a dimensionless steepening parameter  $\zeta$ , which measures by how much a wave crest is approaching (or has overtaken) the zero-velocity node immediately ahead of it.<sup>4</sup> The efficiency  $\varepsilon$  is defined as the ratio of the shock velocity amplitude to the full velocity amplitude of the (arbitrarily steepened) wave profile, and we define

$$M_1 = 1 + \left( \frac{\gamma+1}{2} \right) \frac{\varepsilon v_{\parallel}}{c_s}. \quad (35)$$

Where the wave is still a sinusoid,  $\varepsilon = 0$  and  $M_1 = 1$ , which results in no heating. As the wave steepens,  $\varepsilon$  grows from 0 to 1. At each radial grid zone, we compute the crest-to-node distance factor  $\zeta \equiv \Delta z / \lambda$ , where  $\lambda$  is the local parallel wavelength and

$$\Delta z = \frac{\lambda_0}{4} - \frac{\gamma+1}{2} \int \frac{v_{\parallel} dz}{c_s}, \quad (36)$$

where the integration is taken from the lower boundary (at which  $\lambda = \lambda_0$ ) up to an arbitrary height. By computing this quantity point-by-point along the grid, the atmospheric stratification is taken into account accurately. At the lower boundary, the wave profile is assumed to be a perfect sinusoid, and  $\zeta = 1/4$ . This quantity decreases steadily as the wave train propagates upward and steepens. When  $\zeta$  reaches zero, the shock amplitude has grown to be equal to the wave amplitude and the profile is assumed to remain a sawtooth as it propagates upward. We continue to follow the ever-decreasing  $\zeta$  to values below zero, though, because the profile only reaches the exact sawtooth “N-wave” shape in the limit of  $\zeta \rightarrow -\infty$ .

Figure 2 shows the normalized phase function  $\Phi(\phi)$  of a gradually steepening acoustic wave, where the phase  $\phi$  is defined at a given (constant) height as  $\pi - \omega t$ ; it varies from  $-\pi$  to  $\pi$ . Figure 2 also plots the efficiency  $\varepsilon$  and the shape factor  $s$  as a function of  $\zeta$ . These have been derived from numerical simulations of this steepening sinusoidal wave profile, and we give parameterized fits (used by the ZEPHYR code) below. The fit to the efficiency is given by

$$\varepsilon(\zeta) = \begin{cases} 1 & \zeta \leq 0 \\ \sqrt{1 - (\zeta/\zeta_0)^{3.1}} & 0 < \zeta < \zeta_0 \\ 0 & \zeta \geq \zeta_0 \end{cases}. \quad (37)$$

The constant  $\zeta_0$  denotes the critical breakpoint at which the wave train first steepens to infinite slope at the node ahead of the crest; it is defined as  $\zeta_0 \equiv (\pi - 2)/4\pi \approx 0.091$ . Note that as  $\zeta$  decreases from 0.25 to  $\zeta_0$ , the efficiency  $\varepsilon$  remains

<sup>4</sup> The node propagates exactly at the linear phase speed, and the crest propagates faster by a nonlinear factor proportional to the wave amplitude  $v_{\parallel}$ .

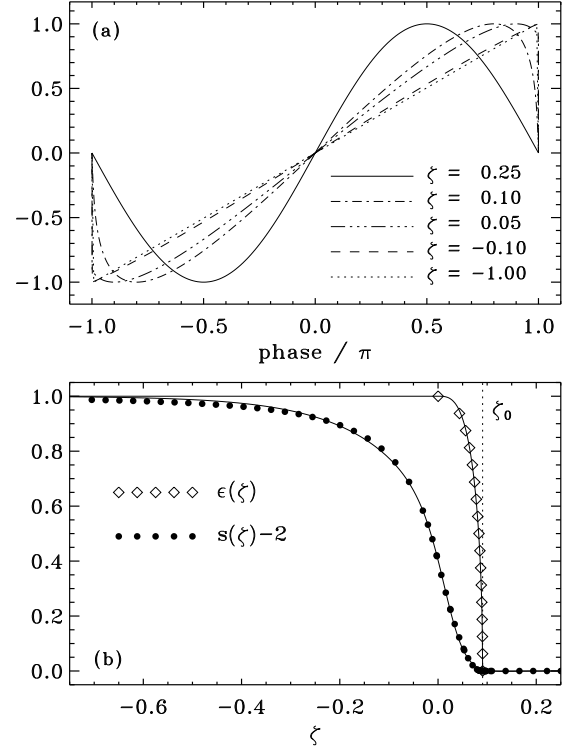


FIG. 2.— Properties of steepened acoustic waveforms. (a) Normalized phase function  $\Phi$  as a function of the dimensionless wave phase  $\phi$  (in units of  $\pi$ ) for a series of steepening parameters  $\zeta$  (see labels for values). (b) Steepening efficiency ratio  $\varepsilon$  (open diamonds) and scaled shape factor  $s-2$  (filled circles) computed numerically for a series of values of  $\zeta$ . Solid lines show the analytic fitting functions given in the text.

zero because no shock transition has yet formed. Only when  $\zeta$  decreases below  $\zeta_0$  does there exist a shock with a finite strength.

The shape factor  $s$  is used to convert between wave amplitude and energy density (eq. [24]), and it is defined as the inverse of the phase-averaged square of the normalized phase function, i.e.,

$$\frac{1}{s} = \frac{1}{2\pi} \int_{-\pi}^{+\pi} d\phi [\Phi(\phi)]^2 \quad (38)$$

(see also Koninx 1992; Suzuki 2004). As an example, for a sinusoid the average of  $\sin^2 \phi$  over a full period is  $1/2$ , and thus  $s = 2$ . We found the following fit from a series of simulated wave profiles undergoing gradual steepening,

$$s(\zeta) = 3 - \frac{1 + 1.32e^{-37.5\zeta}}{1 + 2.89e^{-44.7\zeta}} \quad (39)$$

(see Figure 2 for a comparison between the numerically determined values and the fit). For most of the pre-break steepening (i.e., from  $\zeta = 0.25$  down to  $\zeta_0$ )  $s$  remains close to 2. Note, though, that when the shock grows to full amplitude at  $\zeta = 0$  the shape factor has increased only to about 2.4. The additional increase up to 3 occurs for negative values of  $\zeta$ .

#### 4.2. Acoustic Power Spectrum

The convection zone generates a continuous spectrum of acoustic power, and we need to specify this distribution of energy as a function of frequency at the photospheric base of the model. The power spectrum at larger heights is determined implicitly as a result of solving the monochromatic wave action conservation equations (eq. [23]) for a range of



frequencies. The continuous power spectrum  $P_S(\omega)$  is defined at the base in units of the photospheric acoustic flux, with

$$F_S = \int d\omega P_S(\omega). \quad (40)$$

For waves that escape into the upper atmosphere, there should be negligible power at frequencies below the acoustic cutoff,

$$\omega_{ac} \equiv \frac{\gamma g}{2c_s}, \quad (41)$$

because waves having  $\omega < \omega_{ac}$  are evanescent in an ideal hydrostatic atmosphere (e.g., Mihalas & Mihalas 1984; see, however, Wang et al. 1995; Schmitz & Fleck 1998). We used a constant value of  $\omega_{ac} = 0.03 \text{ rad s}^{-1}$  (i.e.,  $f \approx 4.8 \text{ mHz}$ , or a period of 3.5 minutes), which corresponds to temperature-minimum conditions in the upper photosphere. From a theoretical standpoint, this value is slightly on the high side, since the photospheric  $T_{\text{eff}}$  of 5800 K gives a cutoff frequency about 13% lower. Our higher value for  $\omega_{ac}$  is an attempt to ensure that the modeled frequencies are those that should be propagating *everywhere* in the model—i.e., since we do not treat evanescent energy loss, we want to include only waves that can make it through both the photosphere and the temperature minimum region without becoming evanescent. Note, though, that from the standpoint of observational helioseismology, our value is slightly on the low side (e.g., Jiménez 2006), so it seems to be a satisfactory median value.

The shape of the power spectrum above the cutoff is a subject of some ongoing controversy, which we do not attempt to address fully. The presence of substantial power at high frequencies ( $f \gtrsim 20 \text{ mHz}$ ) is predicted by traditional theories of sound generation from turbulent convection (e.g., Lighthill 1952; Stein 1967; Musielak et al. 1994; Ulmschneider et al. 1996) and also by observational inferences of time-steady chromospheric heating (Kalkofen et al. 1999; Ulmschneider et al. 2005; Cuntz et al. 2007). However, evidence also exists that there may be an extremely steep decline in the acoustic power spectrum before frequencies of order 20 mHz are reached, and thus that high frequencies would not be important to atmospheric heating (e.g., Judge et al. 2003; Fossum & Carlsson 2005, 2006). Recent advances in detecting high-frequency acoustic fluctuations have been made by Wunnenberg et al. (2002), DeForest (2004), Muglach (2006), and van Noort & Rouppe van der Voort (2006), but no firm conclusions yet exist regarding their impact on chromospheric heating. Future observations with higher spatial and temporal resolution are definitely needed.

Provisionally, we model  $P_S(\omega)$  with a high-frequency tail reminiscent of the turbulent convection theories cited above. The following parameterization

$$P_S(\omega) \propto \begin{cases} (\omega/\omega_{\text{max}})^\psi / [1 + (\omega/\omega_{\text{max}})^{2\psi}] & \omega \geq \omega_{ac} \\ 0 & \omega < \omega_{ac} \end{cases} \quad (42)$$

has finite power at the cutoff, a peak value at  $\omega_{\text{max}} > \omega_{ac}$ , and a declining tail with  $P_S \propto \omega^{-\psi}$  at high frequencies. Typically,  $\psi \approx 3$  and  $\omega_{\text{max}}$  is a factor of 2 to 5 larger than  $\omega_{ac}$ . The normalization is given by specifying a known value of  $F_S$  and using equation (40).

Figure 3 illustrates the shape of the acoustic power spectrum that is used in all of the solar models described in this paper. We use constant values of  $\omega_{\text{max}}/\omega_{ac} = 3$  and  $\psi = 2.5$ . The adopted value of  $\psi$  is the most sensitive to the controversy over high-frequency acoustic waves, and it deserves further discussion. The standard Lagrangian treatment of the

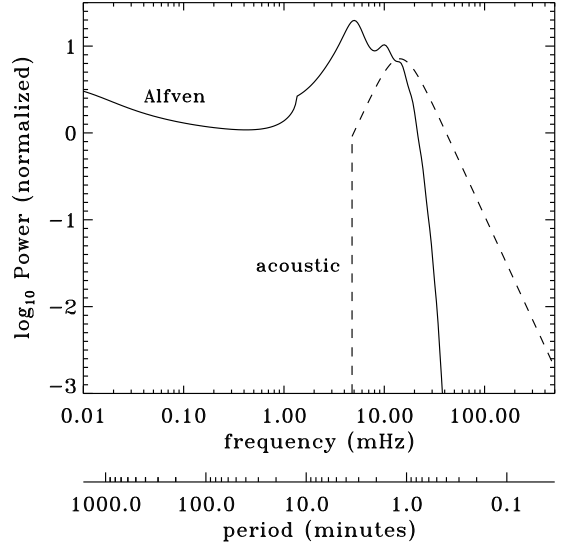


FIG. 3.— Normalized power spectra for Alfvén waves  $P_A$  (solid line) and acoustic waves  $P_S$  (dashed line). The cyclic frequency  $f = \omega/2\pi$  is given in units of mHz, and the period  $p = 1/f$  is given in units of minutes.

Lighthill-Stein sound generation mechanism tends to give values of  $\psi$  between 3 and 3.5 in the high-frequency limit for both acoustic and longitudinal flux-tube waves (Ulmschneider et al. 1996; Musielak et al. 2000). However, an alternate Eulerian treatment of the turbulent correlations (Rubinstein & Zhou 2002) yielded a much shallower decline with increasing frequency;  $\psi \approx 1.3$ –2.4. We also note that the value  $\psi = 3$  is a special case that corresponds to frequency-independent shock steepening for the discrete bins that we use (see below); i.e., when  $\psi = 3$  the increase in frequency from one bin to the next is balanced exactly by the power decrease, such that the wave train in each bin steepens into a shock train at the same height. We find that a realistic chromospheric temperature rise occurs only when higher frequency waves steepen at successively lower heights (which requires  $\psi < 3$ ). Our value of 2.5 satisfies this requirement while being only slightly lower than the range predicted by traditional Lighthill-Stein theory.

In the ZEPHYR code, the continuous spectrum  $P_S(\omega)$  is modeled as a series of discrete frequency bins, each of which is treated independently as described in § 4.1. We define the bins as “octaves” in frequency space; i.e., the first bin encompasses  $\omega_{ac}$  to  $2\omega_{ac}$ , the second encompasses  $2\omega_{ac}$  to  $4\omega_{ac}$ , and so on. Ideally, it would have been preferable to use even narrower bins in order to more accurately represent the shape of the spectrum. However, if the frequency bins were too narrow, each would contain a vanishingly small amount of wave energy. The calculation of nonlinear steepening (eq. [36]) depends on the total amplitude that remains reasonably coherent at a given frequency. Narrow bins—treated independently as described above—would essentially destroy this coherence and produce an unphysical delay in the onset of steepening due to the low amplitudes in each bin. The use of octaves is an attempt to balance the needs of frequency resolution and realistic coherence for steepening.<sup>5</sup>

<sup>5</sup> Too much coherence would also be undesirable. One-dimensional simulations of chromospheric shocks often result in “shock cannibalization” (i.e., overtaking and merging) and an effective filtering out of high frequencies. A realistic multidimensional distribution of strong and weak acoustic sources at and below the photosphere, though, is more likely to result in an incoherent and randomized power spectrum such as we assume here (see, e.g., Cadavid et al. 2003; Ulmschneider et al. 2005).

In the models computed for this paper, a series of 14 bins is used. The power missed by ignoring frequencies above the maximum value of  $2^{14}\omega_{ac}$  is only  $\sim 10^{-5}$  of the total flux. The monochromatic frequencies used in the wave action conservation equation are computed as mean, or first-moment frequencies over the power spectrum of each bin. The first one ( $\omega_{ac}$  to  $2\omega_{ac}$ ), for example, has a mean of  $1.62\omega_{ac}$  (i.e.,  $f = 7.7$  mHz).

### 5. ALFVÉN WAVES AND TURBULENCE

We model transverse MHD fluctuations in the radially oriented magnetic flux tube as ideal incompressible Alfvén waves. The equations and assumptions we use generally follow Cranmer & van Ballegoijen (2005), who computed various properties of Alfvén waves from the photosphere to the interplanetary medium assuming a known background plasma state ( $u$ ,  $\rho$ ,  $B_0$ ). Here we compute the wave properties and background plasma properties together in a self-consistent manner. The Alfvén waves are believed to arise from transverse jostling of magnetic flux tubes in the intergranular photosphere by convective motions on granular ( $\sim 1000$  km) horizontal scales. Note that, similar to the acoustic waves, the Alfvén waves are expected to have modified dispersive properties in the photosphere and low chromosphere (e.g., they become *kink-mode* tube waves in regions where the flux tubes are surrounded by field-free regions; see Spruit 1981, 1982), but we ignore these effects because they occur over a small range of heights. Our treatment of Alfvén wave reflection and turbulent dissipation is complementary to the recent work of Verdini et al. (2005, 2006).

As in the previous section, we first discuss the overall wave energy transport and dissipation mechanisms (§ 5.1) and then describe the power spectrum of the fluctuations (§ 5.2). The way that the frequency dependence is assimilated into the model is slightly different from the acoustic-wave case, though.

#### 5.1. Alfvén Wave Action Conservation

For transverse incompressible waves, we solve a single wave action conservation equation with a damping term that contains information about the power spectrum and wave reflection. We believe that a monochromatic treatment of the wave action conservation (i.e., to treat each frequency bin independently from the rest) is inappropriate to use when the dominant dissipation mechanism is MHD turbulence. A turbulent cascade inherently contains strong nonlocal “mixing” in frequency and wavenumber space. Thus the turbulent damping rate is computed only using quantities that have been integrated over the power spectrum (see below).

We assume the Alfvén waves are dispersionless with a phase speed given by  $\omega/k_{\parallel} = u + V_A$  in the stationary reference frame of the Sun. The Alfvén speed is defined as  $V_A = B_0/(4\pi\rho)^{1/2}$ . Although we solve the full non-WKB transport equation to obtain the *relative* distribution of outward and inward propagating waves, we use the following simplified version of the wave action conservation equation to compute the radial evolution of the total (frequency-integrated) wave energy density  $U_A$ :

$$\frac{\partial}{\partial t} \left( \frac{U_A}{\omega'} \right) + \frac{1}{A} \frac{\partial}{\partial r} \left[ \frac{(u + V_A)AU_A}{\omega'} \right] = -\frac{Q_A}{\omega'} \quad (43)$$

(see, e.g., Jacques 1977; Isenberg & Hollweg 1982; Tu & Marsch 1995). The presence of the Doppler shifted frequency

$\omega'$  (measured in the solar wind frame) in the above equation is deceptive, since the wave action conservation is essentially *frequency-independent*. Note that  $\omega' = \omega - uk_{\parallel} = \omega V_A/(u + V_A)$ , and thus a constant factor of  $\omega$  can be factored out of each term in equation (43). The total Alfvénic energy density  $U_A$  is the sum of the energy densities in kinetic and magnetic fluctuations,

$$U_K = \frac{\rho v_{\perp}^2}{2}, \quad U_B = \frac{B_{\perp}^2}{8\pi} \quad (44)$$

where  $v_{\perp}$  and  $B_{\perp}$  are the transverse velocity and magnetic field oscillation amplitudes. We assume equipartition between the two components ( $U_K = U_B$ ), such that  $U_A = 2U_K = \rho v_{\perp}^2$ .

The use of equation (43) contains the assumption that the energy balance is dominated by outward-propagating waves, whose energy density  $U_{-}$  exceeds the energy density of inward-propagating waves  $U_{+}$ . By definition,  $U_A = U_{-} + U_{+}$ , and

$$U_{\pm} = \frac{\rho Z_{\pm}^2}{4} \quad (45)$$

where the Elsasser (1950) amplitudes are defined here as  $Z_{\pm} \equiv |v_{\perp} \pm B_{\perp}|/(4\pi\rho)^{1/2}$ . For future reference, we give the expression for the net outward Alfvén wave flux,

$$F_A = u(U_K + 2U_B) + V_A(U_{-} - U_{+}) \quad (46)$$

(e.g., Heinemann & Olbert 1980). The two assumptions of kinetic/magnetic equipartition and outward-wave dominance in equation (43) tend to break down in the lower atmosphere when there is strong non-WKB wave reflection, but in the *corona*—where the dominant Alfvénic heating occurs—these assumptions seem to be appropriate (see also Cranmer & van Ballegoijen 2005).

The only physical source of Alfvén wave damping that we include is the turbulent cascade, which ultimately must terminate in an irreversible conversion of wave energy into heat. This is, in some sense, a controlled experiment to evaluate to what degree turbulence may be the *dominant* cause of coronal heating and solar wind acceleration, but other damping mechanisms for Alfvén waves have been suggested. Collisional damping mechanisms for MHD waves have been studied extensively in the context of the dense coronal base (e.g., Alfvén 1947; Kuperus et al. 1981; Narain & Ulmschneider 1990, 1996; Porter et al. 1994; Roberts 2000), but the open field lines that feed the solar wind have lower densities and are thus less collisionally dominated than closed loops in the low corona. Cranmer & van Ballegoijen (2005) investigated linear viscous dissipation of Alfvén waves along an open magnetic flux tube and found that viscosity should be negligible for waves having periods longer than about 1 minute.

We adopted the following phenomenological form for the MHD turbulence damping rate,

$$Q_A = \rho \mathcal{E}_{\text{turb}} \frac{Z_{-}^2 Z_{+} + Z_{+}^2 Z_{-}}{4L_{\perp}} \quad (47)$$

(Hossain et al. 1995; Zhou & Matthaeus 1990; Matthaeus et al. 1999; Dmitruk et al. 2001, 2002). The transverse length scale  $L_{\perp}(r)$  represents an effective perpendicular correlation length of the turbulence for the largest “driving” eddies. We used the standard assumption that  $L_{\perp}$  scales with the transverse width of the open flux tube; i.e., that it remains proportional to  $B_0^{-1/2}$  (see also Hollweg 1986). Ideally, the evolution of  $L_{\perp}$  should be coupled to the radial variation of the fluctuation energy (see, e.g., eq. [3] of Matthaeus et al. 1999) as

well as to the non-varying field strength. Future work should include both this effect and additional tests of whether the above phenomenological form is an adequate representation of the true anisotropic cascade.

The normalization of  $L_\perp$  is one of the few free parameters of our model. We note that Cranmer & van Ballegooijen (2005) found that  $L_\perp$  should be about 1100 km at the height in the low chromosphere where thin flux tubes merge with one another. Mapping this value down to the photosphere would yield a lower boundary value  $L_{\perp\odot} = 320$  km. This spatial scale is intermediate between the probable horizontal size an individual flux tube in the photosphere (50–100 km) and the size of a convective granule (1000 km). This value is also similar to the width of an intergranular lane and also the mean separation between photospheric flux tubes in the quiet-Sun supergranular network (350–700 km; see Cranmer & van Ballegooijen 2005).

The factor  $\mathcal{E}_{\text{turb}}$  in equation (47) is a turbulent efficiency that accounts for regions where the turbulence may not have time to develop before the waves or the wind carry away the energy (see Dmitruk & Matthaeus 2003). We estimated this efficiency factor to be

$$\mathcal{E}_{\text{turb}} = \frac{1}{1 + (t_{\text{eddy}}/t_{\text{ref}})^n} \quad (48)$$

where the two time scales in this expression are  $t_{\text{eddy}}$ , a nonlinear outer-scale eddy cascade time, and  $t_{\text{ref}}$ , a timescale for macroscopic Alfvén wave reflection. In most of the models presented below we take  $n = 1$ , based on analytic and numerical models of Dobrowolny et al. (1980), Matthaeus & Zhou (1989), and Oughton et al. (2006). Dmitruk & Matthaeus (2003) found that the turbulent cascade has sufficient time to develop and heat the plasma only when  $t_{\text{eddy}} \ll t_{\text{ref}}$ . Thus, our efficiency factor above quenches the turbulent heating when  $t_{\text{eddy}} \gg t_{\text{ref}}$ , i.e., when the Alfvén waves want to propagate away much faster than the cascade can proceed “locally.” The reflection time is defined simply as  $t_{\text{ref}} = 1/|\nabla \cdot \mathbf{V}_A|$ , and the eddy cascade time is given by

$$t_{\text{eddy}} = \frac{L_\perp \sqrt{3\pi}}{(1 + M_A) v_\perp}, \quad (49)$$

where the Alfvénic Mach number  $M_A = u/V_A$  and the numerical factor of  $\sqrt{3\pi}$  comes from the normalization of an assumed shape of the turbulence spectrum (see Appendix C of Cranmer & van Ballegooijen 2005; see also Higdon 1984; Shebalin et al. 1983; Goldreich & Sridhar 1995, 1997; Bhattacharjee & Ng 2001; Cho et al. 2002). When  $n = 1$ , the efficiency factor provides an approximate bridging between a Kolmogorov (1941) scaling, when  $t_{\text{eddy}} \ll t_{\text{ref}}$ , and an IK-like (Iroshnikov 1963; Kraichnan 1965) scaling, when  $t_{\text{eddy}} \gg t_{\text{ref}}$ . There is still some controversy, though, over which type of cascade rate is appropriate for MHD turbulence in the solar wind.

We separated the Alfvén wave energy into outward ( $Z_-$ ) and inward ( $Z_+$ ) components by solving a modified form of the non-WKB transport equations of Heinemann & Olbert (1980), Barkhudarov (1991), Velli (1993), and Orlando et al. (1996).<sup>6</sup> These frequency-dependent equations are dis-

cussed below in § 5.2 and their solution provides a spectrum-averaged value of the effective local reflection coefficient  $\mathcal{R} = Z_+/Z_-$ . Knowing  $\mathcal{R}$  and  $U_A$  (from eq. [43]) allows the Elsasser amplitudes to be computed at all heights,

$$Z_- = \sqrt{\frac{4U_A}{\rho(1 + \mathcal{R}^2)}}, \quad Z_+ = \mathcal{R}|Z_-|, \quad (50)$$

and the turbulent damping rate in equation (47) is then specified.

### 5.2. Alfvén Wave Frequency Dependence

For a series of Alfvén wave frequencies  $\omega$ , we solved the non-WKB wave transport equations in the dimensionless form given by equations (24) and (33) of Barkhudarov (1991),

$$\frac{d\Psi}{dr} = \frac{(\Psi^2 - 1)\cos\Gamma}{2H_A} \quad (51)$$

$$\frac{d\Gamma}{dr} = \frac{(\Psi^2 + 1)\sin\Gamma}{2H_A\Psi} - \frac{2\omega V_A}{u^2 - V_A^2} \quad (52)$$

where  $\Psi$  is related to the frequency-dependent reflection coefficient  $\mathcal{R}_\omega$  via

$$\Psi = \left( \frac{u - V_A}{u + V_A} \right) \mathcal{R}_\omega, \quad (53)$$

$\Gamma$  is the angular phase shift between the  $Z_-$  and  $Z_+$  wave trains, and  $H_A$  is the (signed) scale height for the Alfvén speed, or  $V_A/(\partial V_A/\partial r)$ . Although the models of Barkhudarov (1991) were limited to spherical geometry ( $A \propto r^2$ ) the above relations are valid for any  $A(r)$  (see also Cranmer & van Ballegooijen 2005). We followed the general solution procedure outlined by Barkhudarov (1991) for integrating across the Alfvénic singular point  $r_A$ , where  $u = V_A$  and thus  $\Psi = 0$ . The reflection coefficient remains finite at this point, and it can be written exactly as

$$\mathcal{R}_\omega(r_A) = \frac{|V'_A|}{\sqrt{\omega^2 + (u' - V'_A)^2}}, \quad (54)$$

where  $u'$  and  $V'_A$  are radial derivatives of the outflow speed and Alfvén speed taken at  $r = r_A$ . The ZEPHYR code utilizes fourth-order Runge-Kutta numerical integration to solve for  $\mathcal{R}_\omega(r)$  above and below  $r_A$ . We ensured that  $|\mathcal{R}_\omega| < 1$  at all heights and for all frequencies.

The dissipation of Alfvén waves is explicitly not included in the equations given above for the reflection coefficient. Although it is possible to include nonlinear damping consistent with equation (47) in these transport equations (see, e.g., Verdini et al. 2005, 2006), we remain cautious about the combination of strong turbulent damping and “monochromatic” wave quantities. Additional simulations may be required in order to better guide the use of phenomenological nonlinear terms when following the development of a spectrum of Alfvénic fluctuations.

The full frequency-averaged reflection coefficient is computed by weighting  $\mathcal{R}_\omega$  by the Alfvén wave power spectrum  $P_A(\omega)$ , with

$$\mathcal{R}^2(r) = \frac{\int d\omega P_A(\omega) \mathcal{R}_\omega^2(r)}{\int d\omega P_A(\omega)} \quad (55)$$

where the square of  $\mathcal{R}$  is used because the power spectrum is an energy density quantity and  $\mathcal{R}$  is a ratio of amplitudes. The spectrum is used essentially as a weighting function, and

<sup>6</sup> By WKB (Wentzel, Kramers, Brillouin) we do not refer to any specific asymptotic expansion. The WKB limit of pure outward propagation, with no reflection, is amenable to the standard “eikonal” approximation by defining a local wavenumber. The treatment of non-WKB reflection is more general in that the radial parts of the  $Z_\pm$  eigenfunctions are computed numerically without the use of a wavenumber.

we assume it has a constant shape as a function of height (see, e.g., Figure 8 of Cranmer & van Ballegoijen 2005).

Figure 3 shows the shape of the Alfvén wave power spectrum that we use in the ZEPHYR models discussed below. Specifically, this is the power spectrum of total (kinetic plus magnetic) energy from the model of Cranmer & van Ballegoijen (2005) taken at the height of the transition region. It was computed from an empirically constrained *photospheric* spectrum of the dynamics of thin flux-tubes, which is described as a linear superposition of two types of motion. First, isolated flux tubes undertake “random walks” in response to convective granulation; they have a power spectrum that has been constrained by observed G-band bright point motions (e.g., van Ballegoijen et al. 1998; Nisenson et al. 2003). Second, flux tubes exhibit sporadic rapid horizontal “jumps” that probably represent merging, fragmenting, or reconnecting with surrounding magnetic fields (e.g., Choudhuri et al. 1993; Berger & Title 1996; Berger et al. 1998; Hasan et al. 2000) which we modeled as a series of periodic impulsive motions. High-resolution photospheric observations thus provided the kinetic energy spectrum, and the partitioning between kinetic and magnetic energy components (needed to compute the total energy spectrum) was determined using the analytic linear theory of kink-mode waves in a stratified atmosphere. Finally, propagation effects between the photosphere and the transition region ( $z = 0.003 R_\odot$  in the model of Cranmer & van Ballegoijen 2005) were taken into account by solving the combined non-WKB kink-mode and Alfvén-mode transport equations for an empirically constrained (FAL-C') background plasma state.

There are several noteworthy features of the spectrum  $P_A(\omega)$  in Figure 3. There is power at the lowest frequencies, corresponding to periods of hours to days, because of the assumed random-walk component of the photospheric flux tube motion (with  $P_A \propto e^{-\omega\tau}$ , where  $\tau \approx 60$  s). However, the relative amount of power at periods longer than 1 hour is negligible compared to the total; this stands in contrast with in situ measurements that show the majority of power to be at these long periods (e.g., Goldstein et al. 1995; Tu & Marsch 1995). There is growing evidence that the low-frequency fluctuations seen in interplanetary space may be the result of the passage of multiple uncorrelated flux tubes past the spacecraft and not intrinsic turbulence within any one flux tube (see, e.g., McCracken & Ness 1966; Jokipii & Parker 1969; Bruno et al. 2001; Giacalone & Jokipii 2004; Giacalone et al. 2006; Borovsky 2006).

The damping of evanescent kink-mode waves can be seen in Figure 3 from the mild discontinuity at the cutoff frequency of 1.4 mHz. Only about 40% of the energy of evanescent waves is lost, though, because the flux tubes remain thin (and thus gravitationally buoyant) only below a low-chromosphere “merging height” of 600 km. Above this height the magnetic fields expand horizontally to fill the volume above supergranular network lanes and the transverse waves both below and above the cutoff can propagate freely as Alfvén waves. The multiple peaks in the spectrum between about 3 and 20 mHz are a result of propagation effects between the photosphere and the merging height. In the model of Cranmer & van Ballegoijen (2005) the atmosphere was modeled with the non-isothermal FAL-C' temperature structure and a radially varying filling factor for the flux tubes; both of these factors resulted in a complicated frequency dependence for the non-WKB transmission of kink-mode waves between  $z = 0$  and 600 km. Coincidentally, the frequencies of the maxima in

both  $P_A$  and  $P_S$  are each about a factor three higher than their respective cutoff frequencies.

It is important to note that the Alfvén wave amplitude  $v_\perp$  (obtained from the WKB-like eq. [43]) diverges from the actual transverse velocity of oscillating magnetic flux tubes in the lower atmosphere. The effects of evanescence and non-WKB wave reflection are not *directly* included in equation (43), but they end up being of minimal importance in the corona and solar wind. We thus can estimate the true velocity amplitude  $w_\perp$  after the final iterated solar atmosphere parameters have been determined, as

$$w_\perp^2 = v_\perp^2 \left( \frac{1 + \mathcal{R}_\omega^2}{1 - \mathcal{R}_\omega^2} \right) \times \begin{cases} 1, & \omega \geq \omega_{kc} \\ \exp \left[ 1 - \sqrt{1 - (\omega/\omega_{kc})^2} \right], & \omega < \omega_{kc} \end{cases}, \quad (56)$$

where  $\omega_{kc}$  is the kink-mode cutoff frequency. Above the mid-chromosphere height where thin flux tubes merge with one another,  $\omega_{kc}$  effectively goes to zero and there is no evanescence. The  $\mathcal{R}_\omega$  factor above in parentheses corrects for the approximation that equation (43) follows only outward-going waves. For the ZEPHYR models presented below, the spectrum-averaged value of  $w_\perp$  at the photosphere is typically a factor of 2 to 5 times larger than  $v_\perp$  at this lower boundary. Above the transition region, though,  $w_\perp \approx v_\perp$  (see also Figure 11 of Cranmer & van Ballegoijen 2005). Despite the fact that  $v_\perp$  underestimates the actual velocity amplitude, we believe it is more appropriate to use this as an imposed lower boundary condition rather than to use  $w_\perp$ . The latter quantity depends on quantities that are computed self-consistently along with the other plasma parameters and are not known a priori.

## 6. WAVE PRESSURE ACCELERATION

Just as electromagnetic waves carry momentum and exert pressure on matter, propagating acoustic and MHD waves can also do work on the mean fluid via a similar kind of radiation stress. (Bretherton & Garrett 1968; Dewar 1970; Belcher 1971; Alazraki and Couturier 1971). For parallel-propagating acoustic and Alfvén waves, the time-averaged radial wave pressure acceleration was derived in detail by Jacques (1977) to be

$$D = -\frac{1}{2\rho} \frac{\partial U_A}{\partial r} - \left( \frac{\gamma+1}{2\rho} \right) \frac{\partial U_S}{\partial r} - \frac{U_S}{A\rho} \frac{\partial A}{\partial r}. \quad (57)$$

As above, we ignore departures from kinetic-magnetic energy equipartition for the Alfvén waves; this ends up being a good approximation for solar wind conditions (see, e.g., Heinemann & Olbert 1980; Cranmer & van Ballegoijen 2005).

To implement the above expression in the ZEPHYR code, we used the wave action conservation equations (23) and (43) to reformulate the momentum conservation equation into a time-independent Parker (1958, 1963) critical point equation with additional terms that affect the definition of the critical point. Assuming  $\gamma = 5/3$  throughout, the modified momentum equation becomes

$$\left( u - \frac{u_c^2}{u} \right) \frac{du}{dr} = -\frac{GM_*}{r^2} + (u_c^2 + V_1^2) \frac{d \ln A}{dr} - (a^2 + V_2^2) \frac{d \ln a^2}{dr} + \frac{1}{\rho} \left[ \frac{Q_A}{2(u+V_A)} + \frac{4Q_S}{3(u+c_s)} \right] \quad (58)$$

where  $a$  is the isothermal sound speed  $(k_B T / m_H)^{1/2}$  and the modified critical speed is given by

$$u_c^2 = a^2 + \frac{U_A}{4\rho} \left( \frac{1+3M_A}{1+M_A} \right) + \frac{8U_S}{3\rho} \left( \frac{M_S}{1+M_S} \right) \quad (59)$$

with the bulk-flow Mach numbers  $M_A = u/V_A$  and  $M_S = u/c_s$ . In the presence of acoustic waves, the additional terms above are given by

$$V_1^2 = \frac{U_S}{3\rho} \left( \frac{1-7M_S}{1+M_S} \right) \quad (60)$$

$$V_2^2 = \frac{4U_S}{3\rho} \left( \frac{M_S-1}{M_S+1} \right). \quad (61)$$

The modified critical radius  $r_c$  is found by locating the point where the right-hand side of equation (58) is zero, and thus  $u = u_c$ .

For rapidly expanding superradial flux tubes, Kopp & Holzer (1976) pointed out that there may be more than one possible location for the critical point. Defining the right-hand side of equation (58) as the radial derivative of a known function  $\mathcal{F}(r)$ , they essentially found that the *global minimum* of  $\mathcal{F}(r)$  specifies the critical point location that allows for a stable and continuous solution for  $u(r)$  from the Sun to interplanetary space (see also Vázquez et al. 2003; Cranmer 2005a). The Kopp & Holzer (1976) result, though, was derived for an ideally polytropic corona without wave pressure acceleration. It is not clear if this global minimum condition is applicable to the models described in this paper. For all of the ZEPHYR models discussed below in § 8, though, the global minimum of  $\mathcal{F}(r)$  coincides with the *largest* possible value of  $r_c$ . For expediency, then, when there are multiple possibilities we choose the largest value for the critical radius that also exhibits a minimum in  $\mathcal{F}$  (i.e.,  $d^2\mathcal{F}/dr^2 > 0$ ).

Note that equation (58) includes the wave pressure acceleration, but not the explicit derivatives of  $U_S$  and  $U_A$  that appear in equation (57). The modified momentum equation thus alleviates the need to perform noisy numerical differentiation (see also Jacques 1977; Hartmann & MacGregor 1980; DeCampi 1981; Holzer et al. 1983; Wang & Sheeley 1991). The damping rates  $Q_S$  and  $Q_A$  appear explicitly in the momentum equation, which provides additional nonlinear coupling between the momentum and energy equations.

Wave pressure acceleration has been invoked by Laming (2004) as a potential explanation for the relative enhancement of low FIP (first ionization potential) elements relative to high FIP elements in the corona and solar wind.<sup>7</sup> If Alfvén waves exert an appreciable force on ions in the chromosphere and transition region (where there are still neutrals that do not feel this force) significant “fractionation” may occur. We apply Laming’s (2004) idea to the models presented below by evaluating his integrated momentum equation for atoms and ions of element  $s$  undergoing fractionation. A slightly simplified version of this equation (which assumes that there is no explicit dependence of  $D$  on the density gradient) is

$$\ln \left( \frac{(\rho_s v_s^2)_u}{(\rho_s v_s^2)_l} \right) = \int_{z_l}^{z_u} dz \frac{D}{v_s^2} \left[ \frac{2\xi_s}{\xi_s + (1-\xi_s)(\nu_{s,i}/\nu_{s,n})} \right] \quad (62)$$

where  $\rho_s$  and  $v_s = (c_s^2 + v_{\parallel}^2)^{1/2}$  are the element’s mass density and effective parallel turbulent speed. The ionization fraction of the element—essentially one minus the neutral fraction—is given by  $\xi_s$ , and the collision rates between ions and neutrals of element  $s$  and the ambient gas are given by  $\nu_{s,i}$  and  $\nu_{s,n}$  (see Laming 2004 for detailed expressions). Subscripts  $l$  and  $u$  denote quantities computed at heights  $z_l$  (a lower boundary we

take as the photosphere) and  $z_u$  (an upper boundary that can be anywhere in the corona or solar wind), respectively. The degree of FIP enhancement between these heights is obtained by solving equation (62) twice: once for the ratio  $\rho_{s,u}/\rho_{s,l}$  for a low FIP element, and once for a high FIP element. Dividing one ratio by the other cancels out the overall density stratification between  $z_l$  and  $z_u$  and leaves only the fractionated abundance difference.

## 7. SOLUTION METHOD

We compute time-independent solutions to the conservation equations given above by applying a new hybrid method of iteration and relaxation. Reasons for not following time-dependent fluctuations explicitly were summarized in § 2. It has become common, though, to use time-dependent hydrodynamics codes to find stable time-steady solar wind solutions (see recent work by, e.g., Li et al. 2004; Lionello et al. 2005; Lie-Svendsen & Esser 2005, and references therein). We break from this tradition for several reasons. First, in the one-fluid case, the time-independent mass and momentum conservation equations are relatively easy to solve, and only the energy equation requires special treatment. Second, when modeling the photosphere, chromosphere, corona, and wind all in one grid, the energy equation changes its basic character at different locations depending on which terms are dominant. In the corona, the Spitzer-Härm conduction makes it a second-order parabolic differential equation. In the outer solar wind the gradual transition to collisionless heat conduction reduces it to a first-order differential equation. In the photosphere and chromosphere it is essentially a zeroth-order differential equation—i.e., an algebraic balance between heating and cooling. These changes, combined with the huge dynamic range in quantities such as density, temperature, and wave phase speeds, make it difficult to implement and optimize a *robust* time-dependent numerical scheme. Even implicit methods, which are not necessarily limited by propagation across the smallest grid zones, appear to be prohibitively difficult to set up properly when the source terms (i.e., the waves) have such a complex nonlinear dependence on the primary plasma parameters.

The code developed for this work is called ZEPHYR. After setting up an initial trial guess for the plasma parameters  $\rho$ ,  $u$ , and  $T$ , the code iterates a fixed number of times (typically 100 to 200) alternately between solutions of the energy equation (eq. [3]) and the other constitutive and conservation equations (eqs. [1], [2], [4], [5], [6], [23], [43], [51], [52]) to find a steady-state accelerating wind solution. To stabilize the iteration process and avoid pathological solutions, most of the plasma parameters are “undercorrected” using a scheme described below—i.e., rather than replacing the old solution with the new one, a fractional step *toward* the new solution is taken.

The spatial grid used by ZEPHYR has variable zone spacing that depends on the height above the lower boundary. The total number of grid zones  $N$  is divided into two subsets: 45% of the zones are allocated to a fine mesh with constant spacing in the lower atmosphere (i.e., between  $z = 0$  and a fixed zone-midpoint height  $z_{\text{mid}} = 0.005 R_{\odot}$ ) and 55% of the zones occupy the rest of the grid with spacing that increases by 1% per zone from the value at  $z_{\text{mid}}$  up to the top of the grid. All models described in this paper have  $N = 1300$  and a fixed grid spacing of  $8.56 \times 10^{-6} R_{\odot} \approx 6$  km in the lower atmosphere. At the top of the grid ( $z = 1200 R_{\odot} \approx 5.6$  AU) the grid spacing has increased to  $24 R_{\odot}$ . The relative spacing  $\Delta r/R_{\odot}$  thus

<sup>7</sup> For other potential explanations of the FIP effect, see also von Steiger & Geiss (1989), Vauclair (1996), Arge & Mullan (1998), Schwadron et al. (1999), and references therein and in Laming (2004).

increases from about  $10^{-5}$  in the lower atmosphere up to 0.02 at the top of the grid.

The initial condition for the temperature is a gray radiative equilibrium atmosphere (i.e.,  $T = T_{\text{rad}}$  as defined in § 3.2) that is perturbed by transitioning (using a hyperbolic tangent function) to a corona/wind value above a specified transition region height of  $0.9z_{\text{mid}}$ . The temperature above this transition obeys a power law in  $r$ , with a basal value of  $1.5 \times 10^6$  K and a very slow radial decline proportional to  $r^{-0.05}$ . The lower boundary ( $z = 0$ ) is defined as  $\tau_R = 2$ , which corresponds to a base density  $\rho_{\odot} = 2.45 \times 10^{-7}$  g cm $^{-3}$ . This choice for the lower boundary condition is used in order to include the traditional photosphere (either  $\tau_R = 1$  or  $2/3$ ) in the interior of the grid. The temperature at the lower boundary is defined by the gray atmosphere condition (eq. [10]). The initial density distribution is assumed to be hydrostatic (i.e.,  $u = 0$ ). Refined initial guesses for the density and outflow speed are evaluated as the first steps in the iteration process described below. Tests have shown that finding the proper solution is insensitive to the details of the initial guess, but the iteration method converges faster when the initial guess has properties closer to a realistic solar atmosphere.

The main “outer” iteration loop consists of two interior modules, each of which undergoes a number of “inner” iterations. The first module solves for the dynamics ( $\rho$ ,  $u$ ) and for the various source terms in the momentum and energy equations. The five steps taken in one inner iteration of this module are as follows.

1. The hydrogen ionization fraction  $x$ , the gas pressure  $P$ , and the internal energy density  $E$  are computed as described in § 3.1. The optical depth scale  $\tau_R$  is integrated and the radiative cooling/heating rate  $Q_{\text{rad}}$  is computed (§ 3.2). The heat conduction rate  $Q_{\text{cond}}$  (§ 3.3) is also determined using the four-point finite differencing scheme discussed below for the radial derivatives  $\partial T / \partial r$  and  $\partial q_{\parallel} / \partial r$ . The heat conduction  $Q_{\text{cond}}$  is artificially suppressed in the outermost 10 grid zones in order to produce a more well-behaved upper boundary condition that is dominated by the outward advection of all characteristics. (These 10 zones are not considered to be part of the actual solar wind solution.)
2. The modified Parker critical point equation (58) is solved for  $u(r)$  by integrating up and down from  $r_c$ . To step from the critical point (which generally falls between grid zones) to the grid zones immediately above and below, an analytic derivative  $(\partial u / \partial r)_c$  computed from L’Hôpital’s rule is used in order to avoid the well-known instability at an X-type singular point. At all other grid zones, fourth-order Runge-Kutta integration is used (e.g., Press et al. 1992). The undercorrection scheme described below is used for  $u(r)$ .
3. The time-steady mass conservation equation (1) is solved for  $\rho(r)$  in a straightforward way. The base density  $\rho_{\odot}$  described above is kept fixed and the prior step’s solution for the basal outflow speed  $u_{\odot} = u(R_{\odot})$  is used to determine the constant mass flux  $\rho u A$ . The density is then computed exactly at each grid zone, but the undercorrection scheme is also used for  $\rho(r)$  in order to prevent too rapid a change.
4. The properties of the acoustic wave spectrum are computed at each grid point and the spectrum-integrated

values of  $U_S$  and  $Q_S$  are determined (§ 4). The steepening of each monochromatic wave train is computed by integrating equation (36) up from the lower boundary simultaneously with the wave action equation (23). Simple first-order Euler steps are used to perform both integrations.

5. The non-WKB Alfvén wave transport equations (§ 5.2) are solved for a number of frequency dependent reflection coefficients  $\mathcal{R}_{\omega}(r)$  which are summed over the power spectrum to obtain  $\mathcal{R}(r)$ . The adaptive fourth-order Runge-Kutta scheme developed by Cranmer & van Ballegoijen (2005) has been included in the ZEPHYR code. Once the  $Z_{\pm}$  Elsasser variables have been determined, the heating rate  $Q_A$  is computed and the Alfvén wave action conservation equation is integrated up from the lower boundary to obtain  $U_A$  (§ 5.1).

These steps are repeated for a fixed number of inner iterations (typically 50 to 100) in order to reach internal consistency. However, because the non-WKB wave reflection equations (51–52) dominate the computation time, the reflection coefficient  $\mathcal{R}$  is recomputed only for the first two of these iterations.

The second main module of ZEPHYR solves the energy conservation equation and obtains a time-independent temperature distribution  $T(r)$ . There are three main steps that are repeated until either a certain degree of convergence has been attained ( $\langle \delta E \rangle < 10^{-3}$ ) or a maximum number of iterations (typically 1000) is exceeded. The convergence quantity  $\langle \delta E \rangle$  is defined to be an average over the relative convergence at each grid zone. For the radial grid with  $N$  discrete zones,

$$\langle \delta E \rangle \equiv \frac{1}{N} \sum_{i=1}^N \left( \frac{|\dot{E}|_i}{\max |Q|_i} \right) \quad (63)$$

where  $i$  denotes quantities computed at each grid zone. The numerator is obtained by solving equation (3) for the explicit time dependent term  $\dot{E} \equiv \partial E / \partial t$  at each grid zone and taking the absolute magnitude. This residual-like quantity is nonzero for solutions that have not yet converged to a steady state. The denominator is the absolute magnitude of the largest single term in equation (3); this includes the two advection terms on the left-hand side, and it also includes the separation of the optically thick  $J$  and  $S$  terms in  $Q_{\text{thick}}$  (eq. [9]) which balance one another in the photosphere. The solution that satisfies exact time-independence (for the energy equation) would have  $\langle \delta E \rangle = 0$ . The following three steps repeated by the second module of ZEPHYR are designed to hone in on this solution.

1. The core procedure in solving the energy equation is *relaxation* using  $\dot{E}$  at each grid zone. The sign of  $\dot{E}$  is used to determine whether the current solution for  $T$  should be increased or decreased, and the magnitude of the change is computed from a positive-definite correction factor  $c(r)$ .<sup>8</sup> This factor is initialized to a constant value of 0.16 at the start of the inner iteration loop. During each relaxation step it is either kept constant, if  $\dot{E}$  has kept the same sign from the last step to the current step, or it is reduced in magnitude by 7%, if  $\dot{E}$  has switched signs from the last step to the current step. The reduction in  $c$  that occurs when  $\dot{E}$  oscillates in sign is

<sup>8</sup> The fact that the magnitude of  $\dot{E}$  is *not* used is the main reason that this technique is called “relaxation” and is not really a variety of time-dependent hydrodynamic evolution.

a kind of “annealing” that allows the relaxation method to focus in on the time-independent solution (i.e., the solution with  $\dot{E} = 0$  everywhere). The updated temperature at each grid zone is thus determined by multiplying the old value by a factor of  $(1 + c\dot{E}/|\dot{E}|)$ . The optimized numerical values given above were determined from a large number of tests with a range of values.

2. Because the relaxation method above can lead to discontinuous jumps in  $T(r)$ , we perform trial piecewise smoothing in order to reduce unphysical fluctuations. The radial grid with  $N = 1300$  is broken up into 130 pieces each having 10 zones. (At the start of each iteration, the offset point that defines the start of the first 10-zone piece is shifted by one grid zone.) If a piece contains more than one change of sign in the slope  $\partial T / \partial r$ , it is smoothed using a Gaussian filter (with a two zone half-width) until only 0 or 1 changes of sign remain. The piecewise nature of this smoothing is necessary so that the entire grid does not “suffer” when just a small part of it contains numerical noise.
3. The convergence parameter  $\langle \delta E \rangle$  for the current inner iteration is compared to the best solution (i.e., the lowest value of  $\langle \delta E \rangle$ ) that has been found during this outer iteration loop. If the solution has improved, the best solution is updated. If the solution has gotten worse, we discard it and revert to the saved best case. Note, though, that this comparison is not performed at every inner iteration step. (Doing it every time could lead to an infinite loop with no changes ever made to  $T$ .) Tests showed that it is best to allow the solutions to evolve for a while and only perform this comparison every 15 to 20 iteration steps (we use 17).

The converged value of  $T$  that emerges from this module is undercorrected before starting the next outer iteration.

The undercorrection scheme that is used at various points in the ZEPHYR code was motivated by globally convergent backtracking methods for finding roots of nonlinear equations (e.g., Dennis & Schnabel 1983). Rather than taking the full suggested iteration step, which may propel the solution away from the desired region of convergence, it is sometimes best to take only a partial step. For a scalar quantity  $f_{i,j}$  at radial grid zone  $i$  and iteration step  $j$ , we specify this partial step as

$$f_{i,j+1} = f_{i,j} \left| \frac{\tilde{f}_{i,j+1}}{f_{i,j}} \right|^\epsilon \quad (64)$$

where  $\tilde{f}_{i,j+1}$  is the next suggested iteration that was obtained by solving one of the conservation equations. The exponent  $\epsilon$  describes the degree of undercorrection. When the solutions are nearly converged, the full iteration step should be taken ( $\epsilon \approx 1$ ). When the solutions are far from convergence, though, we require substantial undercorrection ( $0 < \epsilon \ll 1$ ). To obtain this exponent, we use

$$\epsilon = \epsilon_0 + (1 - \epsilon_0) \min \left( \left| \frac{\tilde{f}_{j+1}}{f_j} \right|, \left| \frac{f_j}{\tilde{f}_{j+1}} \right| \right) \quad (65)$$

where the minimum is taken over the entire radial grid (thus the absence of  $i$  subscripts) so that the worst agreement between the current iteration and the next suggested iteration is highlighted. Because  $\tilde{f}_{j+1}$  may be larger or smaller than  $f_j$ , both the ratio and its reciprocal are used above, and the

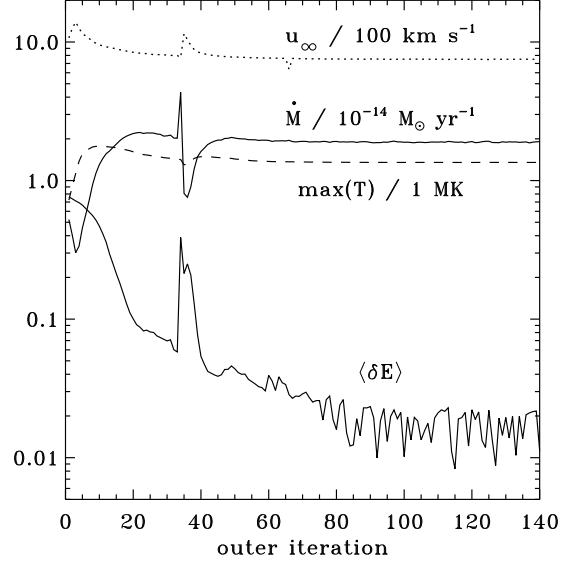


FIG. 4.— Convergence of the ZEPHYR outer iteration process toward a steady-state solution. From top to bottom, the plasma parameters shown include the solar wind speed  $u_\infty$  at the top of the grid (dotted line), the spherical mass loss rate  $\dot{M}$  (upper solid line), the maximum coronal temperature (dashed line)—all in scaled units as listed in the captions—and the dimensionless energy convergence parameter  $\langle \delta E \rangle$  (lower solid line).

largest value that the minimum can take is 1. Tests have shown  $\epsilon_0 = 0.17$  to be a robust value; it represents a practical lower limit to  $\epsilon$  that alleviates making infinitesimally small corrections.

When radial derivatives need to be taken in the ZEPHYR code, we use the following four-point finite differencing scheme,

$$\left( \frac{\partial f}{\partial r} \right)_i = C \left( \frac{f_{i+1} - f_{i-1}}{r_{i+1} - r_{i-1}} \right) + (1 - C) \left( \frac{f_{i+2} - f_{i-2}}{r_{i+2} - r_{i-2}} \right) \quad (66)$$

for discretized quantities  $f_i$  on the radial grid that has unequally spaced heights  $r_i$ . The constant  $C$  determines the weighting between two pairs of centered differences. The limit of  $C = 1$  corresponds to standard two-point finite differencing, which is generally accurate to second order. Further Taylor-series expansion, assuming a constant-spacing grid and a reasonably smooth function  $f(r)$ , would give a result that is accurate to fourth order for  $C = 4/3$ . Note, though, that quantities in the ZEPHYR code are tabulated on a grid with variable spacing and they often exhibit numerical noise. In this case, errors may be reduced by essentially averaging between the  $i \pm 1$  difference and the  $i \pm 2$  difference (i.e., using  $C \approx 0.5$ ). Tests with the ZEPHYR code found that  $C = 0.2$  provides the most accurate differentiation and noise reduction, and this value is used in the models presented below. For the four zones at the bottom ( $i = 1, 2$ ) and top ( $i = N - 1, N$ ) of the grid we use a combination of the standard two-point finite difference expression and linear extrapolation to evaluate the derivatives.

Figure 4 illustrates the convergence of the outer iteration process for the main polar coronal hole model described in § 8.3. The displayed plasma parameters reach reasonably steady final values in about 70 outer iteration steps. The energy convergence parameter  $\langle \delta E \rangle$  decreases to its minimum range of variation (0.01–0.02) in about 100 iterations. Note, though, that  $\langle \delta E \rangle$  is averaged over the entire radial grid; in many parts of the grid the convergence is much better than the average value indicates. Below the chromosphere-corona

transition region the convergence is excellent (i.e.,  $\langle \delta E \rangle$  is always less than  $10^{-4}$ ). In the narrow transition region itself, though, the piecewise smoothing discussed above smears out the temperature distribution so that the ideal “conduction dominated” solution cannot be sustained exactly.<sup>9</sup> Thus, the average value of the convergence parameter for  $10^4 < T < 10^5$  K is about 0.2–0.3. In the corona and solar wind acceleration region above the transition region the average value of the convergence parameter is about 0.01, similar to the global average. If the 30 or so grid zones of the transition region are excluded, the global average  $\langle \delta E \rangle$  is reduced by about a factor of two to  $\sim 0.005$ .

The full ZEPHYR code comprises approximately 2000 lines of Fortran. With the typical iteration parameters given above, the code runs in 2 to 4 hours of CPU time on various Sun Microsystems (Ultra and SunFire) computers.

## 8. RESULTS

In this section we present a series of solar atmosphere models computed by the ZEPHYR code. A series of tests was first performed to evaluate the sensitivity of the dominant plasma properties to various input parameters (§§ 8.1–8.2). We used the grids of test models to determine the most likely input parameters for a detailed model of a flux tube emerging from a polar coronal hole at solar minimum (§ 8.3). Then, using the same input parameters and varying only the radial dependence of the magnetic field  $B_0(r)$ , we modeled the pole-to-equator variation of solar wind conditions at solar minimum (§ 8.4) and explored the properties of slow wind streams that are connected to flux tubes emerging from active regions (§ 8.5).

In addition to the global magnetic field strength (our primary “control knob”) there are three key parameters that we varied in the course of exploring the physics of atmospheric heating and solar wind acceleration:

1. The *photospheric acoustic flux*  $F_{S\odot}$  injected at the lower boundary mainly affects the chromospheric heating. Probable values for  $F_{S\odot}$  seem to range between  $10^7$  and  $10^9$  erg s<sup>-1</sup> cm<sup>-2</sup> (see, e.g., Musielak et al. 1994; Ulmschneider et al. 1996, 2001; Carlsson & Stein 1997; Fawzy et al. 2002). For standard photospheric densities and sound speeds, this gives a range for the photospheric acoustic velocity amplitude  $v_{\parallel\odot}$  of about 0.1 to 1 km s<sup>-1</sup>. These values are a bit smaller than traditional “laminar” granulation velocities of 1 to 2 km s<sup>-1</sup>. The sources of propagating waves are believed to be concentrated in the dark intergranular lanes and thus are able to extract only a fraction of the total kinetic energy of granulation (Rimmele et al. 1995; Nesis et al. 1997, 1999; Cadavid et al. 2003).
2. The *photospheric Alfvén wave amplitude*  $v_{\perp\odot}$  is specified instead of the basal flux  $F_A$  or non-WKB velocity amplitude  $w_{\perp}$ , since the latter quantities depend on the cancellation between upward and downward propagating waves that is determined as a part of the self-consistent solution. Observational determinations of  $w_{\perp}$  from the footpoint motions of G-band

<sup>9</sup> Note that the solar atmosphere should also contain some degree of *ambipolar diffusion* between ions and neutrals (Fontenla et al. 1990, 1991, 1993). This effectively provides additional “smearing” of the otherwise extremely sharp transition region. Our transition region thicknesses resemble those of Fontenla et al. by pure coincidence. None of the derived properties of the model either above or below the transition region appear to depend on this smearing.

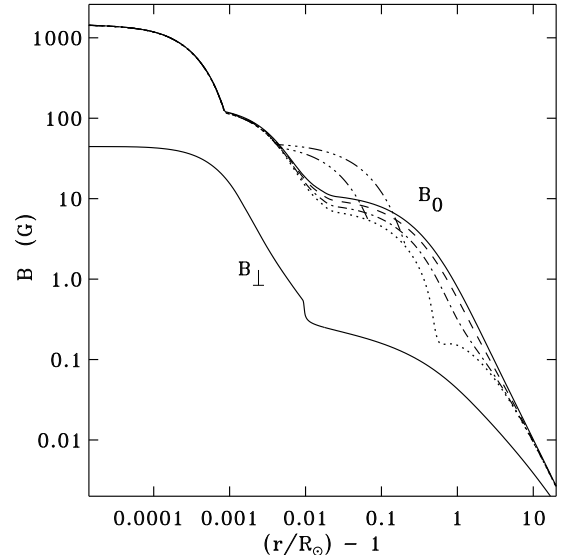


FIG. 5.— Radial dependence of the background magnetic field  $B_0$ . The axisymmetric solar-minimum field of Banaszkiewicz et al. (1998) is shown for field lines originating at  $\theta_0 = 0^\circ$  (upper solid line),  $16^\circ$  (dashed line),  $24^\circ$  (dot-dashed line), and  $29.7^\circ$  (dotted line). All have been modified at low heights using the model of Cranmer & van Ballegoijen (2005). Also shown are example active-region fields for  $h = 0.03$  and  $0.07 R_\odot$  (dash-triple-dot lines) and the computed Alfvén-wave magnetic amplitude  $B_\perp$  for the polar coronal hole model (lower solid line). Above the largest height shown ( $r \approx 20 R_\odot$ ) the magnetic field is nearly exactly radial, with  $B_0 \propto r^{-2}$ .

bright points yield mean values around 1 km s<sup>-1</sup>, with transient speeds up to 5 km s<sup>-1</sup> (e.g., Berger & Title 1996). Larger-scale analyses of the horizontal diffusion of magnetic flux elements give smaller speeds of order 0.1 to 0.3 km s<sup>-1</sup> (Schrijver et al. 1996). Recall that  $v_\perp$  is likely to be factors of 2 to 5 smaller than  $w_\perp$ , so the range of possible values for  $v_{\perp\odot}$  may extend from below 0.1 up to 1 or 2 km s<sup>-1</sup>.

3. The *photospheric Alfvén wave correlation length*  $L_{\perp\odot}$  sets the scale of the turbulent heating rate  $Q_A$  (eq. [47]). Once this parameter is set, the value of  $L_\perp$  at all larger heights is determined by the adopted proportionality with  $B_0^{-1/2}$ . A practical lower limit for  $L_{\perp\odot}$  seems to be about 10 km; i.e., the spatial scale over which radiative diffusion may inhibit the collapse of strong fields into thin flux tubes (e.g., Venkatakrishnan 1986; Sánchez Almeida 2001; Cameron & Galloway 2005). The upper limit may be of the order of the size of photospheric granules ( $\sim 1000$  km). Possible intermediate length scales include the photospheric radius of a thin flux tube (50–100 km), the width of an intergranular lane (about 300 km), and the mean separation between the flux tubes in the supergranular network (350–700 km; see Cranmer & van Ballegoijen 2005).

All other parameters have been fixed with the values given in earlier sections.

### 8.1. Coronal Parameter Study

The test models discussed in this section all used the polar coronal hole magnetic field model that was derived by Cranmer & van Ballegoijen (2005). In the photosphere, chromosphere, and low corona (i.e., from  $z = 0$  to 12 Mm), this model was obtained by tracing the radial magnetic field strength from the central axis of a two-dimensional numerical model



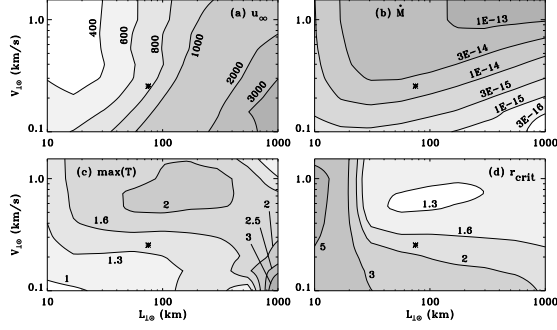


FIG. 6.— Contour plots of solar wind quantities resulting from varying the coronal heating parameters  $v_{\perp\odot}$  and  $L_{\perp\odot}$ : (a) terminal wind speed  $u_{\infty}$  in units of  $\text{km s}^{-1}$ , (b) mass loss rate  $\dot{M}$  in units of  $M_{\odot} \text{ yr}^{-1}$ , (c) maximum coronal temperature in units of MK, (d) heliocentric critical radius in units of  $R_{\odot}$ . Also shown in each panel are the parameters chosen for the model of fast wind from a polar coronal hole discussed in § 8.3 (stars). **SEE LAST PAGE OF PAPER FOR LARGER VERSION.**

of the supergranular network. This model contains thin intergranular flux tubes between the photosphere and a “merging height” of 0.6 Mm where the flux tubes have expanded laterally to the extent that the surrounding field-free plasma disappears. Above this height the merged network element undergoes further funnel-like horizontal expansion to fill a supergranular canopy. The field is directed completely vertically by the height of 12 Mm. Above this height we applied a slightly modified version of the empirically derived solar-minimum magnetic model of Banaszkiewicz et al. (1998). The radial dependence of  $B_0$  is shown in Figure 5.

Figure 6 shows the result of producing a two-dimensional grid of ZEPHYR models by varying  $v_{\perp\odot}$  and  $L_{\perp\odot}$ . The acoustic flux  $F_{S\odot}$  was kept fixed at a median value of  $10^8 \text{ erg s}^{-1} \text{ cm}^{-2}$  (see above). The other two quantities were varied between the limits of  $0.1 \leq v_{\perp\odot} \leq 1.5 \text{ km s}^{-1}$  and  $10 \leq L_{\perp\odot} \leq 1000 \text{ km}$ , with 9 points per quantity spread logarithmically between those limits. Figure 6a displays contours of the “terminal” outflow speed at the upper edge of the spatial grid, which we call  $u_{\infty}$ . This quantity is slightly larger than the outflow speed at 1 AU, but never by more than 5%. Figure 6b shows the spherical mass loss rate, which is defined as

$$\dot{M} = 4\pi\rho ur^2, \quad (67)$$

with the quantities on the right-hand side evaluated at the top of the grid (where  $A \propto r^2$ ). Figures 6c and 6d show the maximum coronal temperature and the heliocentric radius of the wave-modified critical point (see § 6), respectively.

Several general trends are evident in Figure 6. The mass loss rate is primarily dependent on  $v_{\perp\odot}$ , which represents the total amount of Alfvénic wave energy available to be dissipated in the corona. The outflow speed, though, seems to depend mainly on  $L_{\perp\odot}$ ; this parameter tells us *where* the wave energy is damped. For large values of  $L_{\perp\odot}$  the damping occurs over a large range of heights, with increasingly more heating and acceleration taking place above the critical point. It has been known for some time that the relative heights of the critical point and the dominant energy deposition are key in determining the nature of a pressure-driven wind (Leer & Holzer 1980; Pneuman 1980; Leer et al. 1982). Heat that is deposited *above* the critical point is converted nearly completely into kinetic energy of the wind (and a higher value of  $u_{\infty}$ ). On the other hand, low values of  $L_{\perp\odot}$  give a more concentrated heat deposition mostly *below* the critical point. This energy raises the temperature in the subsonic part of the

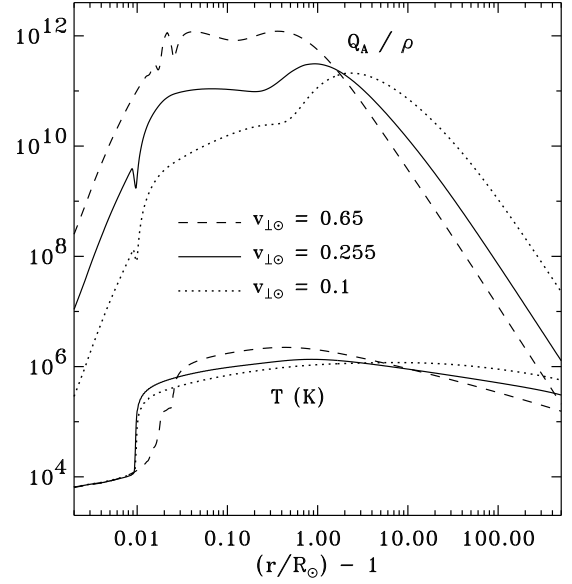


FIG. 7.— Coronal heating rates per unit mass ( $Q_A/\rho$ ) in units of  $\text{erg s}^{-1} \text{ g}^{-1}$  and temperatures (in K) for three models with constant values of  $L_{\perp\odot} = 75 \text{ km}$  and  $F_{S\odot} = 10^8 \text{ erg s}^{-1} \text{ cm}^{-2}$ , and a range of values for  $v_{\perp\odot} = 0.1$  (dotted lines),  $0.255$  (solid lines), and  $0.65 \text{ km s}^{-1}$  (dashed lines).

corona, increases its scale height, and provides more downward heat conduction into the upper transition region. Less energy is thus available to accelerate the wind and  $u_{\infty}$  is lower. The mass loss rate  $\dot{M}$  is generally believed to be set in the transition region by a balance between conduction, radiative losses, and an upward enthalpy flux (e.g., Hammer 1982; Leer et al. 1998).

Interestingly, for a large range of parameters in the lower-right of Figure 6b ( $L_{\perp\odot} \gtrsim 30 \text{ km}$  and  $v_{\perp\odot} \lesssim 0.4 \text{ km/s}$ ), a combined power-law fit to the parameter dependence of the mass loss rate yields good agreement with the ZEPHYR models for  $\dot{M} \propto v_{\perp\odot}^{2.7}/L_{\perp\odot}$ . This resembles the classical Kolmogorov (1941) energy flux due to isotropic hydrodynamic turbulence:  $v^3/\ell$ . It seems to corroborate the general idea that the mass flux of a thermally driven wind is proportional to the deposited coronal energy flux. The large variation in coronal heating, though, does *not* seem to produce a large variation in the maximum coronal temperature. Figure 6c shows that this temperature varies only by about a factor of two over most of the parameter space. Owocki (2004) summarized how the energy losses due to both conduction and the solar wind act as an effective “thermostat” to keep the coronal temperature from varying too widely.

Figure 7 illustrates how the coronal heating rate  $Q_A$  changes as  $v_{\perp\odot}$  is varied and  $L_{\perp\odot}$  is kept fixed. We plot the heating rate per unit mass  $Q_A/\rho$  in order to more easily show which heights receive the most heating on a particle-by-particle basis. Note that larger values of  $v_{\perp\odot}$  produce larger values of both  $Q_A/\rho$  and  $T$  and move their local maxima down to lower heights. The presence of damping, though, leads to differences in how the heating rate depends on  $v_{\perp\odot}$  in various regions. In the lower corona ( $z \approx 0.05 R_{\odot}$ ), before substantial Alfvén-wave damping has had time to occur, the three models show a power-law dependence of  $Q_A/\rho \propto v_{\perp\odot}^{2.58}$  that is similar to the mass loss rate dependence of  $\dot{M} \propto v_{\perp\odot}^{2.11}$  for these models. In the extended corona, though, the *peak value* of  $Q_A/\rho$  (above  $z \approx 0.1 R_{\odot}$ ) varies more weakly as  $v_{\perp\odot}^{0.98}$ . The models with higher Alfvén wave amplitudes have undergone rela-

tively more damping in the extended corona than the models with lower  $v_{\perp}$ .

The above arguments do not explain all of the features of the contours shown in Figure 6. For example, although there is a general trend (in the center and lower-right of Figure 6b) for a decreasing  $L_{\perp\odot}$  to give a larger value of  $\dot{M}$ , the globally largest mass loss rate occurs in the upper-right corner of the plot—i.e., for the largest values of *both*  $v_{\perp\odot}$  and  $L_{\perp\odot}$ . In this region of the plot, added insight can be found in the “cold” wave-driven wind model of Holzer et al. (1983). For undamped Alfvén waves that dominate the critical velocity (eq. [59]) the terminal wind speed and mass loss rate can be computed analytically. Isolating the proportionality with  $v_{\perp\odot}$  in this model yields

$$\dot{M} \propto v_{\perp\odot}^4, \quad u_{\infty}^2 \propto (1/v_{\perp\odot}^2) - \text{constant}, \quad (68)$$

where the constant term is typically negligible, thus giving  $u_{\infty} \propto v_{\perp\odot}^{-1}$  (see eqs. [39] and [41] of Holzer et al. 1983). In the upper-right corners of Figures 6a and 6b, these relations come the closest to being satisfied. Specifically, for  $v_{\perp\odot} > 0.6$  km s<sup>-1</sup> and  $L_{\perp\odot} > 600$  km, the best power-law fits to the model results are  $\dot{M} \propto v_{\perp\odot}^{3.42}$  and  $u_{\infty} \propto v_{\perp\odot}^{-0.89}$ . These parameters indeed correspond to a wave-dominated critical velocity (i.e., large  $v_{\perp\odot}$ ) without much damping (large  $L_{\perp\odot}$ ).

For the entire grid of values shown in Figure 6, a power-law is a poor fit to the overall variations of  $\dot{M}$  and  $u_{\infty}$  as a function of the two input parameters. For completeness, though, we report the best-fitting exponents over the full grid:  $\dot{M} \propto v_{\perp\odot}^{1.7} L_{\perp\odot}^{-0.07}$  and  $u_{\infty} \propto v_{\perp\odot}^{-0.27} L_{\perp\odot}^{0.44}$ .

## 8.2. Chromospheric Parameter Study

We produced a second grid of exploratory ZEPHYR models that kept the coronal heating parameters ( $v_{\perp\odot}$ ,  $L_{\perp\odot}$ ) fixed and varied only the basal acoustic wave flux  $F_{S\odot}$ . As described further in § 8.3, we chose optimal values of  $v_{\perp\odot} = 0.255$  km s<sup>-1</sup> and  $L_{\perp\odot} = 75$  km in order to model the fast wind that emerges from a polar coronal hole (see also the stars in Figure 6). For the median value of  $F_{S\odot} = 10^8$  erg s<sup>-1</sup> cm<sup>-2</sup> used above, the transition region occurs at a relatively large height of  $z = 7200$  km  $\approx 0.01 R_{\odot}$ . A traditional view of chromospheric energy balance is that when the acoustic heating is increased, the height of the transition region should decrease (since the temperature would rise more rapidly as a function of  $z$ ).

Figure 8 shows that the *opposite* actually occurs when we vary  $F_{S\odot}$  and keep everything else fixed. We produced a series of models with  $F_{S\odot} = 10^5, 10^6, 10^7, 10^8, 10^9$ , and  $10^{10}$  erg s<sup>-1</sup> cm<sup>-2</sup>, as well as a model with  $F_{S\odot} = 0$  (i.e., a model with Alfvén wave heating only). The models with  $F_{S\odot} = 0$  and  $10^5$  are virtually identical and the latter is not shown.

Before discussing the chromospheric heating, we first note that the coronal and solar wind parameters for these models are remarkably constant. This shows that varying the acoustic heating has relatively little impact above the transition region. As  $F_{S\odot}$  is increased from zero to its maximum value, the mass loss rate decreases by only 7%, the terminal speed increases by less than 1%, and the peak coronal temperature decreases by 5%.

Why does the transition region height increase as additional chromospheric heating is imposed? The models having larger values of  $F_{S\odot}$  have *larger scale heights* because they have both larger chromospheric temperatures and higher acoustic wave pressures. The larger scale heights lead to a more shal-

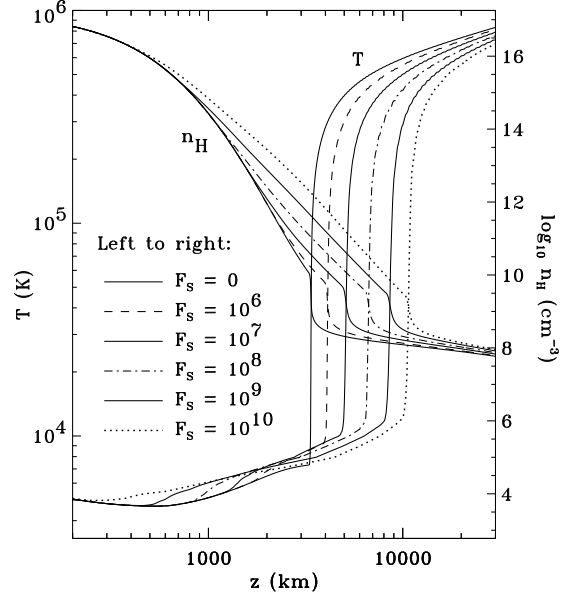


FIG. 8.— Temperature (*left axis*) and hydrogen number density (*right axis*) shown as a function of height above the photosphere (in km) for models that vary the acoustic wave flux  $F_{S\odot}$  (in units of erg s<sup>-1</sup> cm<sup>-2</sup>) and keep the coronal heating parameters  $v_{\perp\odot}$  and  $L_{\perp\odot}$  fixed (see captions).

low density decrease in the approximately hydrostatic chromosphere. The transition region tends to occur at a critical density at which radiative cooling can no longer keep pace with the imposed acoustic heating (i.e., because  $\Lambda(T)$  has reached its peak and can increase no further). The “shallower” models with more acoustic heating reach this critical density at a larger height.

The modeled transition region heights  $z_{\text{TR}}$  range from 3800 km (for  $F_{S\odot} = 0$ ) to 11500 km (for  $F_{S\odot} = 10^{10}$  erg s<sup>-1</sup> cm<sup>-2</sup>). For consistency, we define  $z_{\text{TR}}$  as the height where  $T$  first reaches  $2 \times 10^5$  K, which is the peak of the radiative cooling curve; see Figure 1. These heights are conspicuously larger than the standard values of, e.g., 1700 to 2300 km from “FAL” semi-empirical solar atmosphere models (Fontenla et al. 1993). Although there are some solar limb observations that suggest large values similar to our modeled  $z_{\text{TR}}$  (Zhang et al. 1998), these may be affected by the dynamics of spicules and mass flows along closed magnetic loops, and thus may not be comparable directly to the present models (see also Filippov & Koutchmy 2000).

The relative stretching of the chromospheres shown in Figure 8 can be understood further by examining the density dependence of the total heating rate:  $(Q_S + Q_A) \propto \rho^\eta$ . The exponent  $\eta$  was computed for all of the models by utilizing the radial dependence of both  $\rho$  and the total heating rate, with

$$\eta = \frac{\partial \ln(Q_S + Q_A) / \partial r}{\partial \ln \rho / \partial r}. \quad (69)$$

Because the heating is balanced by radiative cooling (which usually has  $Q_{\text{rad}} \propto \rho^2$ ), we find that values of  $\eta$  closer to 2 give rise to a more extended “matching” between heating and cooling at chromospheric temperatures—and thus a larger overall extent of the chromosphere. Thus, since  $\eta < 2$  for all of the models shown below, we can understand how larger [smaller] values of  $\eta$  correspond to a higher [lower] transition region height. For the shock heating described in § 4.1, the possible values of  $\eta$  range between  $-0.5$  and  $+1$ . The lower limit would occur for an undamped weak shock train, for which  $T \Delta S \propto v_{\parallel}^3$

(eq. [33]) and  $\rho v_{\parallel}^2 = \text{constant}$ . The upper limit occurs when the shock train strengthens to the point where  $v_{\parallel}$  saturates to a nearly constant value and thus  $T\Delta S \approx \text{constant}$ . (The peak Mach number  $M_1$  tends to saturate at values between 2 and 3 for the majority of the  $F_{S\odot}$  models.)

The ZEPHYR models shown in Figure 8 exhibit intermediate values of the density exponent  $\eta$ , with the value of the exponent varying slightly as a function of height in the chromosphere. The lowest value of  $z_{\text{TR}}$  corresponds to the  $F_{S\odot} = 0$  model and  $\eta = 0.4\text{--}0.5$ . The highest value of  $z_{\text{TR}}$  corresponds to the  $F_{S\odot} = 10^{10}$  model and  $\eta = 0.8\text{--}1$ . It is clear that, in these models, an even lower (FAL-like) transition region height would require  $\eta \lesssim 0$ , and thus would require the heating rate to increase with height. Such heating may occur for the following reasons.

1. As described above, if the acoustic wave energy were to act more like a weak undamped shock train,  $\eta$  would approach  $-0.5$ . The emerging picture of the chromosphere as a confluence of multiple acoustic sources (each expanding quasi-spherically from small regions at or below the photosphere) may be consistent with the need for more low-amplitude acoustic wave energy (see, e.g., Ulmschneider et al. 2005). A collection of weak and incoherent acoustic wave packets may also exhibit effectively larger frequencies because of their random phases and constructive interference.
2. There could be additional important sources of linear wave dissipation in the low chromosphere, similar in form to  $\gamma_{\text{cond}}$  (which gives  $\eta \approx -1$  to  $-0.5$  depending on the magnetic geometry). For example, Goodman (2000, 2004) suggested that the resistive dissipation of currents driven by MHD waves may provide enough energy to heat the chromosphere.
3. Similarly, it has been argued on the basis of multiple lines of observational evidence that both solar and stellar chromospheres may be dominated by magnetic and not acoustic heating (e.g., Judge & Carpenter 1998; Judge et al. 2003; Bercik et al. 2005). If these mechanisms grow stronger as one moves from the lower to the upper chromosphere (the latter being more strongly ionized and magnetized), this could produce the radial increase of the total heating rate that would be needed to push down the transition region.

However, we should note that Anderson & Athay (1989a) determined empirically that the chromospheric heating rate seems to be roughly proportional to  $\rho$  (and thus  $\eta \approx 1$ ) throughout most of the chromosphere. The mechanisms included in the ZEPHYR models may thus be reasonable without the need for additional physics.

We experimented with several other variations on the acoustic heating in order to test the assumptions described in § 4. A test model was created with the power spectrum  $P_S(\omega)$  divided into a finer mesh of discrete frequency bins: separated by factors of  $\sqrt{2}$  rather than 2. This model, which had  $F_{S\odot} = 10^8 \text{ erg s}^{-1} \text{ cm}^{-2}$ , produced a nearly identical chromosphere to the standard model with the same value of  $F_{S\odot}$ . The fine-mesh model's transition region height  $z_{\text{TR}}$  was about 10% higher than that of the standard model because slightly more power was given to the lower frequencies (which form shocks at larger heights). Presumably, using a coarser frequency spectrum would lead to a lower value of  $z_{\text{TR}}$ , but

this would start to become unfaithful to the modeled spectral shape (eq. [42]). Another model was run with just a single frequency bin; i.e., a monochromatic low-frequency wave train with  $\omega = \omega_{\text{ac}}$ . This model was designed to explore what would happen if the high-frequency tail in  $P_S(\omega)$  were absent (e.g., Fossum & Carlsson 2005, 2006). This model exhibited  $z_{\text{TR}} = 14300 \text{ km}$ , about a factor of two larger than the standard model, and would certainly require some additional kind of chromospheric heating to produce a realistically low value of  $z_{\text{TR}}$ .

Note that for all of the above models the minimum temperature in the upper photosphere never dropped below the radiative equilibrium value of  $T_{\text{rad}} \approx 4500 \text{ K}$ . There is observational evidence, though, for a lower minimum temperature that could extend intermittently down to values between 3000 to 4000 K (see model A of Fontenla et al. 1993; Carlsson & Stein 1997; as well as recent work by Ayres et al. 2006; Fontenla et al. 2006). Additional sources of cooling that could be included in ZEPHYR include molecular opacity and dust formation (for cooler stars) as well as adiabatic expansion effects due to waves and shocks that may *not* be confined to the modeled flux tube.

### 8.3. Polar Coronal Hole Model

The exploratory models discussed above led to a choice for the optimal set of parameters which would reproduce the observed properties of high-speed solar wind streams that emerge from polar coronal holes (mainly at the minimum of the solar cycle). These parameters are  $v_{\perp\odot} = 0.255 \text{ km s}^{-1}$ ,  $L_{\perp\odot} = 75 \text{ km}$ , and  $F_{S\odot} = 10^8 \text{ erg s}^{-1} \text{ cm}^{-2}$ . The terminal speed  $u_{\infty}$  and mass loss rate  $\dot{M}$  computed for this model are  $753.5 \text{ km s}^{-1}$  and  $1.88 \times 10^{-14} M_{\odot} \text{ yr}^{-1}$ , respectively. These values give a total hydrogen number density of  $2.9 \text{ cm}^{-3}$  at  $r = 1 \text{ AU}$ .

The semi-empirical Alfvénic turbulence model of Cranmer & van Ballegoijen (2005) determined a value for  $L_{\perp}$  at the mid-chromosphere merging height of about 1100 km, which corresponds to a photospheric value  $L_{\perp\odot} \approx 320 \text{ km}$ . The Cranmer & van Ballegoijen (2005) model also predicted a photospheric non-WKB amplitude  $w_{\perp\odot}$  of about  $3.1 \text{ km s}^{-1}$ , which translates into  $v_{\perp\odot} \approx 0.46 \text{ km s}^{-1}$ . These values are both slightly higher than the ones chosen on the basis of the self-consistent ZEPHYR models, though they certainly fall within the range of plausibility. The smaller value of the turbulence correlation length (75 km) seems to be consistent with the observed horizontal size of a thin flux tube in the photosphere (50–100 km). This seems nicely consistent with being an outer “stirring” scale for the turbulence, since the horizontal shaking and distortion of the flux tube can be expected to take place mainly on the spatial scale of its own size. (Earlier justifications for the larger [ $\sim 300 \text{ km}$ ] correlation length were based on this being either the mean separation between flux tubes or the intergranular lane width. These scales may be excited by convective driving as well, but it makes sense for the primary *response* of each tube to be on the smaller scale of its radius or diameter.)

For simplicity we continue to use the fiducial value for  $F_{S\odot}$  that was used in the two-dimensional grid shown in Figure 6. This energy flux density ( $10^8 \text{ erg s}^{-1} \text{ cm}^{-2}$ ) corresponds to a photospheric acoustic wave amplitude  $v_{\parallel\odot}$  of about  $0.29 \text{ km s}^{-1}$ , and it is close to that computed by Musielak et al. (2000) for linear longitudinal flux-tube waves. The flux computed in the Lighthill-Stein sound generation models depends sensitively on the partitioning of gas and magnetic pressure in

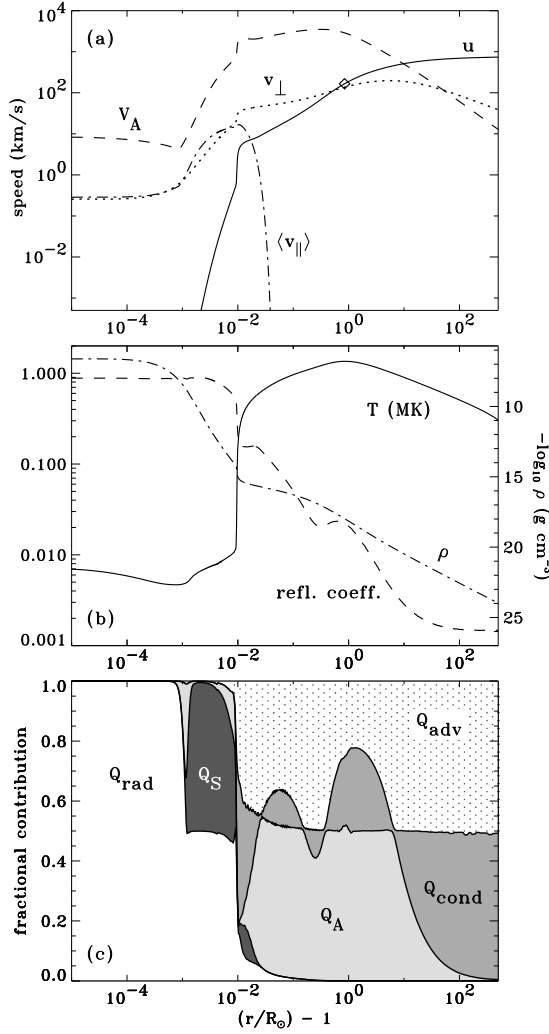


FIG. 9.— Radial dependence of various plasma parameters for a polar coronal hole. (a) Velocity quantities in  $\text{km s}^{-1}$ : wind speed  $u$  (solid line), Alfvén speed  $V_A$  (dashed line), Alfvén wave amplitude  $v_\perp$  (dotted line), acoustic wave amplitude  $\langle v_\parallel \rangle$  (dot-dashed line), and the wave-modified critical point (diamond symbol). (b) Temperature  $T$  in MK (solid line), spectrum-averaged reflection coefficient  $\mathcal{R}$  (dashed line), and mass density  $\rho$  (dot-dashed line; right axis). (c) Areas denote the relative contribution of terms to the energy conservation equation; see labels. ( $Q_{\text{adv}}$  denotes the advection terms on the left-hand side of equation (3), other terms are defined in the text.)

the photosphere; these models have  $F_{S\odot} \propto (B_0/B_{\text{eq}})^{-p}$ , where  $B_{\text{eq}} = (8\pi P)^{1/2}$  is the field strength consistent with equipartition between gas and magnetic pressures, and  $p$  takes on large values typically between 6 and 9. Our polar coronal hole model has a photospheric ratio  $B_0/B_{\text{eq}} = 0.77$ . Interpolating from Table 1 of Musielak et al. (2000) would yield a flux for this model of about  $1.1 \times 10^8 \text{ erg s}^{-1} \text{ cm}^{-2}$ , which is extremely close to what we use.

Figure 9 displays the radial dependence of several key plasma parameters for the polar coronal hole model. The critical point is denoted by a symbol, with  $r_c = 1.84 R_\odot$  and  $u_c = 166 \text{ km s}^{-1}$ . The wave-modified critical point is only a small distance above the classical sonic point, which occurs at  $1.74 R_\odot$  (where  $u = a = 149 \text{ km s}^{-1}$ ). This is somewhat surprising because the fast solar wind is typically assumed to be strongly “wave dominated,” and thus one might have expected the modified critical point to be far from the unmodified sonic point. Both of these points are also near the so-called *turbopause* radius at which the bulk solar wind

speed begins to exceed the turbulent fluctuation amplitude  $v_\perp$  ( $r = 1.54 R_\odot$ ; see Veselovsky 2001). In contrast, the Alfvén singular point (where  $u = V_A$ ) occurs at a substantially larger radius of  $r_A = 10.8 R_\odot$  and  $u_A = 509 \text{ km s}^{-1}$ . Note that Figure 9a displays a frequency-integrated acoustic wave amplitude that we define for convenience as

$$\langle v_\parallel \rangle = \left( \frac{2}{\rho} \sum_{\text{bins}} U_s \right)^{1/2} \quad (70)$$

(see eq. [24]), where we summed over the discrete frequency bins discussed in § 4.2 and assumed  $s = 2$  everywhere. This acoustic wave amplitude peaks at about  $17 \text{ km s}^{-1}$  in the upper chromosphere (and is mildly nonlinear, with  $\langle v_\parallel \rangle / c_s$  peaking there at 0.96), then is damped strongly in the low corona.

The temperature and density curves shown in Figure 9b appear to be in reasonable agreement with prior expectations for the fast solar wind (e.g., Kohl et al. 2006). When  $\rho$  is converted into electron number density  $n_e$ , the modeled values agree with the canonical polar coronal hole measurements of Sittler & Guhathakurta (1999) to within  $\pm 20\%$ . These measurements come mainly from white-light polarization brightness ( $pB$ ) observations between  $r = 1.5$  and  $4 R_\odot$ . Considering that the absolute  $pB$  calibration uncertainties are typically about 10% and that the measured density depends on the filling factor of polar plumes along the line of sight (which introduces  $pB$  variations up to a factor of two in magnitude; see Fisher & Guhathakurta 1995), this agreement is good.

The Alfvén wave amplitudes ( $v_\perp$  in Figure 9a and  $B_\perp$  in Figure 5) compare favorably with the semi-empirical models of Cranmer & van Ballegoijen (2005), who compared those models with various remote-sensing and in situ measurements. The spectrum-averaged reflection coefficient  $\mathcal{R}$  shown in Figure 9b is also similar to that of Cranmer & van Ballegoijen (2005); note that it need not be monotonically decreasing with increasing distance. The photospheric value of  $\mathcal{R}$  in this model is 0.883, which is smaller than the value of 0.974 from Cranmer & van Ballegoijen (2005). The latter model utilized the FAL-C’ temperature structure which had a sharper transition region than that produced by the ZEPHYR code. A more abrupt transition region has a larger  $V_A$  gradient and thus experiences stronger reflection. Defining the transition region thickness  $\delta z_{\text{TR}}$  as the distance between temperatures of  $2 \times 10^4$  and  $2 \times 10^5 \text{ K}$ , the FAL-C’ model has  $\delta z_{\text{TR}} = 120 \text{ km}$  and the ZEPHYR polar coronal hole model has a value of 560 km. Although some of the computed thickness may be due to numerical smoothing (see § 7) not all of it is. The ZEPHYR code did produce a sharper transition region ( $\delta z_{\text{TR}} = 270 \text{ km}$ ) for the  $F_{S\odot} = 0$  model shown in Figure 8—which was also the model with the lowest transition region height  $z_{\text{TR}}$ .

The radial dependence of temperature in the extended corona and heliosphere can be compared with various analytic limiting cases (e.g., Hundhausen 1972). At large distances where the wind speed is approximately constant and  $\rho \propto r^{-2}$ , there are several cases that give a power-law dependence  $T(r) \propto r^{-\beta}$ . The polar coronal hole model shown in Figure 9 exhibits  $\beta \approx 0.30$  at 1 AU. If the advection terms on the left-hand side of equation (3) are dominant, one obtains the purely adiabatic exponent  $\beta = 4/3$ . If classical heat conduction were to dominate the energy equation out to 1 AU,  $\beta = 2/7$ . However, we find that conduction and advection tend to *balance* one another in the heliosphere and yield intermediate values. For the case that the advection terms

are balanced by classical Spitzer-Härm conduction, there is no exact power-law solution for  $T(r)$ . For advection being balanced by collisionless conduction (eq. [22]), one obtains  $\beta = 8/(6 + 3\alpha_c)$ , which for the adopted value  $\alpha_c = 4$  gives  $\beta = 4/9$ . In the ZEPHYR models, the hybrid heat conduction (eq. [14]) is mostly collisionless at 1 AU, but it still contains some classical heat conduction. The computed values of  $\beta$  thus tend to fall between the two above cases of  $2/7$  and  $4/9$ .

Figure 9c shows the terms that dominate the energy conservation equation as a function of distance. The areas plotted here were computed by normalizing the absolute values of the individual terms in equation (3) by the maximum value at each height (as in the denominator of eq. [63]) and then “stacking” them so that together they fill the region between 0 and 1. The photosphere is essentially definable as the region where radiative heating balances radiative cooling (both denoted as  $Q_{\text{rad}}$ ) and the chromosphere is the region where acoustic heating ( $Q_S$ ) balances  $Q_{\text{rad}}$ . The transition region and the very low corona ( $T \lesssim 0.5$  MK) exhibit a complicated balance of radiation, conduction, advection (i.e., enthalpy flux), and some Alfvénic and acoustic heating. The extended corona is mainly a balance between the Alfvén wave heating ( $Q_A$ ) and the advection terms on the left-hand side of equation (3), although conduction remains nonnegligible. In the heliosphere above  $20\text{--}30 R_\odot$  the direct heating becomes less important and advection balances conduction.

In order to produce further comparisons with in situ solar wind measurements, we computed the nonequilibrium ionization balance of oxygen as a function of distance in the ZEPHYR models. Specifically, the ratio of number densities of  $\text{O}^{7+}$  to  $\text{O}^{6+}$  is often used to aid in the identification of fast and slow wind streams (e.g., Zurbuchen et al. 2002). Because of the steep decline in electron density with increasing height, solar wind ions above a certain “freezing-in radius” encounter virtually no electrons, and thus are not sensitive to ionization and recombination processes in interplanetary space (Hundhausen et al. 1968; Owocki et al. 1983). Interplanetary charge states thus carry information about the plasma properties in the corona. We adopted the nonequilibrium ionization code of Gaetz et al. (1988), Esser et al. (1998), and Esser & Edgar (2000, 2001) to the ZEPHYR models at temperatures above  $10^4$  K. Ionization and recombination are most sensitive to the electron velocity distribution in the corona, and we relied on our basic one-fluid assumption of a Maxwellian distribution with  $T = T_e = T_p$ . We also assumed that all oxygen ions flow with the bulk wind speed  $u$ , independent of their charge.

Figure 10 shows the result of computing the oxygen ionization state for the polar coronal hole model. The mean charge state  $\langle Z_O \rangle$  is computed as an average of the net charge of the ions (in units of  $e$ ) weighted by the computed number density fractions of each stage of ionization. The equilibrium solution assumes a local “coronal” balance between collisional ionization, radiative recombination, and dielectronic recombination, and is a strict function of temperature. The full nonequilibrium solution freezes in at a relatively low height in the corona ( $z \approx 0.05 R_\odot$ ) and is roughly constant at all larger heights. Note, though, that the equilibrium and nonequilibrium solutions are also different from one another in the upper transition region ( $z \approx 0.01\text{--}0.02 R_\odot$ ) where the wind flow time over a scale height is beginning to approach the relevant ionization and recombination times. The dominant ionization state at 1 AU is  $\text{O}^{6+}$  (i.e.,  $\langle Z_O \rangle \approx 6$ ) and the ratio of  $\text{O}^{7+}$  to  $\text{O}^{6+}$  is discussed further below.

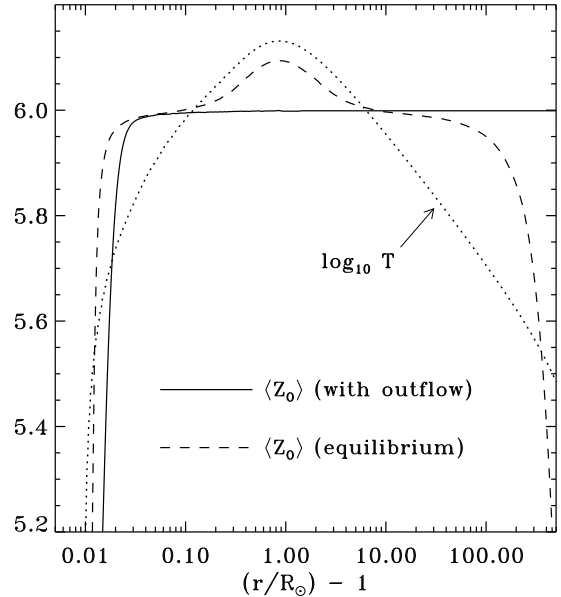


FIG. 10.— Oxygen ionization versus radial distance for the polar coronal hole model. The mean charge states for the nonequilibrium “frozen in” model (solid line) and the local coronal equilibrium (dashed line) are compared with the logarithm of the temperature  $T$ , in K (dotted line).

#### 8.4. Solar Minimum Axisymmetric Field

There is a definite empirical relationship between the solar wind speed measured in situ and the inferred lateral expansion of magnetic flux tubes near the Sun (Levine et al. 1977; Wang & Sheeley 1990; Arge & Pizzo 2000). Specifically, flux tubes that expand more rapidly between the coronal base and  $r \approx 2.5 R_\odot$  tend to have lower wind speeds at 1 AU. There have been many theoretical attempts to explain this observed anticorrelation. Some models have treated the flux expansion as the fundamental cause of the difference between fast and slow streams (e.g., Kovalenko 1978, 1981; Wang & Sheeley 1991, 2006; Wang 1993; Cranmer 2005a), some have treated it as a by-product of varying boundary conditions in the low corona (e.g., Fisk 2003; Schwadron & McComas 2003), and some have considered a combination of the two (Bravo & Stewart 1997; Suzuki 2006).

Our goal is to test these ideas by varying *only* the flux expansion rate and keeping the lower boundary parameters ( $v_{\perp\odot}$ ,  $L_{\perp\odot}$ ,  $F_{S\odot}$ ) fixed. The first way that we modify the flux expansion is to utilize the full two-dimensional axisymmetric magnetic field model of Banaszkiewicz et al. (1998). This model utilizes a sum of dipole, quadrupole, and current-sheet (effective monopole) terms to reproduce various observed properties of the solar-minimum field. Note that other assumptions lead to slightly different solar-minimum field configurations (e.g., Sittler & Guhathakurta 1999, 2002; Vázquez et al. 2003) but the general trends of the polar and equatorial expansion factors are not substantially different from the Banaszkiewicz et al. (1998) case.

Figure 11 illustrates a selection of the open field lines in the Banaszkiewicz et al. (1998) model. Figure 5 also shows the magnetic field  $B_0(r)$  traced along a subset of these field lines. We define the surface colatitude  $\theta_0$  as the main identifier of each flux tube. The polar flux tube that was used above in § 8.3 has  $\theta_0 = 0$ . We take the “last” open field line (at the outermost edge of the open-field region) as  $\theta_0 = 29.7^\circ$ . Because the latter field line eventually stretches to a colatitude of nearly  $90^\circ$  we also call this the “equatorial” flux tube. We

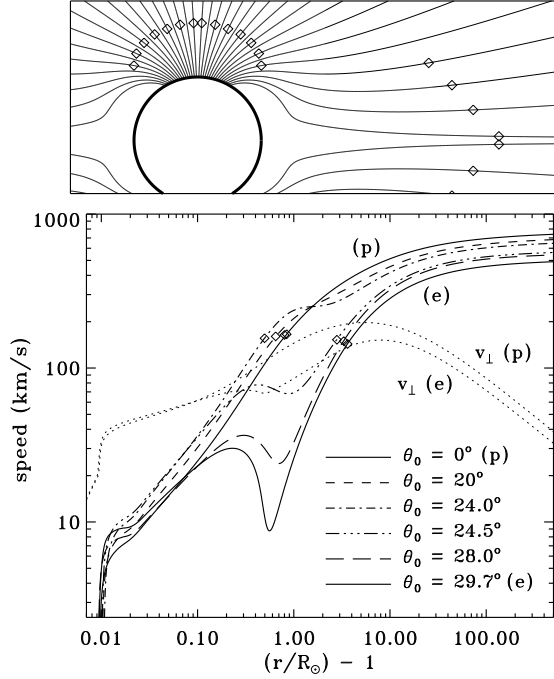


FIG. 11.— *Upper panel:* axisymmetric magnetic field geometry of Banaszkiewicz et al. (1998) with the radii of wave-modified critical points marked by open diamond symbols. *Lower panel:* outflow speeds for a series of axisymmetric flux tube models (surface colatitudes  $\theta_0$  given in captions) with critical point heights denoted by open diamonds, and the Alfvén wave amplitude  $v_\perp$  for the polar (p) and equatorial (e) models (dotted lines).

assume that the differences in  $B_0$  between flux tubes occur only above  $z \approx 0.01 R_\odot$  and that in the photosphere and chromosphere all flux tubes are identical (see, e.g., Aiouaz & Rast 2006).

Let us define an effective Wang & Sheeley (1990) superradial expansion factor for each flux tube as

$$f_{ss} = \frac{(B_0 r^2)_{\text{base}}}{(B_0 r^2)_{ss}} \quad (71)$$

where the coronal base is fixed at  $r_{\text{base}} = 1.04 R_\odot$  (i.e., a height equivalent to the size of one supergranule, well above any “canopy” structure) and we use the traditional source surface radius of  $r_{ss} = 2.5 R_\odot$  (Hoeksema & Scherrer 1986). It would not be proper to use the photosphere as the basal height because the low-resolution magnetograms that typically are used to determine  $f_{ss}$  resolve neither the individual photospheric flux tubes nor the contrast between supergranular network and cell interior. For the Banaszkiewicz et al. (1998) field configuration,  $f_{ss}$  ranges from 4.5 for the polar flux tube to 9.1 for the equatorial flux tube. Note that this model does not produce the larger values of  $f_{ss} \approx 20\text{--}40$  that have been found during more active phases of the solar cycle (see § 8.5).

A series of 20 ZEPHYR models was computed with the same photospheric boundary conditions as the polar coronal hole model discussed in § 8.3, but varying  $\theta_0$  from 0 to  $29.7^\circ$ . Going from pole to equator, the asymptotic solar wind speed  $u_\infty$  was found to decrease and the mass loss rate  $\dot{M}$  was found to increase. Figure 11 shows how the radial dependence of outflow speed changes as  $\theta_0$  increases from 0 to  $29.7^\circ$ . There is an abrupt bifurcation between two classes of solar wind solution: (1) polar solutions that have fast wind speeds, low densities, and wave-modified critical points  $r_c < 2 R_\odot$ , and (2) equatorial solutions that have slow wind speeds, high densities, and  $r_c \gtrsim 4 R_\odot$ . The colatitude at which this bifurcation

occurs is  $\theta_0 \approx 24.25^\circ$ . As discussed by Vázquez et al. (2003) and in § 6 above, when there is more than one possible location for the critical point, the most stable time-steady solution tends to be the one with the largest value of  $r_c$ . For the Banaszkiewicz et al. (1998) field geometry, the second (large- $r_c$ ) solution appears only for  $\theta_0 \gtrsim 24.25^\circ$ . The field line that divides the two classes of solutions extends out to a heliospheric latitude (measured from the ecliptic plane at  $r \gg R_\odot$ ) of  $16^\circ$ .

Figure 11 shows that the solar wind solutions all exhibit substantial wind speeds just above the transition region ( $u \approx 10 \text{ km s}^{-1}$ ). Esser et al. (2005) found that such rapid flows at the coronal base are a consequence of the rapid superradial divergence in supergranular funnels, and that these flows seem to be necessary to explain observed H I Ly $\alpha$  emission from the solar disk. Note also that our modeled flux tubes nearest to the equator exhibit a pronounced local minimum in the wind speed at the cusp-radius of the current sheet in the Banaszkiewicz et al. (1998) model. Observational evidence for this kind of “stagnation point” in equatorial streamers was reported by Strachan et al. (2002) and was also modeled in a similar way as in this paper by Chen et al. (2004) and Li et al. (2004).

It is also evident from Figure 11 that the polar model has a larger Alfvén wave amplitude than the equatorial model. Some of this difference can be attributed directly to the varying flux-tube area factors  $A(r)$  (i.e., different manifestations of wave action conservation). However, the equatorial flux tube also exhibits relatively more damping than the polar model. In the corona, the Alfvén waves essentially “spend more time” at low heights in the equatorial flux tube because of its lower phase speed ( $u + V_A$ ), and this allows a given damping rate  $Q_A$  to have more of an impact on diminishing the wave energy. Thus, the equatorial models exhibit more heating at low heights (due to the increased damping and the higher densities at the coronal base) and less heating at large heights (due to the lower wave amplitudes  $v_\perp$  and larger turbulent correlation lengths  $L_\perp$  in the extended corona). The peak temperature for the polar model,  $T = 1.35 \text{ MK}$ , occurs at  $r = 1.86 R_\odot$ , and the peak temperature for the equatorial model,  $T = 1.29 \text{ MK}$ , has a similar magnitude but occurs at a lower height of  $r = 1.26 R_\odot$  (see also Figure 17 below). This shift in the range of heights over which coronal heating occurs seems to be an important factor in producing a fast solar wind for the polar model (which is heated in the supersonic region) and a slow wind for the equatorial model (which is heated in the subsonic region); see § 8.1. The differences in temperature persist out to 1 AU, where the polar temperature (0.41 MK) exceeds the equatorial temperature (0.16 MK) by a larger relative amount than in the extended corona. The radial temperature exponent  $\beta$  (i.e.,  $T \propto r^{-\beta}$ ) grows steeper from pole ( $\beta \approx 0.30$ ) to equator ( $\beta \approx 0.47$ ).

Although the photospheric Alfvén wave amplitude parameter  $v_{\perp\odot}$  was kept fixed in these models, the degree of non-WKB reflection decreased slightly from the polar to the equatorial flux tube. This resulted in a decrease in the computed value of  $w_{\perp\odot}$  (eq. [56]) from its polar value of  $0.72 \text{ km s}^{-1}$  to an equatorial value of  $0.59 \text{ km s}^{-1}$ . Interestingly, if we could have forced  $w_{\perp\odot}$  to remain fixed as a function of latitude, the resulting equatorial value of  $v_{\perp\odot}$  would have been about 20% larger than the polar value. Figure 6 indicates that the effect would have been an even larger equatorial mass loss rate and a slightly lower  $u_\infty$ . Thus, the current set of models is in some sense “robust” because these effects arise even without such

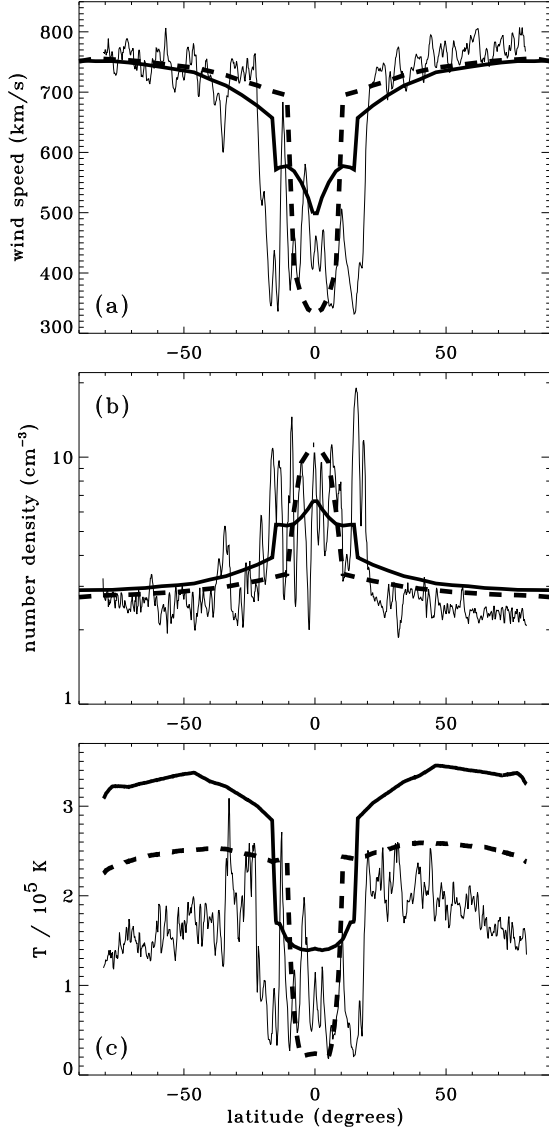


FIG. 12.— Latitudinal dependence of (a) outflow speed, (b) number density, and (c) temperature measured in interplanetary space (see text for details). Data from the *Ulysses* first polar pass (thin solid lines) are compared to the standard ZEPHYR models computed along axisymmetric superradial flux tubes (thick solid lines) and the ‘Durham’ ZEPHYR models computed along the same flux tubes (thick dashed lines).

an extra fine-tuning in  $w_{\perp\odot}$ .

The detailed latitudinal dependence of the ZEPHYR models (for an observer in interplanetary space) is shown in Figure 12. We compare the model predictions with *Ulysses* SWOOPS (Solar Wind Observations Over the Poles of the Sun; Bame et al. 1992) measurements during its first fast latitude scan in 1994 and 1995 (see Goldstein et al. 1996). The measured values for flow speed, proton number density, and proton temperature were obtained at heliocentric distances between 1.3 and 2.3 AU. The densities were scaled to a common distance of 1 AU by using an assumed  $r^{-2}$  dependence. For comparison we plot  $u_{\infty}$ , which does not vary substantially between these distances, and the proton number density ( $n_p = \rho/m_H/1.2$ ) at 1 AU, scaled for an assumed helium-to-hydrogen number density ratio of 0.05. The model temperature  $T(r)$  has been interpolated to varying heights as a function of latitude to match the elliptical orbit of the *Ulysses* probe during its polar pass. Also, we used the Banaszekiewicz et al.

(1998) model to map the surface colatitude  $\theta_0$  of each model flux tube to its corresponding heliospheric latitude at  $r \rightarrow \infty$ . The latter is the abscissa coordinate used in Figure 12. To within about 10% accuracy, one can estimate this latitude as  $|90^\circ - 3\theta_0|$ .

There are two sets of pole-to-equator ZEPHYR models shown in Figure 12. We compare the standard model discussed above with a preliminary model presented by Cranmer (2006), which we hereafter call the ‘Durham’ model.<sup>10</sup> The models differ in two specific ways. (1) The standard model used the Alfvén wave frequency spectrum shown in Figure 3, but the Durham model assumed a single frequency for the Alfvén waves—corresponding to a period of 6 minutes. (2) The standard model used an exponent  $n = 1$  in equation (48), but the Durham model used  $n = 2$ . The latter was an early guess for the functional form of  $\mathcal{E}_{\text{turb}}$  that we used prior to the incorporation of the insights of Oughton et al. (2006). The larger exponent resulted in more efficient quenching of the MHD turbulence in the lower atmosphere, which thus required a larger amount of Alfvén wave energy to produce plasma conditions appropriate for a polar coronal hole. Specifically, the Durham model used  $v_{\perp\odot} = 0.42$  km s<sup>-1</sup>,  $L_{\perp\odot} = 120$  km, and the same value of  $F_{S\odot}$  as was used in the standard model. The Durham model’s  $u_{\infty}$  and  $\dot{M}$  for the polar flux tube were nearly identical to those of the standard model. The peak coronal temperature, though, was substantially larger (2.06 MK) and the temperature at 1 AU was slightly smaller (0.31 MK) in comparison to the standard polar model.

There is reasonably good agreement between the modeled and observed plasma properties shown in Figure 12. We of course do not reproduce any of the measured north-south asymmetry in the data, except for that in  $T_p$  that arose because the path of *Ulysses* was not perfectly north-south symmetric. We also do not attempt to model the rapid near-ecliptic variability that seems to result from longitudinal variations in  $B_0$ . In some sense, the Durham model does better at achieving the low equatorial wind speeds (down to 330 km s<sup>-1</sup>) and high number densities (up to about 10 cm<sup>-3</sup>) that are often observed in the plane of the ecliptic, but that model exhibits a narrower range of slow-wind (large- $r_c$ ) latitudes than both the standard model and the *Ulysses* data. It is expected, though, that some fraction of the observed  $\pm 20^\circ$  latitudinal extent of the slow-wind region may be due to a slight tilt in the main dipole component of the solar magnetic field (i.e., a ‘ballerina skirt’ phenomenon) because the first *Ulysses* polar pass did not occur exactly at the minimum of the activity cycle.

Note from Figure 12c that the ZEPHYR model temperatures between 1.3 and 2.3 AU are systematically higher than the measured values of  $T_p$ . The trend as a function of the coupled distance-latitude coordinate, though, is similar to the measurements. Our heliospheric temperatures are sensitive to the adopted method of bridging between collisional and collisionless heat conduction (eq. [14]) and the present method is admittedly somewhat ad hoc. However, some of the discrepancy in Figure 12c may come from the fact that  $T_p \neq T_e$  in interplanetary space and that we are essentially modeling their average. In situ measurements have shown that  $T_p > T_e$  in the fast solar wind and  $T_p < T_e$  in the slow wind (see, e.g., Feldman & Marsch 1997). The discrepancy is worst in the

<sup>10</sup> This model was presented at the 37th meeting of the Solar Physics Division of the American Astronomical Society in Durham, New Hampshire (25–30 June 2006).

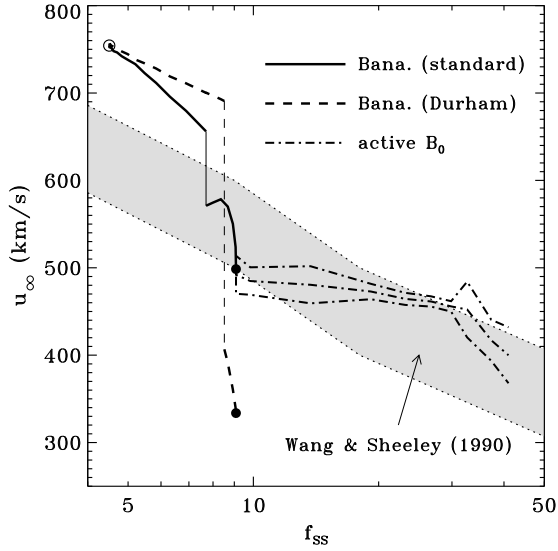


FIG. 13.— Terminal outflow speeds for the various sets of ZEPHYR models plotted versus the flux-tube expansion factor  $f_{ss}$  (eq. [71]), compared with the empirically derived relationship from Table 2 of Wang & Sheeley (1990). The standard (solid line) and Durham (dashed line) pole-to-equator models computed using the Banaszkiewicz magnetic field are shown along with the active-region extensions to equatorial  $B_0(r)$  discussed in § 8.5 (dot-dashed lines). The polar (open circle) and equatorial (filled circles) axisymmetric models are highlighted.

polar, fast-wind regions where our modeled average temperature would exceed *both* the observed  $T_p$  and  $T_e$ . However, the ZEPHYR code does not yet contain the dissipative physical processes that would lead to temperature equilibration between protons and electrons; these may alter subtly both the net heating and the form of the conduction flux  $q_{||}$ .

Figure 13 plots the terminal speeds of the standard and Durham ZEPHYR models as a function of the Wang-Sheeley superradial expansion factor  $f_{ss}$ . The abrupt changes in  $u_\infty$  that occur because of the emergence of the outer critical point are evident as vertical discontinuities at the critical values of  $\theta_0$ . Because of the relatively narrow range of  $f_{ss}$  values subtended by the pole-to-equator (Banaszkiewicz et al. 1998) flux tubes, we see that the standard model actually follows the the empirical Wang & Sheeley (1990) relationship better than the Durham model, despite the fact that the standard model has a relatively high equatorial terminal speed of  $500 \text{ km s}^{-1}$ .

Figure 14 compares modeled and measured Alfvén wave amplitudes in the heliosphere as a function of the in situ wind speed. It is difficult to process the richly nonlinear turbulent fluctuations (as measured in situ) into a single “amplitude,” so we made an attempt to convert the ZEPHYR values of  $v_\perp$  into something analogous to the frequency-averaged Elsasser spectrum quantities reported by Tu et al. (1992). Those data were obtained by the two *Helios* spacecraft between 0.29 and 0.52 AU in the years 1979–1980. (Measurements taken closest to the Sun are optimal if the goal is to obtain the properties of the “pristine” Alfvén waves.) Individual time series of  $Z^2/2$  (outward-propagating kinetic energy) magnitudes for one-day periods were transformed into power spectra, denoted  $e^+(f)$ . The values shown in Figure 14 were averaged over frequencies  $f$  between  $10^{-4}$  and  $2 \times 10^{-4}$  Hz. The plotted data points also correspond to time periods when the solar wind exhibited its highest range of total energy flux ( $F_{\text{tot}} = \rho u[u^2 + v_{\text{esc}}^2]/2$ ), which we verified to correspond most closely with the ZEPHYR model results.

We extracted the Elsasser amplitudes  $Z_\perp$  from the models

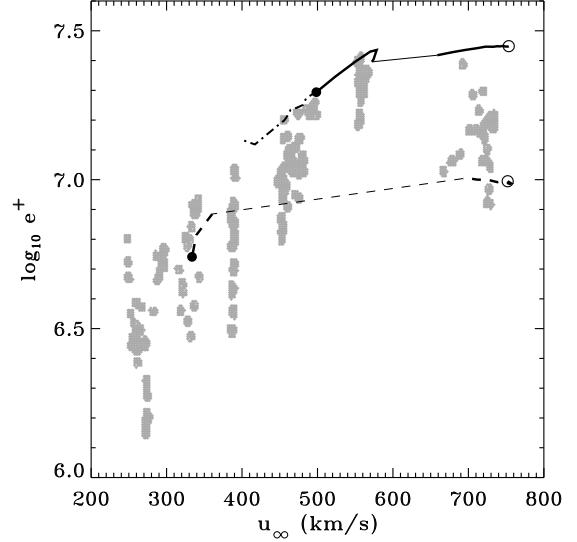


FIG. 14.— Comparison of *Helios* Elsasser spectra  $e^+$  at  $r = 0.3\text{--}0.5$  AU with ZEPHYR model predictions at a mean distance of  $r = 0.4$  AU. Data from Figure 3 of Tu et al. (1992) is shown (gray points). Standard (solid line) and Durham (dashed line) pole-to-equator models are plotted together with active-region flux tube models (dot-dashed lines) in a similar way as in Figure 13.

at a mean distance of  $r = 0.4$  AU and converted them into the average value of  $e^+$  as follows. First, representative spectral shapes for these fluctuations were used in order to determine how much of the total energy is contributed by the specified frequency band ( $1\text{--}2 \times 10^{-4}$  Hz). We used the power-law exponents and breakpoints reported by Tu et al. (1989), using the same *Helios* data, to determine that fast and slow wind streams contain approximately 11% and 21%, respectively, of their power in this band. We used a mean value of 16% for all ZEPHYR models to avoid introducing any possibly spurious correlations with wind speed. To convert the (implicitly frequency-integrated) energy fraction into an “average” spectrum quantity we divided by an effective frequency  $f_{\text{eff}}$  that was defined to perform this conversion exactly for the idealized spectra of Tu et al. (1989); it turned out that  $f_{\text{eff}} \approx 9.5 \times 10^{-5}$  Hz for both fast and slow wind spectra and we used just  $10^{-4}$  Hz. Thus we plot the derived quantity

$$e^+ = \frac{0.16(Z_\perp^2/2)}{10^{-4} \text{ Hz}} \text{ km}^2 \text{ s}^{-2} \text{ Hz}^{-1} \quad (72)$$

in Figure 14 in order to compare with the measured average spectra from Tu et al. (1992). The modeled and measured values—and trends with wind speed—appear to agree quite nicely.

In the remainder of this section we discuss two supplementary calculations of in situ quantities that are often used to diagnose the properties of fast and slow wind streams: the ionization fraction (Figure 15) and the FIP effect (Figure 16).

1. The *nonequilibrium oxygen ionization state* at 1 AU has been computed for each of the standard and Durham model flux tubes. Figure 15 shows the ratio of  $\text{O}^{7+}$  to  $\text{O}^{6+}$  number densities as a function of the modeled terminal speed. These are compared to statistical summaries of *Ulysses* SWICS (Solar Wind Ion Composition Spectrometer; Gloeckler et al. 1992) measurements of this ratio taken during two time periods: the first polar pass discussed above (September 1994 to August 1995) and the initial phase of the mission that sampled the peak of the solar cycle (December 1990 to September 1994). The data points, obtained from the online database of



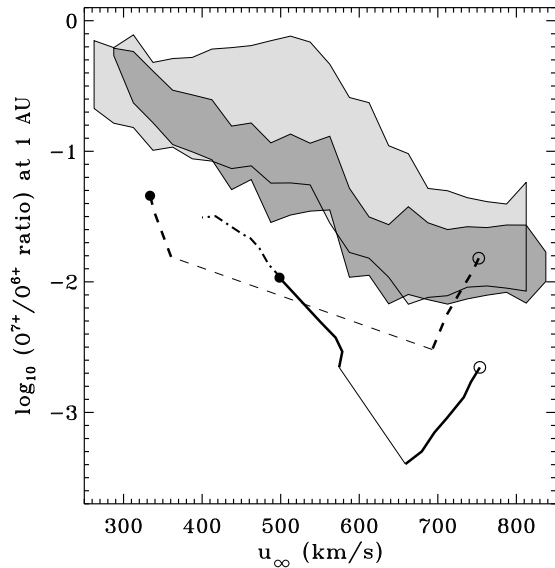


FIG. 15.— Oxygen freezing-in ratio (i.e., ratio of  $O^{7+}$  to  $O^{6+}$  number densities) at 1 AU plotted as a function of solar wind speed in interplanetary space. Symbols and line styles for the models are the same as in Figure 14. Binned *Ulysses* data from the 1990–1994 solar maximum time period (light gray region) and the 1994–1995 fast latitude scan (dark gray region) are shown for comparison.

T. Zurbuchen and R. von Steiger (see also von Steiger et al. 2000), were grouped in sequential bins of wind speed of size  $25 \text{ km s}^{-1}$ , and the mean and standard deviation of the ionization ratio in each bin were computed. The regions plotted in Figure 15 show the values within  $\pm 1$  standard deviations of the mean for each bin in the two data sets.

The general trend of the pole-to-equator ZEPHYR models is for lower wind speeds to have higher ratios of  $O^{7+}$  to  $O^{6+}$  at 1 AU, in qualitative agreement with the observations. The absolute values of the modeled ionization ratios, though, are up to an order of magnitude lower than the *Ulysses* measurements, with slightly better agreement for the hotter Durham models. This discrepancy may be the result of our simple assumption of Maxwellian electron distributions and equal flow speeds for all ion charge states (see, e.g., Esser & Edgar 2000, 2001). A ubiquitous weak “halo” of suprathermal electrons in the low corona could be responsible for the larger overall degree of ionization that is observed.

As one moves from the polar flux tube to the middle latitudes (i.e., from  $u_\infty \approx 750 \text{ km s}^{-1}$  down to about  $650 \text{ km s}^{-1}$ ) the modeled ionization ratio decreases, but then as one passes the bifurcation point between the low and high critical radii, the ionization ratio increases for the rest of the way from the mid-latitude region to the equator. The overall trend for slow wind to have a high ionization ratio is expected because of the higher temperatures in the narrow zone just above the transition region. In fact, the temperature at a constant height of  $z \approx 0.013 R_\odot$  has the same quantitative trend as the modeled  $O^{7+}$  to  $O^{6+}$  ratios: there is an initial decrease from the polar model (0.37 MK) to just before the bifurcation latitude (0.28 MK), then an abrupt jump back to nearly the polar value (0.34 MK) followed by a steady increase toward the equatorial flux tube (0.46 MK). The freezing in occurs at about this height, so it makes sense that the ionization state tracks these variations. Notice that this ionization ratio is sensitive only to the temperature trends at low heights (and that the  $O^{7+}$  to  $O^{6+}$  ratio freezes in just above the transition region) and is *not* sensitive to the temperatures at larger heights in most of the

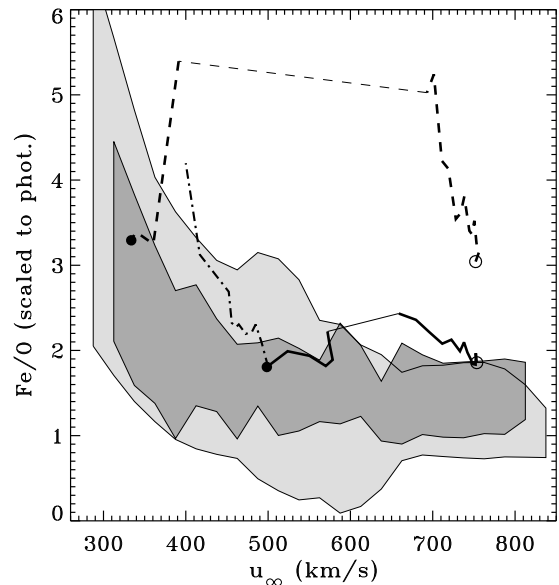


FIG. 16.— FIP fractionation ratio of Fe to O abundance in units of their photospheric abundances. Symbols, line styles, and grayscale regions are the same as in Figure 15.

extended corona. Some interpretations of the in situ charge states make the implicit assumption that high electron temperatures in the slow wind must persist all the way through the extended corona into interplanetary space, and our models show that this need not be the case.

2. A specific diagnostic of *FIP fractionation* has been computed for each of the standard and Durham model flux tubes. Figure 16 shows a commonly measured ratio of the abundances of a low-FIP element (Fe, 7.9 eV) and a moderately high-FIP element (O, 13.6 eV) normalized to their photospheric abundance ratio. We solved equation (62) as described in § 6, and by Laming (2004), for the various models and compared the ratios to the *Ulysses* SWICS observations of the Fe/O ratio. The SWICS ratio was normalized to an assumed photospheric iron-to-oxygen abundance ratio of 0.0468 (Grevesse & Sauval 1998) and the modeled quantity is naturally in units of the photospheric ratio. Because the FIP fractionation takes place in the uppermost part of the chromosphere (which is largely optically thin) and the very low transition region, we assumed “coronal” ionization equilibrium to hold for the modeled Fe and O ions. We used the code developed by Cranmer (2000) to compute the Fe and O ionization fractions  $\xi_s$  that are used in equation (62); the rates were taken largely from Mazzotta et al. (1998).

Figure 16 shows that our standard pole-to-equator ZEPHYR model exhibits a roughly constant Fe/O ratio of about 2 for outflow speeds between 500 and  $750 \text{ km s}^{-1}$ . This is in reasonable agreement with the *Ulysses* data, which have a roughly constant mean value of about 1.5 over these speeds. The Durham model varies nonmonotonically between ratios of about 3 and 5.5 over its wider range of outflow speeds and is clearly inconsistent with most of the in situ data. The equatorial Durham model, with  $u_\infty \approx 330 \text{ km s}^{-1}$ , does seem to fall into agreement with the measured data, but the overall trend as a function of wind speed is not the same. The most promising models for matching the observed trend for a steep enhancement of the Fe/O ratio (as the wind speed decreases from 500 to  $300 \text{ km s}^{-1}$ ) appear to be the active-region flux tubes discussed below in § 8.5.

We should note that an alternate theoretical explanation for

FIP fractionation may also be consistent with the ZEPHYR models. Wang (1996) proposed that flux tubes with a stronger degree of downward heat conduction in the low corona could give rise to a larger amount of transient evaporative outflow of protons relative to neutral hydrogen atoms. These protons could collisionally dredge up singly ionized species (which are preferentially low-FIP) from the transition region and upper chromosphere. In our models, the maximum value of  $|Q_{\text{cond}}|$  occurs within the transition region (at  $T \approx 10^5$  K), and in the equatorial models this peak value is consistently *larger* than in the polar models. The ratio of equatorial to polar maximum conduction rates is 1.7 for the standard model and 2.8 for the Durham model. Whether this is enough to produce a FIP effect with Wang’s (1996) mechanism is not known, but the variations are at least in the correct qualitative direction to produce more of an effect in the slow wind than in the fast wind. Note, though, that Schwadron et al. (1999) disagree with some of the basic assumptions of the Wang (1996) mechanism, and a definitive explanation for the FIP effect remains elusive.

There are additional observational diagnostics that appear to be correlated with fast and slow wind speeds. Kojima et al. (2004) and Suzuki (2006) found that the ratio of basal magnetic field strength to the superradial flux-tube divergence factor (i.e.,  $B_{\text{base}}/f_{\text{ss}}$ ) may be a better predictor of solar wind speed than just using  $f_{\text{ss}}$  itself (see, however, Wang & Sheeley 2006). McIntosh & Leamon (2005) found that the difference in formation heights between the emission seen in the TRACE 1600 Å and 1700 Å filter bandpasses could be a useful diagnostic of the eventual wind speed in flux tubes that are associated with specific regions on the solar surface. Although there have been numerous observational inferences of blueshifts (i.e., outflow) in various spectral lines, it is unclear to what degree these may be utilized as empirical “lower boundary conditions” for solar wind flux tubes (see reviews by Peter et al. 2004; Jones 2005). Finally, there are definite fast/slow wind correlations in the wealth of existing turbulence measurements—both in situ and remote sensing—that could be key tests of models that use waves and turbulence for energy and momentum deposition. Future development of the ZEPHYR models will encompass such additional comparisons.

### 8.5. Active Corona

At times other than solar minimum, the coronal magnetic field is substantially more complex than the axisymmetric configuration modeled in the previous section. During the approach to solar maximum the large polar coronal holes disappear as magnetic flux of the opposite polarity is brought toward the poles. Active regions with strong fields emerge at all latitudes and give rise to an interconnected web of closed loops and intermittent open flux tubes. In the extended corona, active regions often have the appearance of cusp-like “active streamers” that seem like smaller, more intense versions of the quiescent equatorial streamers that dominate at solar minimum (Newkirk 1967; Liewer et al. 2001; Ko et al. 2002). There is increasing evidence that much of the slow solar wind is connected somehow to open flux tubes that are rooted in or near active regions (e.g., Neugebauer et al. 2002; Liewer et al. 2004).

We investigated several different ways to model active-region flux tubes with the ZEPHYR code. First, we explored just changing the radial location of the cusp in the equatorial Banaszkiewicz et al. (1998) flux tube. Observationally,

streamers exhibit a wide range of cusp heights which gives rise to a large variation in their rates of superradial expansion. The cusp height was varied by first computing the ratio of the equatorial ( $\theta_0 = 29.7^\circ$ ) to the polar ( $\theta_0 = 0$ ) magnetic fields  $B_0(z)$ , as shown in Figure 5, then shifting the height coordinate  $z$  either upward or downward by a constant multiplier. The “new” equatorial field was obtained by taking the product of this shifted ratio and the polar field strength. Changing the cusp height by up to a factor of two in either direction did not have much of an effect on the resulting solar wind properties. The mass loss rates varied by about 18% for these models (lower cusps having lower  $\dot{M}$ ), whereas the terminal speeds  $u_\infty$  varied by less than 3%. This near constancy in the solar wind speed occurred despite the fact that  $f_{\text{ss}}$  was made to increase and decrease by factors of  $\sim 2$  about the equatorial value of 9.1.

The above models cannot be considered true active-streamer models because they were not given the significantly *stronger* mean magnetic field strengths that active regions are observed to have in the lower atmosphere. On the smallest scales in the photosphere, plage and active regions exhibit a much higher filling factor of strong-field flux concentrations than quiet regions and coronal holes. In the most tightly-packed active regions these flux concentrations do not appear as isolated flux tubes but instead as fluted ribbons, buckled flux sheets, and flower-like patterns (e.g., Berger et al. 2004; Rouppe van der Voort et al. 2005). We are concerned here only with the subset of magnetic flux that extends out into interplanetary space, so we provisionally retain the “flux tube” picture. We thus modeled  $B_0(r)$  in an active-region flux tube by enhancing the field strength in the chromosphere and low corona. This is done in general agreement with the larger observed magnetic fields, but also to account for the smaller area  $A(r)$  subtended by open flux tubes that are “crowded” by neighboring closed loops in active regions.

We added an active-field component to the standard equatorial Banaszkiewicz et al. (1998) magnetic field by taking

$$B_0(z) = \max \left[ B_E(z), B_A e^{-z/h} \right] \quad (73)$$

where  $B_E(z)$  is the equatorial ( $\theta_0 = 29.7^\circ$ ) model and  $B_A$  is a constant that we set at 50 G. We produced a grid of models that varied the scale height  $h$  between 0 and  $0.07 R_\odot$ . The model with  $h \rightarrow 0$  is equivalent to the standard equatorial model with no active-field enhancement. Equation (73) takes the greater of the two magnetic field quantities, which tends to retain the original  $B_E$  in the photosphere, low chromosphere, and outer corona and wind, but produces the active-region enhancement in the upper chromosphere and low corona (see Figure 5). The smallest values of the scale height ( $h < 0.008 R_\odot$ ) do not produce any enhancement in  $B_0$  because the quantity  $B_A e^{-z/h}$  is rapidly decreasing and it never exceeds  $B_E$ . For larger values of  $h$ , the magnetic field strength at the coronal base is enhanced and thus the Wang-Sheeley expansion factor  $f_{\text{ss}}$  is enhanced as well. The maximum value of  $h = 0.07 R_\odot$  (i.e., 49 Mm) corresponds to  $f_{\text{ss}} = 41$ . Even though we used the exact values of  $f_{\text{ss}}$  computed for each model in the plots below, we found the following approximate fit to be a useful illustration of how  $f_{\text{ss}}$  depends on  $h$ :

$$f_{\text{ss}} \approx \begin{cases} 9.1, & h < 0.02 R_\odot \\ 9.1 + |3026(h - 0.02)|^{0.7}, & h \geq 0.02 R_\odot \end{cases} \quad (74)$$

where  $h$  is in units of  $R_\odot$ . The threshold value of  $0.02 R_\odot$  corresponds to the point at which  $B_A e^{-z/h}$  first produces a significant enhancement at  $z_{\text{base}} = 0.04 R_\odot$ .

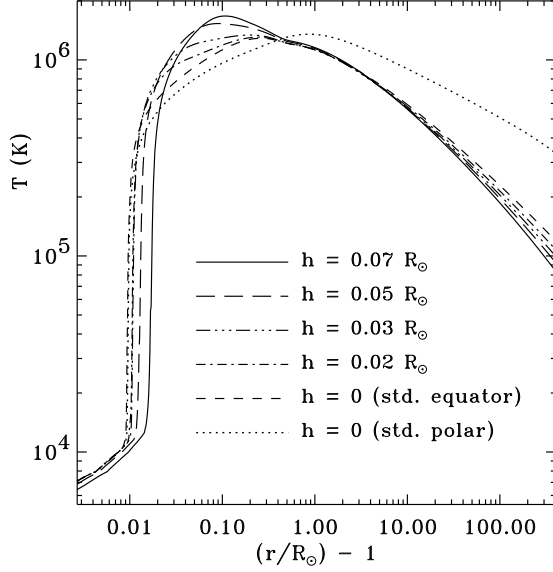


FIG. 17.— Radial dependence of temperature  $T$  for a selection of ZEPHYR models, highlighting the active-region extensions to the equatorial  $B_0(r)$  discussed in § 8.5 (see captions). For comparison the standard-model polar (dotted line) and equatorial (dashed line) model temperatures are also shown.

ZEPHYR models were computed for active region field enhancements with  $h = 0.015, 0.02, 0.024, 0.03, 0.035, 0.04, 0.045, 0.05, 0.06$ , and  $0.07 R_\odot$ . The active region models exhibited lower terminal speeds and higher mass loss rates than the standard equatorial model. As  $h$  was increased from 0 to  $0.07 R_\odot$ ,  $u_\infty$  decreased from 500 to about 390 km/s. The mass loss rate increased from  $2.9 \times 10^{-14}$  to  $3.5 \times 10^{-14} M_\odot \text{ yr}^{-1}$ , thus increasing the proton number density at 1 AU from  $6.4 \text{ cm}^{-3}$  to about  $10 \text{ cm}^{-3}$ . Figure 13 shows how  $u_\infty$  decreases as  $f_{ss}$  increases for these models. There is reasonable agreement with the empirical Wang & Sheeley (1990) relationship, and it is important to reiterate that all models in Figure 13 were produced by fixing the basal parameters ( $v_{\perp\odot}$ ,  $L_{\perp\odot}$ ,  $F_{S\odot}$ ) at values appropriate for the polar coronal hole and varying only the magnetic field above the photosphere in order to produce the fast-to-slow wind transitions.

Figures 15 and 16 illustrate the computed  $\text{O}^{7+}$  to  $\text{O}^{6+}$  freezing-in ratios and Fe/O (FIP fractionation) ratios for the active region models. These models mirror the observed trends for there to be larger ratios for both quantities at lower wind speeds. The strengthening of the FIP ratio, from  $\sim 1.5$  to 4 as the wind speed decreases from 500 to 400 km s $^{-1}$ , is especially comparable to the observed increase toward the lowest speeds.

Figure 17 compares the radial dependence of temperature for a selection of active models to that for the standard polar and equatorial models. As  $h$  increases from 0 to  $0.07 R_\odot$ , the peak coronal temperature increases from the equatorial model’s value of 1.29 MK up to 1.67 MK. The heliocentric radius of this peak decreases from 1.26 to  $1.11 R_\odot$ . These trends appear to be a continuation of the variations in coronal heating from the polar to the equatorial flux tubes. As one progresses from pole to equator ( $h = 0$ ) to active region ( $h > 0$ ), the models show a successively stronger decrease in the Alfvén speed with height, more reflection (and damping) in the low corona, and thus less Alfvén wave power available to heights at and above the critical point.

The iterative convergence for the largest- $h$  active region ZEPHYR models was slower and less robust than for the mod-

els discussed in §§ 8.1–8.4. The models having  $0.035 \leq h \leq 0.07 R_\odot$  were run for 400 outer iterations in order to reach acceptable convergence parameter values:  $\langle \delta E \rangle \approx 0.01$  to 0.02. (Trial models with even larger values of  $h \geq 0.09 R_\odot$  did not converge below  $\langle \delta E \rangle \approx 0.04$  after 400 iterations and were not used.) Unlike in Figure 4, where acceptable values of 0.01–0.02 were retained in nearly every iteration (after 100 or so outer iterations had passed), the active models exhibited these values only sporadically. Thus, the iteration with the lowest value of  $\langle \delta E \rangle$  did not necessarily represent the “best” single solution. In order to evaluate the most likely time-steady plasma parameters, we considered a collection of the lowest- $\langle \delta E \rangle$  solutions sampled from the iteration stream for each model run. This was done by taking the distribution of values for a given parameter, such as  $u_\infty$ , for all 400 outer iterations and weighting it by a factor proportional to  $\langle \delta E \rangle^{-2}$  in order to deemphasize the early iterations that are farthest from convergence. Figure 13 shows both the mean and  $\pm 1$  standard deviation values for this weighted distribution of well-converged terminal speed solutions. As  $h$  is increased, the standard deviation first decreases from about 20 to 6 km s $^{-1}$ , then increases again to 35 km s $^{-1}$ .

It is unclear whether the nonconvergence of the large- $h$  active region models represents a failing of the numerical technique or an intrinsic lack of a steady-state solution. The coronal sources of slow solar wind are traditionally viewed as more variable and filamentary than the source regions of fast wind. High-resolution coronagraphic observations of streamers reveal an almost continual release of low-contrast density inhomogeneities (Sheeley et al. 1997; Wang et al. 2000). Multidimensional simulations of streamers have also exhibited time-variable solutions (e.g., Suess et al. 1996; Endeve et al. 2003, 2004). For flux tubes in the vicinity of the boundary between open and closed magnetic fields, the complex interplay between heat conduction and transverse pressure balance can lead to various instabilities that drive variability. Certain open magnetic field configurations (possibly like the one adopted in eq. [73]) may not be stable when considered in the context of its neighbors in a full-Sun model.

Other techniques for constructing active-region solar wind models should be explored. The specific functional form of the  $B_0$  enhancement in the low corona can be improved in order to agree with, e.g., force-free magnetic field reconstructions of active regions (Schrijver et al. 2006). In addition, the photospheric field strength may also be substantially higher in active regions than elsewhere. It is unclear at first glance how the photospheric wave fluxes would be modified in these regions, though. For strong enough basal fields (i.e., in sunspots) convection is quenched and the wave fluxes should be lower. However, active regions exhibit a larger degree of magnetic flux emergence (e.g., Abramenko et al. 2006) which could increase the frequency of impulsive horizontal “jumps” exhibited by flux-tube footpoints. As summarized above, flux tubes are more more highly concentrated in active-region intergranular lanes than elsewhere. The close presence of additional flux tubes may either increase the basal wave amplitude in a given tube (via “sympathetic” motions from the neighbors) or decrease it (because large horizontal displacements are blocked by the neighbors). Similarly, the correlation length  $L_{\perp\odot}$  in these regions may be either lower (because of the smaller domain of motion when crowded) or higher (because the lane-filled “ribbons” may move together). Comparisons between high-resolution observations of G-band bright points in active regions (Möstl et al. 2006)

and three-dimensional magnetoconvection simulations (e.g., Bushby & Houghton 2005) are needed in order to clarify these competing effects.

## 9. SUMMARY AND DISCUSSION

The primary aim of this paper has been to construct self-consistent models of chromospheric and coronal heating, waves and turbulence, and wind acceleration in an open magnetic flux tube rooted in the solar photosphere. A key aspect of the ZEPHYR models presented above is that the only true free parameters are: (1) the properties of the waves injected at the base, and (2) the background geometry and magnetic field strength along the modeled flux tubes. Everything else (e.g., the radial dependence of the rates of chromospheric and coronal heating, the resulting temperature structure of the atmosphere, and the solar wind speed and mass flux) is an emergent property of the model and not an ad hoc input. In the above sense, the ZEPHYR models are similar to those of Suzuki & Inutsuka (2005, 2006); the differences between the two approaches involve mainly the specific physical processes that are assumed to dissipate the Alfvén waves and heat the corona.

As discussed in § 2, the ZEPHYR models presented here are limited by being one-dimensional, time-independent, and one-fluid solutions to the hydrodynamic conservation equations, with heating that is derived only from a subset of all possible wave and turbulent dissipation processes. Even so, the results given in § 8 show that a realistic variation of asymptotic solar wind conditions can be produced by varying only the background magnetic field geometry, as predicted by Wang & Sheeley (1990, 1991, 2003, 2006). Specifically, our models show general agreement with some well known empirical correlations: i.e., a larger  $f_{ss}$  (expansion factor) gives rise to a slower and denser wind, less intense Alfvénic fluctuations at 1 AU, and larger values of both the  $O^{7+}/O^{6+}$  charge state ratio and the FIP-sensitive Fe/O abundance ratio. Satisfying these kinds of scalings are necessary but not sufficient conditions for validating the idea that the wind is driven by a combination of MHD turbulence and non-WKB Alfvén wave reflection.

Future work must involve more physical realism for the models, expanded comparisons with existing observations, and predictions of as-yet unobserved quantities that may be key discriminators between competing theoretical models. An important component of all three efforts will be to model the divergent temperatures and flow speeds of protons, electrons, and various heavy ion species in the extended corona and heliosphere. These mainly *collisionless* regions allow the kinetic physics of wave dissipation to be probed to a level of detail not possible in a collisionally coupled (i.e., essentially one-fluid) plasma. Even in a perfectly collisional plasma, there can be *macroscopic* dynamical consequences depending on how the energy is deposited into protons, electrons, and possibly heavy ions as well. For example, if all of the heat goes into electrons, there can be substantially more downward conduction than in a proton-heated model, which would affect the coronal temperature distribution (Hansteen & Leer 1995) and the stability of helmet streamers (Endeve et al. 2004). Two-fluid effects also may affect the phenomenological form of the MHD turbulent cascade assumed in the above models (e.g., Galtier 2006).

The original motivation for this work was to understand the preferential ion heating and acceleration in the corona revealed by the UVCS (Ultraviolet Coronagraph Spectrom-

eter) instrument on *SOHO* (Kohl et al. 1995, 1997, 2006). If MHD turbulence gives rise to cyclotron-resonant Alfvén waves—which are likely to be responsible for the observed ion properties—then we must first have a large-scale description of the energy flux injected into the turbulent cascade in order to further model the end-products of that cascade. We hope to link the macroscopic properties modeled by ZEPHYR with the microscopic kinetic processes studied by, e.g., Leamon et al. (1999, 2000), Cranmer & van Ballegoijen (2003), Voitenko & Goossens (2003, 2004), Gary & Nishimura (2004), Dmitruk et al. (2004), Chandran (2005), Gary et al. (2006), and Markovskii et al. (2006).

In addition to increasing the realism (and complexity) of the models, attempts should be made to extract the dominant physical processes of these models and create simpler “scaling laws” that can be used to estimate the wind conditions for varying magnetic field geometries and photospheric wave properties (see also Leer et al. 1982; Schwadron & McComas 2003; Suzuki 2006). An obstacle to accomplishing this for the present ZEPHYR models is that the Alfvén wave reflection is nontrivially coupled to the plasma state via the Alfvén speed  $V_A$  and solar wind speed  $u$  (and their gradients). The radial dependence of these quantities cannot be derived a priori from just the background magnetic field  $B_0(r)$ . Approximations for  $Z_-$  and  $Z_+$  such as those given by Dmitruk et al. (2002) should be tested further to evaluate ways of estimating the amount of reflection without having to solve the full non-WKB equations.

We also intend to use the methodology developed here to model the winds of other kinds of stars on the cool side of the Hertzsprung-Russell (H-R) diagram. Similar ideas are beginning to be applied to younger and older stars with solar-type winds (e.g., Airapetian et al. 2000; Falceta-Gonçalves et al. 2006; Suzuki 2007; Holzwarth & Jardine 2007). A benefit of computing the Alfvén wave evolution with a physically motivated damping rate (like eq. [47]) is that the artificial “damping lengths” used in the past are no longer needed. Many cool stars that exhibit observational evidence for winds have lower surface gravities than the Sun, stronger X-ray emission (i.e., more coronal heating), and much larger mass loss rates. These properties are likely to be causally linked, but no comprehensive and predictive models yet exist.

In order to model cool-star winds with ZEPHYR we must have values for the input parameters that drive the atmospheric heating and wind acceleration. For example, we must be able to predict the properties of waves at the photospheric lower boundary for a given star. Amplitudes can be estimated from existing models of flux-tube wave generation from turbulent convection. Figure 18 shows an example of how transverse kink-mode wave amplitudes in stellar photospheres (for which we retain the symbol  $v_{\perp\odot}$ ) can be estimated from the peak value of the subphotospheric convective velocity  $u_{c,\max}$ . Musielak et al. (2000) computed a series of stellar interior models with a range of effective temperatures (2000 to 10000 K) and surface gravities ( $\log g = 3, 4$ , and 5, with  $g$  in units of  $\text{cm s}^{-2}$ ) and presented the maximum values of the ratio  $u_{c,\max}/c_s$  in their Figure 1. Also, Musielak & Ulmschneider (2002) computed the photospheric transverse wave fluxes for the same grid of stellar models. We rescaled both quantities into velocity units using a sound speed consistent with  $T_{\text{eff}}$ , a magnetic field strength consistent with the degree of pressure equipartition assumed by Musielak et al., and a photospheric density computed from the condition  $\kappa_R \rho H = 1$ , where  $H$  is the photospheric scale height (proportional to  $T_{\text{eff}}/g$ ) and  $\kappa_R$

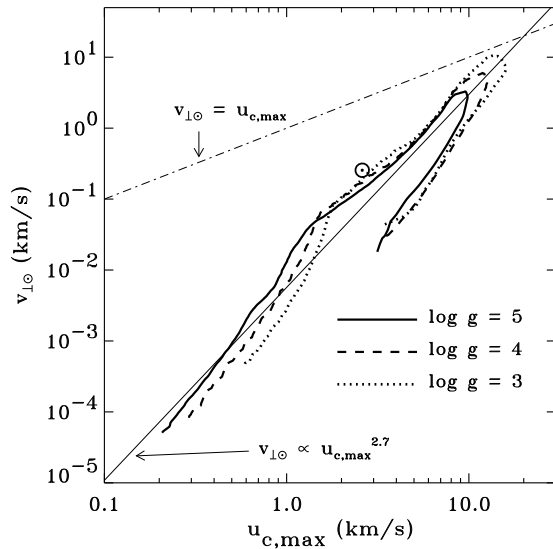


FIG. 18.— Photospheric transverse velocity amplitude  $v_{\perp\odot}$  estimated from turbulent convection models of Musielak et al. (2000) and Musielak & Ulmschneider (2002), plotted against the maximum convective velocity  $u_{c,\max}$  from below the photosphere. Models are for Population I stars with  $T_{\text{eff}}$  ranging from 2000 to 10000 K and  $\log g = 5$  (solid line), 4 (dashed line), and 3 (dotted line). The solar values used in this paper are denoted by the Sun symbol ( $\odot$ ).

is the Rosseland mean opacity interpolated from the same tables used in other parts of the ZEPHYR code (see also Cranmer 2005b). Note that although the two velocities span many orders of magnitude they “collapse” into something close to a one-to-one power-law relation (with  $v_{\perp\odot} \propto u_{c,\max}^{2.7}$ ), and that

the solar value used in § 8 coincides reasonably closely with the model curves.

Another key input to cool-star wind models is an adequate description of the large-scale magnetic field. Observational determinations of the field geometries of rapidly rotating young stars have been made possible via Zeeman-Doppler imaging (e.g., Donati et al. 1990, 2003), time-resolved X-ray spectroscopy (Hussain et al. 2005), and combinations of these and related techniques. However, not enough is known about how the magnetic flux tubes break up—and penetrate the photosphere—on spatial scales relevant to convective granulation and supergranulation. The relationship between the star-averaged mean field strength and the stronger fields inferred for thin flux tubes is not yet well understood (e.g., Saar 2001). Ongoing improvements in the observations make possible more comprehensive and predictive models. We anticipate that phenomenological approaches like those described in this paper can contribute to substantial progress in our understanding of magnetic activity, coronal heating, and wind mass loss in a wide range of stars.

The authors would like to thank Wolfgang Kalkofen, Jonathan Slavin, Eugene Avrett, Rudy Loeser, and Takeru Suzuki for valuable discussions. This work was supported by the National Aeronautics and Space Administration (NASA) under grants NNG04GE77G, NNX06AG95G, and NAG5-11913 to the Smithsonian Astrophysical Observatory. This research made extensive use of NASA’s Astrophysics Data System.

#### REFERENCES

- Abramenko, V. I., Fisk, L. A., & Yurchyshyn, V. B. 2006, *ApJ*, 641, L65  
 Aiouaz, T., & Rast, M. P. 2006, *ApJ*, 647, L183  
 Airapetian, V. S., Ofman, L., Robinson, R. D., Carpenter, K., & Davila, J. 2000, *ApJ*, 528, 965  
 Alazraki, G., & Couturier, P. 1971, *A&A*, 13, 380  
 Alfvén, H. 1947, *MNRAS*, 107, 211  
 Anderson, L. S., & Athay, R. G. 1989a, *ApJ*, 336, 1089  
 Anderson, L. S., & Athay, R. G. 1989b, *ApJ*, 346, 1010  
 Arge, C. N., & Mullan, D. J. 1998, *Sol. Phys.*, 182, 293  
 Arge, C. N., & Pizzo, V. J. 2000, *J. Geophys. Res.*, 105, 10465  
 Aschwanden, M. J. 2006, *Physics of the Solar Corona: An Introduction with Problems and Solutions*, 2nd ed. (Berlin: Springer)  
 Avrett, E. H., & Loeser, R. 1992, in *Cool Stars, Stellar Systems, and the Sun*, 7th Cambridge Workshop, ed. M. Giampapa & J. Bookbinder, ASP Conf. Ser. 26, 489  
 Ayres, T. R., Plymate, C., & Keller, C. U. 2006, *ApJS*, 165, 618  
 Bame, S. J., McComas, D. J., Barraclough, B. L., Phillips, J. L., Sofaly, K. J., Chavez, J. C., Goldstein, B. E., & Sakurai, R. K. 1992, *A&AS*, 92, 237  
 Banaszkiewicz, M., Axford, W. I., & McKenzie, J. F. 1998, *A&A*, 337, 940  
 Barkhudarov, M. R. 1991, *Sol. Phys.*, 135, 131  
 Belcher, J. W. 1971, *ApJ*, 168, 509  
 Bercik, D. J., Fisher, G. H., Johns-Krull, C. M., & Abbett, W. P. 2005, *ApJ*, 631, 529  
 Berger, T. E., Löfdahl, M. G., Shine, R. S., & Title, A. M. 1998, *ApJ*, 495, 973  
 Berger, T. E., Rouppe van der Voort, L. H. M., Löfdahl, M. G., Carlsson, M., Fossum, A., Hansteen, V. H., Marthinussen, E., Title, A., & Scharmer, G. 2004, *A&A*, 428, 613  
 Berger, T. E., & Title, A. M. 1996, *ApJ*, 463, 365  
 Bertschinger, E., & Chevalier, R. A. 1985, *ApJ*, 299, 167  
 Bhattacharjee, A., & Ng, C. S. 2001, *ApJ*, 548, 318  
 Biermann, L. 1948, *ZAp*, 25, 161  
 Bogdan, T. J., et al. 2002, *Astron. Nachr.*, 323, 196  
 Bogdan, T. J., et al. 2003, *ApJ*, 599, 626  
 Borovsky, J. E. 2006, *Texture of the Solar-Wind Plasma* (paper presented at the SHINE 2006 Workshop, Zermatt, Utah)  
 Bowen, G. H. 1988, *ApJ*, 329, 299  
 Braginskii, S. I. 1965, *Rev. Plasma Phys.*, 1, 205  
 Bravo, S., & Stewart, G. A. 1997, *ApJ*, 489, 992  
 Bretherton, F. P., & Garrett, C. J. R. 1968, *Proc. Roy. Soc. A*, 302, 529  
 Bruno, R., Carbone, V., Veltri, P., Pietropaolo, E., & Bavassano, B. 2001, *Planet. Space Sci.*, 49, 1201  
 Bushby, P. J., & Houghton, S. M. 2005, *MNRAS*, 362, 313  
 Cadavid, A. C., Lawrence, J. K., Berger, T. E., & Ruzmaikin, A. 2003, *ApJ*, 586, 1409  
 Cameron, R., & Galloway, D. 2005, *MNRAS*, 358, 1025  
 Canfield, R. C., & Ricchiazzi, P. J. 1980, *ApJ*, 239, 1036  
 Canullo, M. V., Costa, A., & Ferro-Fontán, C. 1996, *ApJ*, 462, 1005  
 Carlsson, M., & Stein, R. F. 1992, *ApJ*, 397, L59  
 Carlsson, M., & Stein, R. F. 1997, *ApJ*, 481, 500  
 Carlsson, M., & Stein, R. F. 2002, *ApJ*, 572, 626  
 Chae, J., Poland, A. I., & Aschwanden, M. J. 2002, *ApJ*, 581, 726  
 Chandran, B. D. G. 2005, *Phys. Rev. Lett.*, 95, 265004  
 Chandrasekhar, S. 1934, *MNRAS*, 94, 444  
 Chen, Y., Esser, R., Strachan, L., & Hu, Y. 2004, *ApJ*, 602, 415  
 Cho, J., Lazarian, A., & Vishniac, E. T. 2002, *ApJ*, 564, 291  
 Choudhuri, A. R., Dikpati, M., & Banerjee, D. 1993, *ApJ*, 413, 811  
 Coleman, P. J., Jr. 1968, *ApJ*, 153, 371  
 Collins, G. W., II 1989, *The Fundamentals of Stellar Astrophysics* (New York: Freeman)  
 Cox, D. P., & Tucker, W. H. 1969, *ApJ*, 157, 1157  
 Craig, I. J. D., & Davys, J. W. 1984, *Sol. Phys.*, 90, 343  
 Cranmer, S. R. 2000, *ApJ*, 532, 1197  
 Cranmer, S. R. 2001, *J. Geophys. Res.*, 106, 24937  
 Cranmer, S. R. 2002, *Space Sci. Rev.*, 101, 229  
 Cranmer, S. R. 2005a, in *Solar Wind 11/SOHO-16: Connecting Sun and Heliosphere*, ed. B. Fleck, T. Zurbuchen, & H. Lacoste (Noordwijk, The Netherlands: ESA), ESA SP-592, 159, astro-ph/0506508  
 Cranmer, S. R. 2005b, *ApJ*, 634, 585  
 Cranmer, S. R. 2006, *BAAS*, 38, 249 (SPD abstract 21.01)  
 Cranmer, S. R., Field, G. B., & Kohl, J. L. 1999, *ApJ*, 518, 937  
 Cranmer, S. R., & van Ballegoijen, A. A. 2003, *ApJ*, 594, 573  
 Cranmer, S. R., & van Ballegoijen, A. A. 2005, *ApJS*, 156, 265  
 Cuntz, M., Rammacher, W., & Musielak, Z. E. 2007, *ApJ*, 657, L57  
 Cuperman, S., & Dryer, M. 1985, *ApJ*, 298, 414  
 DeCampli, W. M. 1981, *ApJ*, 244, 124

- DeForest, C. E. 2004, *ApJ*, 617, L89
- Dennis, J. E., & Schnabel, R. B. 1983, *Numerical Methods for Unconstrained Optimization and Nonlinear Equations* (Englewood Cliffs, NJ: Prentice-Hall)
- Dewar, R. L. 1970, *Phys. Fluids*, 13, 2710
- Dmitruk, P., & Matthaeus, W. H. 2003, *ApJ*, 597, 1097
- Dmitruk, P., Matthaeus, W. H., Milano, L. J., Oughton, S., Zank, G. P., & Mullan, D. J. 2002, *ApJ*, 575, 571
- Dmitruk, P., Matthaeus, W. H., & Seenu, N. 2004, *ApJ*, 617, 667
- Dmitruk, P., Milano, L. J., & Matthaeus, W. H. 2001, *ApJ*, 548, 482
- Dobrowolny, M., Mangeney, A., & Veltri, P. 1980, *Phys. Rev. Lett.*, 45, 144
- Donati, J.-F., Semel, M., Rees, D. E., Taylor, K., & Robinson, R. D. 1990, *A&A*, 232, L1
- Donati, J.-F., et al. 2003, *MNRAS*, 345, 1145
- Elsasser, W. M. 1950, *Phys. Rev.*, 79, 183
- Endeve, E., Leer, E., & Holzer, T. E. 2003, *ApJ*, 589, 1040
- Endeve, E., Holzer, T. E., & Leer, E. 2004, *ApJ*, 603, 307
- Esser, R., Edgar, R. J., & Brickhouse, N. S. 1998, *ApJ*, 498, 448
- Esser, R., & Edgar, R. J. 2000, *ApJ*, 532, L71
- Esser, R., & Edgar, R. J. 2001, *ApJ*, 563, 1055
- Esser, R., Lie-Svendsen, Ø., Janse, Å. M., & Killie, M. A. 2005, *ApJ*, 629, L61
- Falceta-Gonçalves, D., Vidotto, A. A., & Jatenco-Pereira, V. 2006, *MNRAS*, 368, 1145
- Fawzy, D., Rammacher, W., Ulmschneider, P., Musielak, Z. E., & Stepień, K. 2002, *A&A*, 386, 971
- Feldman, W. C., & Marsch, E. 1997, in *Cosmic Winds and the Heliosphere*, ed. J. R. Jokipii, C. P. Sonett, & M. S. Giampapa (Tucson: U. Arizona Press), 617
- Ferguson, J. W., & Ferland, G. J. 1997, *ApJ*, 479, 363
- Ferland, G. J., Peterson, B. M., Horne, K., Welsh, W. F., & Nahar, S. N. 1992, *ApJ*, 387, 95
- Filippov, B., & Koutchmy, S. 2000, *Sol. Phys.*, 196, 311
- Fisher, R. R., & Guhathakurta, M. 1995, *ApJ*, 447, L139
- Fisk, L. A. 2003, *J. Geophys. Res.*, 108 (A4), 1157, doi:10.1029/2002JA009284
- Fontenla, J. M., Avrett, E. H., & Loeser, R. 1990, *ApJ*, 355, 700
- Fontenla, J. M., Avrett, E. H., & Loeser, R. 1991, *ApJ*, 377, 712
- Fontenla, J. M., Avrett, E. H., & Loeser, R. 1993, *ApJ*, 406, 319
- Fontenla, J. M., Avrett, E. H., & Loeser, R. 2002, *ApJ*, 572, 636
- Fontenla, J. M., Balasubramaniam, K. S., & Harder, J. 2006, *ApJ*, submitted
- Forslund, D. W. 1970, *J. Geophys. Res.*, 75, 17
- Fossum, A., & Carlsson, M. 2005, *Nature*, 435, 919
- Fossum, A., & Carlsson, M. 2006, *ApJ*, 646, 579
- Gaetz, T. J., Edgar, R. J., & Chevalier, R. A. 1988, *ApJ*, 329, 927
- Galtier, S. 2006, *J. Plasma Phys.*, 72, 721
- Gary, S. P., & Nishimura, K. 2004, *J. Geophys. Res.*, 109, A02109, doi:10.1029/2003JA010239
- Gary, S. P., Yin, L., & Winske, D. 2006, *J. Geophys. Res.*, 111, A06105, doi:10.1029/2005JA011552
- Giacalone, J., & Jokipii, J. R. 2004, *ApJ*, 616, 573
- Giacalone, J., Jokipii, J. R., & Matthaeus, W. H. 2006, *ApJ*, 641, L61
- Giuliani, P., & Carbone, V. 1998, *Europhys. Lett.*, 43, 527
- Gloeckler, G., et al. 1992, *A&AS*, 92, 267
- Goldreich, P., & Sridhar, S. 1995, *ApJ*, 438, 763
- Goldreich, P., & Sridhar, S. 1997, *ApJ*, 485, 680
- Goldstein, B. E., et al. 1996, *A&A*, 316, 296
- Goldstein, M. L. 1978, *ApJ*, 219, 700
- Goldstein, M. L., Roberts, D. A., & Matthaeus, W. H. 1995, *ARA&A*, 33, 283
- Gómez, D. O., Dmitruk, P. A., & Milano, L. J. 2000, *Sol. Phys.*, 195, 299
- Goodman, M. L. 2000, *ApJ*, 533, 501
- Goodman, M. L. 2004, *A&A*, 424, 691
- Grevesse, N., & Sauval, A. J. 1998, *Space Sci. Rev.*, 85, 161
- Gudiksen, B. V. 2005, in *Solar Wind 11/SOHO-16: Connecting Sun and Heliosphere*, ed. B. Fleck, T. Zurbuchen, & H. Lacoste (Noordwijk, The Netherlands: ESA), ESA SP-592, 165
- Hammer, R. 1982, *ApJ*, 259, 767
- Hansteen, V. H., & Leer, E. 1995, *J. Geophys. Res.*, 100, 21577
- Hansteen, V. H., Leer, E., & Holzer, T. E. 1997, *ApJ*, 482, 498
- Hartmann, L., & MacGregor, K. B. 1980, *ApJ*, 242, 260
- Hasan, S. S., Kalkofen, W., & van Ballegoijen, A. A. 2000, *ApJ*, 535, L67
- Heinemann, M., & Olbert, S. 1980, *J. Geophys. Res.*, 85, 1311
- Hendrix, D. L., & van Hoven, G. 1996, *ApJ*, 467, 887
- Higdon, J. C. 1984, *ApJ*, 285, 109
- Hoeksema, J. T., & Scherrer, P. H. 1986, *Sol. Phys.*, 105, 205
- Hollweg, J. V. 1974, *J. Geophys. Res.*, 79, 3845
- Hollweg, J. V. 1976, *J. Geophys. Res.*, 81, 1649
- Hollweg, J. V. 1986, *J. Geophys. Res.*, 91, 4111
- Hollweg, J. V., & Isenberg, P. A. 2002, *J. Geophys. Res.*, 107 (A7), 1147, doi:10.1029/2001JA000270
- Holzer, T. E., Flå, T., & Leer, E. 1983, *ApJ*, 275, 808
- Holzwarth, V., & Jardine, M. 2007, *A&A*, in press, astro-ph/0611430
- Hopf, E. 1930, *MNRAS*, 90, 287
- Hopf, E. 1932, *MNRAS*, 92, 863
- Hossain, M., Gray, P. C., Pontius, D. H., Jr., Matthaeus, W. H., & Oughton, S. 1995, *Phys. Fluids*, 7, 2886
- Hu, Y. Q., Esser, R., & Habbal, S. R. 2000, *J. Geophys. Res.*, 105, 5093
- Hundhausen, A. J. 1972, *Coronal Expansion and Solar Wind* (Berlin: Springer-Verlag)
- Hundhausen, A. J., Gilbert, H. E., & Bame, S. J. 1968, *ApJ*, 152, L3
- Hung, R. J., & Barnes, A. 1973, *ApJ*, 180, 253
- Hussain, G. A. J., et al. 2005, *ApJ*, 621, 999
- Iroshnikov, P. S. 1963, *AZh*, 40, 742
- Isenberg, P. A. 1990, *J. Geophys. Res.*, 95, 6437
- Isenberg, P. A., & Hollweg, J. V. 1982, *J. Geophys. Res.*, 87, 5023
- Jacques, S. A. 1977, *ApJ*, 215, 942
- Jayanti, V., & Hollweg, J. V. 1993, *J. Geophys. Res.*, 98, 19049
- Jiménez, A. 2006, *ApJ*, 646, 1398
- Jokipii, J. R., & Davis, L., Jr. 1969, *ApJ*, 156, 110
- Jokipii, J. R., & Parker, E. N. 1969, *ApJ*, 155, 777
- Jones, H. P. 2005, in *Large-scale Structures and their Role in Solar Activity*, ed. K. Sankarasubramanian, M. Penn, & A. Pevtsov, ASP Conf. Ser. 346, 229
- Judge, P. G., Carlsson, M., & Stein, R. F. 2003, *ApJ*, 597, 1158
- Judge, P. G., & Carpenter, K. G. 1998, *ApJ*, 494, 828
- Kalkofen, W., Ulmschneider, P., & Avrett, E. H. 1999, *ApJ*, 521, L141
- Klimchuk, J. A. 2006, *Sol. Phys.*, 234, 41
- Ko, Y.-K., Raymond, J. C., Li, J., Ciaravella, A., Michels, J., Fineschi, S., & Wu, R. 2002, *ApJ*, 578, 979
- Kohl, J. L., Noci, G., Cranmer, S. R., & Raymond, J. C. 2006, *A&A Rev.*, 13, 31
- Kohl, J. L., et al. 1995, *Sol. Phys.*, 162, 313
- Kohl, J. L., et al. 1997, *Sol. Phys.*, 175, 613
- Kohl, J. L., et al. 1998, *ApJ*, 501, L127
- Kojima, M., Fujiki, K.-I., Hirano, M., Tokumaru, M., Ohmi, T., & Hakamada, K. 2004, in *The Sun and the Heliosphere as an Integrated System*, ed. G. Poletto & S. T. Suess (Dordrecht: Kluwer), 147
- Kolmogorov, A. N. 1941, *Dokl. Akad. Nauk SSSR*, 30, 301
- Koninx, J. P. M. 1992, Ph.D. Dissertation, Rijksuniversiteit Utrecht
- Kopp, R. A., & Holzer, T. E. 1976, *Sol. Phys.*, 49, 43
- Kovalenko, V. A. 1978, *Geomagnetism & Aeronomy*, 18, 529
- Kovalenko, V. A. 1981, *Sol. Phys.*, 73, 383
- Kraichnan, R. H. 1965, *Phys. Fluids*, 8, 1385
- Kuin, N. P. M., & Poland, A. I. 1991, *ApJ*, 370, 763
- Kuperus, M., Ionson, J. A., & Spicer, D. S. 1981, *ARA&A*, 19, 7
- Kurucz, R. L. 1992, in *IAU Symp. 149, The Stellar Populations of Galaxies*, ed. B. Barbuy & A. Renzini (Dordrecht: Kluwer), 225
- Laming, J. M. 2004, *ApJ*, 614, 1063
- Landau, L. D., & Lifshitz, E. M. 1959, *Fluid Mechanics* (Reading, Mass.: Addison-Wesley)
- Landi, S., & Pantellini, F. 2003, *A&A*, 400, 769
- Leamon, R. J., Matthaeus, W. H., Smith, C. W., Zank, G. P., Mullan, D. J., & Oughton, S. 2000, *ApJ*, 537, 1054
- Leamon, R. J., Smith, C. W., Ness, N. F., & Wong, H. K. 1999, *J. Geophys. Res.*, 104, 22331
- Leer, E., Hansteen, V. H., & Holzer, T. E. 1998, in *Cyclical Variability in Stellar Winds*, ed. L. Kaper & A. W. Fullerton (Berlin: Springer-Verlag), 263
- Leer, E., & Holzer, T. E. 1980, *J. Geophys. Res.*, 85, 4631
- Leer, E., Holzer, T. E., & Flå, T. 1982, *Space Sci. Rev.*, 33, 161
- Levine, R. H., Altschuler, M. D., & Harvey, J. W. 1977, *J. Geophys. Res.*, 82, 1061
- Li, B., Li, X., Hu, Y.-Q., & Habbal, S. R. 2004, *J. Geophys. Res.*, 109, A07103, doi:10.1029/2003JA010313
- Li, X. 2002, *ApJ*, 571, L67
- Li, X. 2003, *A&A*, 406, 345
- Li, X., Habbal, S. R., Hollweg, J. V., & Esser, R. 1999, *J. Geophys. Res.*, 104, 2521
- Lie-Svendsen, Ø., & Esser, R. 2005, *ApJ*, 618, 1057
- Liewer, P. C., et al. 2001, *J. Geophys. Res.*, 106, 15903
- Liewer, P. C., Neugebauer, M., & Zurbuchen, T. H. 2004, *Sol. Phys.*, 223, 209
- Lighthill, M. J. 1952, *Proc. Roy. Soc. A*, 211, 564
- Lionello, R., Riley, P., Linker, J. A., & Mikić, Z. 2005, *ApJ*, 625, 463

- Longcope, D. W. 2004, in *SOHO-15: Coronal Heating*, ed. R. W. Walsh, J. Ireland, D. Danesy, & B. Fleck (Noordwijk, The Netherlands: ESA), ESA SP-575, 198
- Lucy, L. B. 1971, *ApJ*, 163, 95
- Lucy, L. B. 1976, *ApJ*, 205, 482
- Ludwig, H.-G., Jordan, S., & Steffen, M. 1994, *A&A*, 284, 105
- Mannheimer, W. M., & Klein, H. H. 1975, *Phys. Fluids*, 18, 1299
- Markovskii, S. A., Vasquez, B. J., Smith, C. W., & Hollweg, J. V. 2006, *ApJ*, 639, 1177
- Marsch, E. 2005, in *Solar Wind 11/SOHO-16: Connecting Sun and Heliosphere*, ed. B. Fleck, T. Zurbuchen, & H. Lacoste (Noordwijk, The Netherlands: ESA), ESA SP-592, 191
- Marsch, E., Zhou, G.-Q., He, J.-S., & Tu, C.-Y. 2006, *A&A*, 457, 699
- Matthaeus, W. H., Zank, G. P., Oughton, S., Mullan, D. J., & Dmitruk, P. 1999, *ApJ*, 523, L93
- Matthaeus, W. H., & Zhou, Y. 1989, *Phys. Fluids B*, 1, 1929
- Mazzotta, P., Mazzitelli, G., Colafrancesco, S., & Vittorio, N. 1998, *A&AS*, 133, 403
- McClymont, A. N., & Canfield, R. C. 1983, *ApJ*, 265, 483
- McCracken, K. G., & Ness, N. F. 1966, *J. Geophys. Res.*, 71, 3315
- McIntosh, S. W., & Leamon, R. J. 2005, *ApJ*, 624, L117
- McKenzie, J. F., Banaszkiewicz, M., & Axford, W. I. 1995, *A&A*, 303, L45
- Mihalas, D. 1978, *Stellar Atmospheres*, 2nd ed. (San Francisco: W. H. Freeman)
- Mihalas, D., & Mihalas, B. W. 1984, *Foundations of Radiation Hydrodynamics* (Oxford: Oxford U. Press)
- Milano, L. J., Gómez, D. O., & Martens, P. C. H. 1997, *ApJ*, 490, 442
- Möstl, C., Hanslmeier, A., Sobotka, M., Puschmann, K., & Muthsam, H. J. 2006, *Sol. Phys.*, 237, 13
- Muglach, K. 2006, *BAAS*, 38, 247 (SPD abstract 19.01)
- Mullan, D. J., & Cheng, Q. Q. 1993, *ApJ*, 412, 312
- Musielak, Z. E., Rosner, R., Stein, R. F., & Ulmschneider, P. 1994, *ApJ*, 423, 474
- Musielak, Z. E., Rosner, R., & Ulmschneider, P. 2000, *ApJ*, 541, 410
- Musielak, Z. E., & Ulmschneider, P. 2002, *A&A*, 386, 606
- Narain, U., & Ulmschneider, P. 1990, *Space Sci. Rev.*, 54, 377
- Narain, U., & Ulmschneider, P. 1996, *Space Sci. Rev.*, 75, 453
- Natta, A., Giovanardi, C., & Palla, F. 1988, *ApJ*, 332, 921
- Nesis, A., Hammer, R., Hanslmeier, A., Schleicher, H., Sigwarth, M., & Staiger, J. 1997, *A&A*, 326, 851
- Nesis, A., Hammer, R., Kiefer, M., Schleicher, H., Sigwarth, M., & Staiger, J. 1999, *A&A*, 345, 265
- Neugebauer, M., Liewer, P. C., Smith, E. J., Skoug, R. M., & Zurbuchen, T. H. 2002, *J. Geophys. Res.*, 107 (A12), 1488, doi:10.1029/2001JA000306
- Newkirk, G., Jr. 1967, *ARA&A*, 5, 213
- Nigro, G., Malara, F., Carbone, V., & Veltri, P. 2004, *Phys. Rev. Lett.*, 92, 194501
- Nisenson, P., van Ballegoijen, A. A., de Wijn, A. G., & Sütterlin, P. 2003, *ApJ*, 587, 458
- Nowak, T., & Ulmschneider, P. 1977, *A&A*, 60, 413
- Ofman, L. 2005, *Space Sci. Rev.*, 120, 67
- Ofman, L., & Davila, J. M. 1998, *J. Geophys. Res.*, 103, 23677
- Olsen, E. L., & Leer, E. 1996, *ApJ*, 462, 982
- Orlando, S., Lou, Y.-Q., Rosner, R., & Peres, G. 1996, *J. Geophys. Res.*, 101, 24433
- Osterbrock, D. E. 1961, *ApJ*, 134, 347
- Oughton, S., Dmitruk, P., & Matthaeus, W. H. 2006, *Phys. Plasmas*, 13, 042306
- Owocki, S. P. 2004, in *Evolution of Massive Stars, Mass Loss, and Winds*, ed. M. Heydari-Malayeri, P. Stee, & J.-P. Zahn, *EAS Pub. Ser.* 13, 163
- Owocki, S. P., Holzer, T. E., & Hundhausen, A. J. 1983, *ApJ*, 275, 354
- Parker, E. N. 1958, *ApJ*, 128, 664
- Parker, E. N. 1963, *Interplanetary Dynamical Processes* (New York: Interscience)
- Perkins, F. 1973, *ApJ*, 179, 637
- Peter, H., Gudiksen, B. V., & Nordlund, Å. 2004, in *Cool Stars, Stellar Systems, and the Sun*, 13th Cambridge Workshop, ed. F. Favata, G. Hussain, & B. Battrick, (Noordwijk, The Netherlands: ESA), ESA SP-560, 59
- Pneuman, G. W. 1980, *A&A*, 81, 161
- Porter, L. J., Klimchuk, J. A., & Sturrock, P. A. 1994, *ApJ*, 435, 502
- Press, W. H., Teukolsky, S. A., Vetterling, W. T., & Flannery, B. P. 1992, *Numerical Recipes in Fortran: The Art of Scientific Computing* (Cambridge: Cambridge Univ. Press)
- Rammacher, W., Fawzy, D., Ulmschneider, P., & Musielak, Z. E. 2005, *ApJ*, 631, 1113
- Rappazzo, A. F., Velli, M., Einaudi, G., & Dahlburg, R. B. 2007, *ApJ*, 657, L47
- Riley, P., Linker, J. A., & Mikić, Z. 2001, *J. Geophys. Res.*, 106, 15889
- Rimmele, T. R., Goode, P. R., Harold, E., & Stebbins, R. T. 1995, *ApJ*, 444, L119
- Roberts, B. 2000, *Sol. Phys.*, 193, 139
- Roupe van der Voort, L. H. M., Hansteen, V. H., Carlsson, M., Fossum, A., Marthinussen, E., van Noort, M. J., & Berger, T. E. 2005, *A&A*, 435, 327
- Roussev, I. I., Gombosi, T. I., Sokolov, I. V., Velli, M., Manchester, W., IV, DeZeeuw, D. L., Liewer, P., Tóth, G., & Luhmann, J. 2003, *ApJ*, 595, L57
- Rubinstein, R., & Zhou, Y. 2002, *ApJ*, 572, 674
- Saar, S. H. 2001, in *Cool Stars, Stellar Systems, and the Sun*, 11th Cambridge Workshop, ed. R. Garcia Lopez, R. Rebolo, & M. Zapaterio Osorio, *ASP Conf. Ser.* 223, 292
- Sagdeev, R. Z., & Galeev, A. A. 1969, *Nonlinear Plasma Theory* (New York: W. A. Benjamin)
- Sánchez Almeida, J. 2001, *ApJ*, 556, 928
- Schirmacher, V., Woitke, P., & Sedlmayr, E. 2003, *A&A*, 404, 267
- Schmitz, F., & Fleck, B. 1998, *A&A*, 337, 487
- Schmutzler, T., & Tscharnuter, W. M. 1993, *A&A*, 273, 318
- Scholz, T. T., & Walters, H. R. J. 1991, *ApJ*, 380, 302
- Schrijver, C. J. 1995, *A&A Rev.*, 6, 181
- Schrijver, C. J., et al. 1996, *ApJ*, 468, 921
- Schrijver, C. J., et al. 2006, *Sol. Phys.*, 235, 161
- Schwadron, N. A., Fisk, L. A., & Zurbuchen, T. H. 1999, *ApJ*, 521, 859
- Schwadron, N. A., & McComas, D. J. 2003, *ApJ*, 599, 1395
- Schwarzschild, M. 1948, *ApJ*, 107, 1
- Scudder, J. D., & Olbert, S. 1983, in *Solar Wind Five*, ed. M. Neugebauer, *NASA CP-2280*, 163
- Shebalin, J. V., Matthaeus, W. H., & Montgomery, D. 1983, *J. Plasma Phys.*, 29, 525
- Sheeley, N. R., Jr., et al. 1997, *ApJ*, 484, 472
- Shmeleva, O. P., & Syrovatskii, S. I. 1973, *Sol. Phys.*, 33, 341
- Sittler, E. C., Jr., & Guhathakurta, M. 1999, *ApJ*, 523, 812
- Sittler, E. C., Jr., & Guhathakurta, M. 2002, *ApJ*, 564, 1062
- Smith, D. F., & Auer, L. H. 1980, *ApJ*, 238, 1126
- Smith, D. F., & Lilliequist, C. G. 1979, *ApJ*, 232, 582
- Spitzer, L., Jr. 1962, *Physics of Fully Ionized Gases*, 2nd ed. (New York: Wiley)
- Spruit, H. C. 1981, *A&A*, 98, 155
- Spruit, H. C. 1982, *Sol. Phys.*, 75, 3
- Stein, R. F. 1967, *Sol. Phys.*, 2, 385
- Stein, R. F., & Schwartz, R. A. 1972, *ApJ*, 177, 807
- Stein, R. F., & Schwartz, R. A. 1973, *ApJ*, 186, 1083
- Strachan, L., Suleiman, R., Panasyuk, A. V., Biesecker, D. A., & Kohl, J. L. 2002, *ApJ*, 571, 1008
- Suess, S. T., Wang, A.-H., & Wu, S. T. 1996, *J. Geophys. Res.*, 101, 19957
- Suzuki, T. K. 2004, *MNRAS*, 349, 1227
- Suzuki, T. K. 2006, *ApJ*, 640, L75
- Suzuki, T. K. 2007, *ApJ*, in press, astro-ph/0608195
- Suzuki, T. K., & Inutsuka, S.-I. 2005, *ApJ*, 632, L49
- Suzuki, T. K., & Inutsuka, S.-I. 2006, *J. Geophys. Res.*, 111, A06101, doi:10.1029/2005JA011502
- Tóth, G., et al. 2005, *J. Geophys. Res.*, 110, A12226, doi:10.1029/2005JA011126
- Tu, C.-Y., & Marsch, E. 1995, *Space Sci. Rev.*, 73, 1
- Tu, C.-Y., Marsch, E., & Rosenbauer, H. 1992, in *Solar Wind Seven*, ed. E. Marsch & R. Schwenn (New York: Pergamon), 555
- Tu, C.-Y., Marsch, E., & Thieme, K. M. 1989, *J. Geophys. Res.*, 94, 11739
- Ulmschneider, P. 1970, *A&A*, 4, 144
- Ulmschneider, P., & Muchmore, D. 1986, in *Small Scale Magnetic Flux Concentrations in the Solar Photosphere*, ed. W. Deinzer, M. Knölker, & H. H. Voigt (Göttingen: Vandenhoeck & Ruprecht), 191
- Ulmschneider, P., Musielak, Z. E., & Fawzy, D. E. 2001, *A&A*, 374, 662
- Ulmschneider, P., Rammacher, W., Musielak, Z. E., & Kalkofen, W. 2005, *ApJ*, 631, L155
- Ulmschneider, P., Schmitz, F., Kalkofen, W., & Bohn, H. U. 1978, *A&A*, 70, 487
- Ulmschneider, P., Theurer, J., & Musielak, Z. E. 1996, *A&A*, 315, 212
- Usmanov, A. V., & Goldstein, M. L. 2006, *J. Geophys. Res.*, 111, A07101, doi:10.1029/2005JA011533
- van Ballegoijen, A. A. 1986, *ApJ*, 311, 1001
- van Ballegoijen, A. A., Nisenson, P., Noyes, R. W., Löfdahl, M. G., Stein, R. F., Nordlund, Å., & Krishnakumar, V. 1998, *ApJ*, 509, 435
- van Noort, M. J., & Roupe van der Voort, H. M. 2006, *ApJ*, 648, L67
- Vásquez, A. M., van Ballegoijen, A. A., & Raymond, J. C. 2003, *ApJ*, 598, 1361
- Vauclair, S. 1996, *A&A*, 308, 228
- Velli, M. 1993, *A&A*, 270, 304
- Venkatakrishnan, P. 1986, *Nature*, 322, 156

Verdini, A., Dmitruk, P., Oughton, S., Velli, M., & Matthaeus, W. H. 2006, in SOHO-17: Ten Years of SOHO and Beyond, ed. H. Lacoste (Noordwijk, The Netherlands: ESA), ESA SP-617, in press

Verdini, A., Velli, M., & Oughton, S. 2005, A&A, 444, 233

Veselovsky, I. 2001, Ap&SS, 277, 219

Vögler, A., Bruls, J. H. M. J., & Schüssler, M. 2004, A&A, 421, 741

Voitenko, Y., & Goossens, M. 2003, Space Sci. Rev., 107, 387

Voitenko, Y., & Goossens, M. 2004, ApJ, 605, L149

von Steiger, R., & Geiss, J. 1989, A&A, 225, 222

von Steiger, R., Schwadron, N. A., Fisk, L. A., Geiss, J., Gloeckler, G., Hefti, S., Wilken, B., Wimmer-Schweingruber, R. F., & Zurbuchen, T. H. 2000, J. Geophys. Res., 105, 27217

Vriens, L., & Smeets, H. M. 1980, Phys. Rev. A, 22, 940

Wang, Y.-M. 1993, ApJ, 410, L123

Wang, Y.-M. 1996, ApJ, 464, L91

Wang, Y.-M., & Sheeley, N. R., Jr. 1990, ApJ, 355, 726

Wang, Y.-M., & Sheeley, N. R., Jr. 1991, ApJ, 372, L45

Wang, Y.-M., & Sheeley, N. R., Jr. 2003, ApJ, 587, 818

Wang, Y.-M., & Sheeley, N. R., Jr. 2006, ApJ, 653, 708

Wang, Y.-M., Sheeley, N. R., Jr., Socker, D. G., Howard, R. A., & Rich, N. B. 2000, J. Geophys. Res., 105, 25133

Wang, Z., Ulrich, R. K., & Coroniti, F. V. 1995, ApJ, 444, 879

Weymann, R. 1960, ApJ, 132, 452

Whang, Y. C. 1997, ApJ, 485, 389

Withbroe, G. L. 1988, ApJ, 325, 442

Wunnenberg, M., Kneer, F., & Hirzberger, J. 2002, A&A, 395, L51

Young, P. R., Del Zanna, G., Landi, E., Dere, K. P., Mason, H. E., & Landini, M. 2003, ApJS, 144, 135

Zhang, J., White, S. M., & Kundu, M. R. 1998, ApJ, 504, L127

Zhou, Y., & Matthaeus, W. H. 1990, J. Geophys. Res., 95, 10291

Zurbuchen, T. H., Fisk, L. A., Gloeckler, G., & von Steiger, R. 2002, Geophys. Res. Lett., 29 (9), 1352, doi:10.1029/2001GL013946

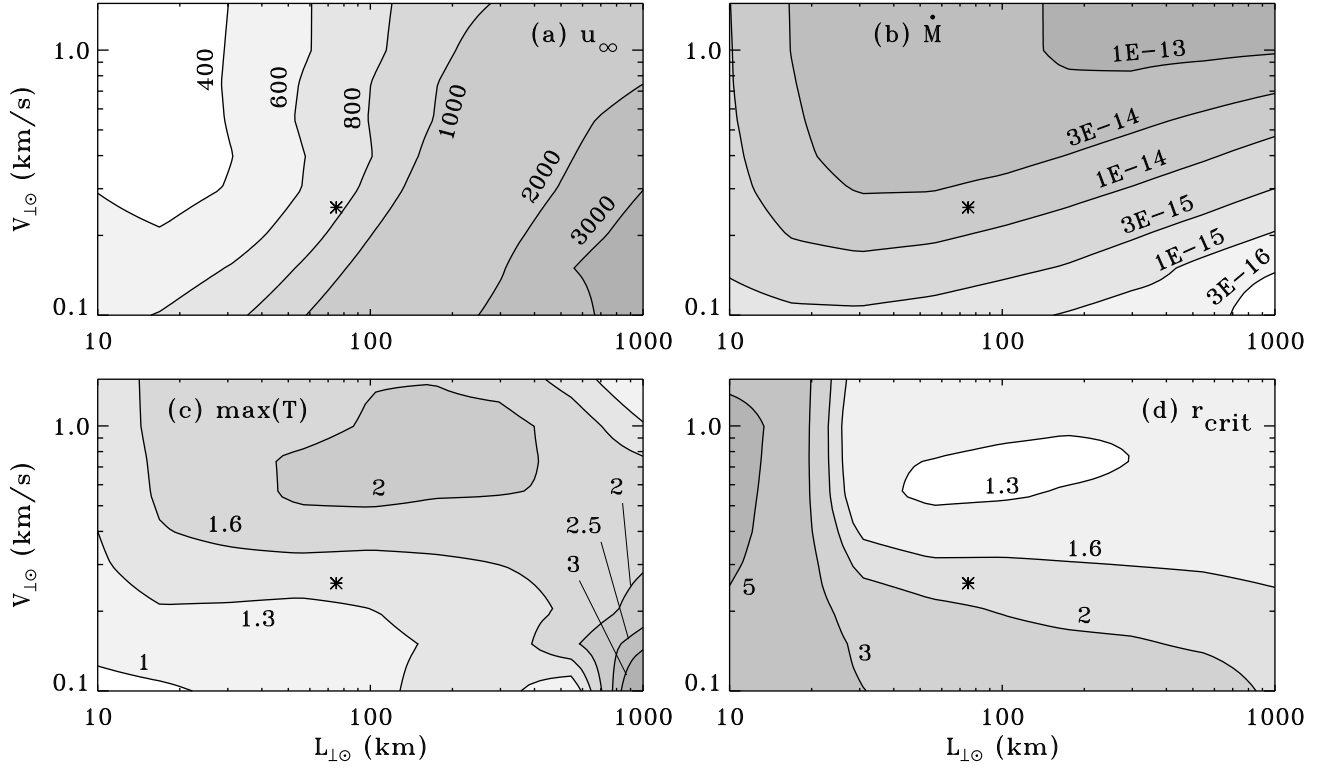


FIG. 6.— Contour plots of solar wind quantities resulting from varying the coronal heating parameters  $v_{\perp\odot}$  and  $L_{\perp\odot}$ : (a) terminal wind speed  $u_{\infty}$  in units of  $\text{km s}^{-1}$ , (b) mass loss rate  $\dot{M}$  in units of  $M_{\odot} \text{ yr}^{-1}$ , (c) maximum coronal temperature in units of MK, (d) heliocentric critical radius in units of  $R_{\odot}$ . Also shown in each panel are the parameters chosen for the model of fast wind from a polar coronal hole discussed in § 8.3 (stars).